UNIVERSITY OF SOUTHAMPTON

FACULTY OF ENGINEERING AND THE ENVIRONMENT

Aerodynamics and Flight Mechanics

Full-Field Surface Pressure Reconstruction Using Deflectometry and the Virtual Fields Method

by

Rene Kaufmann

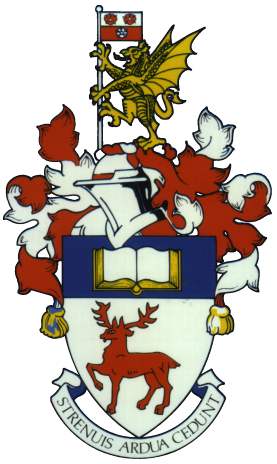

Thesis for the degree of Doctor of Philosophy

Supervised by Prof. B. Ganapathisubramani and Prof. F. Pierron

July 7, 2019

UNIVERSITY OF SOUTHAMPTON

ABSTRACT

FACULTY OF ENGINEERING AND THE ENVIRONMENT
Aerodynamics and Flight Mechanics

FULL-FIELD SURFACE PRESSURE RECONSTRUCTION USING DEFLECTOMETRY AND THE VIRTUAL FIELDS METHOD

by Rene Kaufmann

This thesis presents a technique for the reconstruction of full-field surface pressure distributions with low differential amplitudes. The method is demonstrated in two different setups with air jets impinging on flat plates. Surface deformations were obtained using deflectometry, a highly sensitive technique for slope measurement. The surface slopes in combination with the plate material constitutive mechanical parameters were used as input for pressure reconstructions with the Virtual Fields Method (VFM), which is an application of the principle of virtual work. Both static and dynamic pressure distributions were reconstructed in full-field with this technique. Results were compared with pressure transducer measurements at discrete points. The observed pressure amplitudes were between $\mathcal{O}(1)$ Pa – $\mathcal{O}(100)$ Pa. The spatial extent of the investigated flow structures was $\mathcal{O}(1)$ mm – $\mathcal{O}(10)$ mm. Dynamic pressure information was extracted from time-resolved deflectometry data using temporal band-pass filters or phase-locked measurements. Dynamic Mode Decomposition (DMD) was used on time-resolved data to identify relevant spatial information that correspond to specific frequencies. Despite the low differential amplitudes, dynamically important spatio-temporal events could be observed. Full-field measurements of such small-scale, low-amplitude pressure events are not possible with established pressure measurement techniques. A finite element model was employed in combination with artificial grid deformation to assess the uncertainty of the pressure reconstructions. Finally, challenges and limitations in achieving the metrological performance for resolving the observed surface slopes of $\mathcal{O}(0.1)$ mm km^{-1} – $\mathcal{O}(10)$ mm km^{-1} as well as in the pressure reconstruction approach are described and strategies for future applications are discussed.

Contents

List of Figures

Paper 2

Paper 3

List of Tables

Declaration of Authorship

I, Rene Kaufmann , declare that the thesis entitled *Full-Field Surface Pressure Reconstruction Using Deflectometry and the Virtual Fields Method* and the work presented in the thesis are both my own, and have been generated by me as the result of my own original research. I confirm that:

- this work was done wholly or mainly while in candidature for a research degree at this University;
- where any part of this thesis has previously been submitted for a degree or any other qualification at this University or any other institution, this has been clearly stated;
- where I have consulted the published work of others, this is always clearly attributed;
- where I have quoted from the work of others, the source is always given. With the exception of such quotations, this thesis is entirely my own work;
- I have acknowledged all main sources of help;
- where the thesis is based on work done by myself jointly with others, I have made clear exactly what was done by others and what I have contributed myself;
- none of this work has been published before submission

Signed:.....

Date:.....

Acknowledgements

I would like to thank my supervisors Bharathram Ganapathisubramani and Fabrice Pierron who gave me the opportunity to undertake this PhD, supported me with their knowledge and continuously provided perspective and advice. I am grateful to my colleagues for all their help and support throughout the years. Thanks to the EPSRC for funding my work. Finally, I would like to thank my friends and family for their encouragement and patience.

Nomenclature

Symbols

a	Acceleration
$b_{\frac{1}{2}}$	Half width of pressure profile on impingement plate
C	Camera position
D_{xx}, D_{xy}	Bending stiffness matrix components
D	Nozzle diameter
e	Camera offset
E	Young's Modulus
F	Force
f_{aq}	Acquisition frequency
f_{lens}	Focal length
h_{G}	Distance between grid and sample
h_{N}	Distance between nozzle exit and impingement plate
I	Intensity
l	Slot length
l_{S}	Side length of specimen
M	Magnification
N_{lens}	f-number
p_{G}	Grid pitch
P_{max}	Peak pressure
P_{stag}	Stagnation pressure
P_{exit}	Nozzle exit velocity
P_{∞}	Free stream pressure
Q	In-plane stiffness matrix
r	Radial distance
R	Radius
Re	Reynolds number
S	Surface area
s_{p}	Standard deviation of pressure
t	Time
t_{S}	Plate thickness

u_i	Displacement in direction i
U_{pp}	Peak-to-peak voltage
U_∞	Free stream velocity
v_{peak}	Peak velocity
V	Volume
w	Deflection
w_S	Slot width
W	Work
x, y, z	Cartesian coordinates
$y_{0.5}$	Half-width of jet velocity profile
α	Local slope
ε	Strain
Θ	Angle between grid and camera
κ	Curvature
ν	Poisson's ratio
ν_k	Kinematic viscosity
ξ	Parametric coordinate
ρ	Material density
σ	Stress
Φ	Phase

Superscripts

*	Virtual quantities

Abbreviations

DMD	Dynamic mode decomposition
PIV	Particle image velocimetry
POD	Proper orthogonal decomposition
PRW	Pressure reconstruction window
ROI	Region of interest
VFM	Virtual fields method

Part I

Introduction

Chapter 1

Overview

1.1 Motivation

Full-field surface pressure information is highly relevant for engineering applications like material testing, component design, flow control and impinging jets. It allows determining the aerodynamic loads on *e.g.* fuselages, aerofoils and ship hulls, which are required to evaluate the performance of such components. Surface pressure information is also important for applications involving pipe flows (Browne and Dinkelacker, 1995). In supersonic scenarios, full-field information can be used to determine the position and intensity of shocks (Yang et al., 2012). For the research of turbulent flows low-range differential pressure amplitudes are required to identify turbulent structures forming or impinging on surfaces. This is relevant for the investigation and control of turbulent boundary layers mechanisms (Bull, 1996; Willmarth, 1975), *e.g.* for drag reduction in applications of compliant surfaces (Dinkelacker et al., 1977). It also allows investigating surface-structure interactions along rough walls in boundary-layer flows (Young, 1965). Impinging jets are an essential tool for heat and mass transfer, *e.g.* in the cooling, de-icing and coating of surfaces (N. B. Livingood and Hrycak, 1973; Jambunathan et al., 1992). Full-field pressure information would help assessing the efficiencies of such jets, as local transfer rates of the relevant quantities are connected to the turbulent pressure fluctuations on the surface (Gardon and Akfirat, 1965).
However, full-field, low-amplitude differential surface pressure information is challenging to obtain with established techniques. Pressure transducers and microphones, which are often used for the measurement of low-range differential amplitudes, can only supply point-wise information. Due to their size with typically $2-3$ mm diameter this leads to very limited spatial resolution (Corcos, 1963, 1964). As they need to be integrated into the investigated surface, they can further change the mechanical material response. Large arrays of circular membranes with 2.5 mm diameter each were employed as pressure sensors in the past (Dinkelacker et al., 1977; Emmerling et al., 1975). Using an interferometry setup, interference fringes were recorded on each of the membranes simultaneously to measure the fluctuations under a turbulent boundary layer. A calibration against microphones was used to derive a

relationship between the number of fringes and the pressure acting on the membranes. The evaluation of the data was however challenging, and the spatial resolution was still limited by the diameter of the membranes. Pressure sensitive paints are an option for full-field measurements of large-range differential pressures, but they are difficult to procure and to apply (Gregory et al., 2008; Kim et al., 2019; Tropea et al., 2007, chapter 4.4). They are often used in transonic and supersonic scenarios (Engler et al., 2000; Liu et al., 2008). Particle Image Velocimetry (PIV) can be used for pressure reconstructions in the flow field (van Oudheusden, 2013; Ragni et al., 2009), but reflections and the finite size of the reconstruction window do not allow measurements directly on the surface. PIV can however be used to estimate pressure close to the surface and along lines where it coincides with the field of view (Ghaemi et al., 2012).

None of these techniques can however provide the combination of metrological performance in terms of pressure amplitude, spatial scales and full-field data which the present work aims at. Alternatively, pressure can be reconstructed from full-field surface deformation measurements by solving the local equilibrium equations. A number of measurement techniques is available to acquire the necessary full-field deformation information, like Digital Image Correlation (DIC), Laser Doppler Vibrometers (LDV) and interferometry techniques. In Brown et al., 2018 3D-Digital Image Correlation (DIC) measurements were conducted on a flexible Kevlar wind-tunnel wall in order to reconstruct wall pressure. This was achieved by projecting the measured deflection maps onto polynomial basis functions and then inserting their derivatives into the corresponding equilibrium equations. The obtained pressure coefficients were found to compare well to transducer data, but the investigated scales were relatively large. For thin plates under pure bending as in the present scenario, the local equilibrium equation involves fourth order derivatives of the local surface deflections (Timoshenko and Woinowsky-Krieger, 1959). Each differentiation tends to amplify experimental noise. In case of fourth order derivatives, it is therefore necessary to employ rigorous regularisation techniques. This has been achieved by employing wave number filters in Pezerat and Guyader, 2000 and by adapting the number of data points used for the finite differences in the differentiation scheme in Leclére and Pézerat, 2012. External vibration sources acting on the investigated specimen were identified and localized in these studies. Similarly, wave number filters were used in an investigation of a turbulent boundary layer to identify the acoustic component of a flow in Lecoq et al., 2014. The accuracies that can be achieved in terms of localisation and amplitude identification are limited by the regularization technique as well as the signal-to-noise ratio of the deformation data.

The low differential pressure amplitudes and the small spatial scales investigated in the present work can not be resolved with these approaches. Instead, the principle of virtual work can be employed. It yields an equation that is equivalent to the local equilibrium equation, but only involves second order deflection derivatives in case of the problem of a thin plate in pure bending. The Virtual Fields Method (VFM) (Pierron and Grédiac, 2012) is an application of the principle of virtual work, which allows an identification of constitutive mechanical material properties from known loading or *vice versa* from full-field kinematic data. Further advantages are that the VFM does not require detailed knowledge of the boundary conditions and that

it does not rely on computationally expensive, iterative procedures. The VFM was compared with other, similar methods in Martins et al., 2018. It was found to consistently perform best in terms of computational cost when compared to Finite Element Model Updating and the Constitutive Equation Gap method. VFM load reconstructions have been performed in several studies, including dynamic load identifications in a Hopkinson bar in Moulart et al., 2011; Pierron et al., 2011. The VFM load reconstructions were found to compare reasonably well to standard measurement techniques. Further, spatially-averaged sound pressure levels were reconstructed with the VFM from an acoustic field using a scanning LDV in Robin and Berry, 2018. In a similar approach, dynamic transverse loads and vibrations caused by acoustic pressure were identified in Berry et al., 2014. For distributed loads, the results were found to be accurate. The study applied the VFM using piecewise virtual fields. These allow more accurate descriptions of boundary conditions for complex shapes and heterogeneous materials (Toussaint et al., 2006). This approach was later applied to random, spatial wall pressure excitations in Berry and Robin, 2016. Power spectral density functions were reconstructed from the experimental data and the VFM was used to describe the plate response. It was found that piecewise virtual fields had to be defined over small regions to obtain reasonable results for this application.

The VFM approach was combined with a deflectometry setup to identify mechanical point loads of several $\mathcal{O}(1)$ N in O'Donoughue et al., 2017. Deflectometry is a highly sensitive optical technique for surface slope measurements (Surrel et al., 1999). In the past it was used for the damage detection of composites *e.g.* in Devivier et al., 2012, for the analysis of stiffness and damping parameters of vibrating plates in Giraudeau et al., 2010 and for the imaging of ultrasonic Lamb waves in Devivier et al., 2016. Using full-field surface slopes as input to the VFM reduces the order of derivatives required for pressure reconstruction to one. In O'Donoughue et al., 2017 loads were found to be reconstructed with good accuracy for certain sizes of the piecewise defined virtual fields. The ideal domain sizes were found empirically from comparisons with the known amplitudes of the mechanical loads. In O'Donoughue et al., 2019 pressure auto-spectra of spatially averaged random excitations were identified using the same combination of deflectometry and the VFM. Except at structural resonance frequencies and for poor signal-to-noise-ratios, the results were found to agree well with microphone array measurements.

While these studies have shown the potential of deflectometry and the VFM for full-field pressure reconstructions, they do not investigate the applicability of the techniques for the sought low-range amplitudes and small spatial scales. They further omit the accuracy of the method which is required for applications to unknown input loads. This is an essential step because neither the resolution in space nor the uncertainty in pressure amplitude can be predicted directly, as they depend on the signal amplitude and distribution, the noise level and the processing parameters. The present thesis addresses these gaps in the current research and systematically explores the capabilities and limitations of the experimental and processing techniques.

1.2 Research Objectives and Approach

This work investigates the capabilities and limitations of deflectometry and the VFM in measuring full-field pressure information. The following main questions are addressed in this thesis:

- What is required to detect and reconstruct low-amplitude differential pressure distributions in full-field?
- How can the dynamic, low-amplitude and small-scale pressure fluctuations that occur in turbulent flows be extracted?
- What are the relevant experimental requirements and limitations?
- What influence do the processing parameters have on the identified pressure amplitudes?
- How accurate are the pressure reconstructions?

First, the reconstruction of mean pressure distributions from time-averaged slope measurements is addressed. A Gaussian pressure distribution from a round, impinging air jet was chosen as test application. This allowed investigating the general capabilities in measuring pressure over a range of amplitudes from zero to peak pressures of $\mathcal{O}(100)$ Pa. Simulated experiments are introduced in order to assess the influence of different error sources and of the processing parameters. The fluctuations of the same impinging jet are further investigated using time-resolved measurements. Spatial and temporal filter techniques are used to extract relevant dynamic information. Finally, improvements for an increased metrological performance of the setup are introduced in order to resolve small-scale spatial distributions from an impinging synthetic jet setup.

1.3 Outline

This thesis presents a methodology for the reconstruction of static and dynamic surface pressure distributions with low-range differential amplitudes from optical full-field deformation measurements. The applicability of the data acquisition and processing approaches are demonstrated in two different setups using air jets impinging on thin plates. The work is presented in three main parts. The key content and results are contained in three papers, which form the core of this thesis.

- Part I introduces background information on the theory and experimental methods that are applied throughout this work.
- Part II presents the main content including literature review, methodology, results and discussion in the three papers:

- *Full-field surface pressure reconstruction using the Virtual Fields Method*

- *Reconstruction of surface pressure fluctuations using deflectometry and the Virtual Fields Method*

- *Surface pressure reconstruction from phase-averaged deflectometry measurements using the Virtual Fields Method*

- Part III discusses general recommendations and presents the outlook and conclusions.

Chapter 2

Background

2.1 Deflectometry

Deflectometry is an optical technique for the measurement of surface slopes (Surrel et al., 1999). A schematic of the setup is shown in fig. 2.1. A camera is placed next to the periodic spatial signal, here a cross-hatched grid with printed pitch p_G, and is directed at the specimen surface. The distance to the specimen is denoted with h_G. The camera records the reflected grid in normal incidence. The angle θ should be minimized in order to avoid distortions. In an unloaded configuration, a pixel directed at point M on the surface images the reflection of grid point P. If a load is applied to the specimen, it deforms locally and the same pixel images the reflection of grid point P′. In order to obtain information on the related shift in slope, the local phases have to be extracted.

2.1.1 Phase Extraction

A number of methods for retrieving phase information from grid images is described in the literature, *e.g.* Surrel, 2000; Dai et al., 2014; Grédiac et al., 2016. The relevant approaches can be divided into global and local phase detection. For the global approach, a whole set of

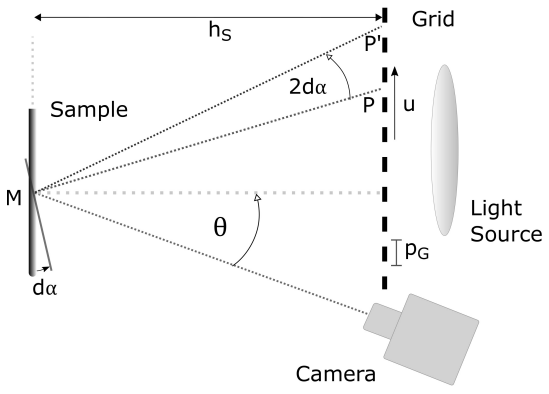

Figure 2.1: Top view of deflectometry setup and working principle.

intensity data from an image is processed using the Fourier transform technique. This approach has poorer phase measurement accuracy and spatial resolution than the local approaches (Davila et al., 2003) and may require filtering in the Fourier plane depending on the analysed pattern, which makes automation challenging (Surrel, 2000). The local approaches calculate phase information from local intensity measurements. They are also called phase-stepping or phase-shifting techniques. These are further divided into temporal and spatial approaches. In case of static measurements, temporal phase-stepping allows *e.g.* damage detection on a surface (Kim et al., 2009). It requires a series of images to be taken with a known phase shift in the reference signal between images. The phase is then calculated for each pixel from the intensities measured at that pixel.

For the dynamic measurements investigated here, a spatial phase-stepping approach (Surrel, 1996; Poon et al., 1993) was chosen. It requires a spatial carrier signal with known frequency and an integer number of pixels per period in the recorded image. This allows calculating a phase map from one image. The algorithm used for spatial phase-stepping in deflectometry under real conditions needs to cope with miscalibration, i.e. a slightly non-integer number of pixels per grid. Further, the investigated signal is not perfectly sinusoidal here. This requires an algorithm to suppress harmonics and sets a lower limit to the number of samples (pixels per recorded grid pitch) required (Hibino et al., 1995). A Windowed Discrete Fourier Transform (WDFT) algorithm is suitable to address this problem (Surrel, 2000):

$$\varphi = \arctan\left(- \frac{\sum_{k=1}^{N-1} k(I_{k-1} - I_{2N-k-1}) \sin(\frac{2k\pi}{N})}{N\ I_{N-1} + \sum_{k=1}^{N-1} k(I_{k-1} - I_{2N-k-1}) \cos(\frac{2k\pi}{N})} \right) \quad , \tag{2.1}$$

where N represents number of pixels per period and I_k is the measured intensity at pixel k. The triangular weighting featured by this algorithm reduces the sensitivity to miscalibration. It is insensitive to harmonics of order up to $N-2$, (Surrel, 1996).

If a large number of grid periods is processed in each direction, the detected phase is wrapped between $[-\pi \quad +\pi]$. This results in 2π 'jumps' which have to be removed before further processing the phases into the measured physical quantity, (Surrel, 2000). Algorithms used on experimental data are however susceptible to detecting false jumps which originate from noise. An algorithm that was found to be robust to noise, fast and memory efficient is used here (Bioucas-Dias and Valadão, 2007).

2.1.2 Surface Slopes

The displacement $\boldsymbol{u}$ between points P and P′ is related to the phase difference dϕ in the grid signal in x- and y-direction respectively as follows:

$$d\phi_x = \frac{2\pi}{p_G} u_x, \quad d\phi_y = \frac{2\pi}{p_G} u_y \tag{2.2}$$

Since the physical point on the specimen surface is subject to a displacement, these relations are not exact. An iterative procedure that is described in Grédiac et al., 2016, section 4.2 was employed to minimize the resulting error:

$$\boldsymbol{u}_{n+1}(\boldsymbol{x}) = -\frac{p_G}{2\pi}(\phi_{def}(\boldsymbol{x} + \boldsymbol{u}_n(\boldsymbol{x})) - \phi_{ref}(\boldsymbol{x})) \quad , \tag{2.3}$$

Where ϕ_{def} and ϕ_{ref} the phases in the deformed and reference configuration respectively. Using geometric considerations and assuming a sufficiently small angle α, so the camera records images in normal incidence, and that h_G is large against the shift $\boldsymbol{u}$, a linear relationship between slopes and displacement can be derived (see *e.g.* (Ritter, 1982)):

$$d\alpha_x = \frac{u_x}{2h_G}, \quad d\alpha_y = \frac{u_y}{2h_G} \tag{2.4}$$

If the above assumptions are not valid, a more complex calibration is required (Balzer and Werling, 2010; Surrel and Pierron, 2019). Eq. 2.4 will be used throughout this work.
The spatial resolution of the method is driven by the printed pitch of the spatial signal, p_G. The phase resolution dependents on measurement noise. Here, it is defined as the standard deviation of the difference between two phase maps measured on a stationary specimen. The slope resolution depends on the phase resolution as well as on the printed pitch, p_G, and the distance between grid and specimen surface, h_G.

2.2 Thin Plate Assumptions

The specimen investigated here were thin plates in pure bending. This allowed employing the Love-Kirchhoff theory, Timoshenko and Woinowsky-Krieger, 1959, which yields a simplified description of the kinematics of such plates (*e.g.* Pierron and Grédiac, 2012; Devivier, 2012, chapter 2):

- All straight lines normal to the middle plane remain normal to the middle plane after deformation.
- Strain components are linear through the thickness of the plate.
- For a load in direction of the surface normal, the out-of-plane displacement is the same through the entire thickness of the plate, i.e. the deflection depends only on the surface coordinates: $u_z = w(x, y)$.
- All in-plane displacements u_x, u_y are proportional to the local slopes:

$$\begin{pmatrix} u_x \\ u_y \end{pmatrix} = -z \begin{pmatrix} \partial_x w \\ \partial_y w \end{pmatrix} \quad , \tag{2.5}$$

where z is the through-thickness position. Differentiating eq. 2.5 yields the strains, ε, which are proportional to the curvatures, κ:

$$\boldsymbol{\varepsilon} = z \cdot \boldsymbol{\kappa} \quad . \tag{2.6}$$

It should be noted that the out-of-plane components are zero, since the deflections are independent from z. The curvatures are:

$$\begin{pmatrix} \kappa_{xx} \\ \kappa_{yy} \\ \kappa_{xy} \end{pmatrix} := - \begin{pmatrix} \partial_x^2 w \\ \partial_y^2 w \\ \partial_x \partial_y w \end{pmatrix} \quad . \tag{2.7}$$

2.3 Principle of Virtual Work

The principle of virtual work postulates that the sum of work of all forces F_i, $i = 1, ...N$ acting on a static system of N points of mass subject to a virtual displacement r_i^* vanishes in equilibrium, Timoshenko and Goodier, 1951, pp151:

$$\delta W = \Sigma_{i=1}^{N} F_i \; r_i^* = 0 \quad . \tag{2.8}$$

Virtual displacements are imagined and instantaneous changes of a mechanical systems coordinates. They have to fulfill the conditions of continuity of the specimen as well as the surface

displacement conditions. The expansion of this principle to dynamic cases is called d'Alembert principle and states that

$$\delta W = \Sigma_{i=1}^{N}(m_i\ \ddot{r}_i - F_i)\ r_i^* \ = \ 0 \quad . \tag{2.9}$$

For small deformations of a thin plate, i.e. the deformed configuration is close to the undeformed one, as expected for the chosen plates bending under the investigated flow conditions, the equilibrium of the plate can be described through the principle of virtual work in its weak form (Dym and Shames, 1973):

$$\underbrace{\int_V \rho\ \boldsymbol{a}\cdot\boldsymbol{u}^* dV}_{W^*_{inertial}} \ = \ \underbrace{-\int_V \boldsymbol{\sigma} : \boldsymbol{\varepsilon}^* dV}_{W^*_{int}} + \underbrace{\int_S \overline{\boldsymbol{T}}\cdot\boldsymbol{u}^*\ dS + \int_V \rho\ \boldsymbol{F_{Vol}}\cdot\boldsymbol{u}^*\ dV}_{W^*_{ext}} \quad , \tag{2.10}$$

with the density ρ, acceleration $\boldsymbol{a}$, virtual displacement $\boldsymbol{u^*}$ and virtual strain $\boldsymbol{\varepsilon^*}$, the mean stress vector, or traction $\overline{\boldsymbol{T}} = \boldsymbol{\sigma}\cdot\boldsymbol{n}$ over the surface over which a load is applied, the external volume force $\boldsymbol{F_{Vol}}$, and the virtual work done by inertial $W^*_{inertial}$, internal W^*_{int} and external forces W^*_{ext}. This equation holds for any continuous and differentiable virtual field $\boldsymbol{u}^*$.
The linear dependence expressed in equation 2.6 has to be taken into account for the parameterization of the virtual fields $\boldsymbol{\varepsilon^*}$ and $\boldsymbol{\kappa^*}$ as well. For non-trivial solutions, virtual fields require in-plane components u_x^* and u_y^* which are odd functions of the out-of-plane coordinate z. Using virtual displacement fields with the same linear z-dependence as the real fields in equation 2.6, the virtual displacement in z-direction can be considered as virtual deflection $\boldsymbol{w^*}$ which again depends only on the in-plane coordinates. It follows that:

$$\begin{pmatrix} u_x^* \\ u_y^* \end{pmatrix} \ = \ -\,z \begin{pmatrix} \partial_x w^* \\ \partial_y w^* \end{pmatrix} \quad , \tag{2.11}$$

and

$$\boldsymbol{\varepsilon^*} \ = \ z\boldsymbol{\kappa^*} \tag{2.12}$$

Neglecting acceleration and external volume forces for now, eq. 2.10 becomes:

$$\int_V \boldsymbol{\sigma}\cdot\boldsymbol{\varepsilon}^* dV \ = \ \int_S \overline{\boldsymbol{T}}\cdot\boldsymbol{u}^*\ dS \quad . \tag{2.13}$$

Eqs. 2.13 and 2.12 yield:

$$\int_V \boldsymbol{\sigma}\cdot z\boldsymbol{\kappa}^* dV \ = \ \int_S \overline{\boldsymbol{T}}\cdot\boldsymbol{u}^*\ dS \quad . \tag{2.14}$$

Using Gauss's theorem, this equals

$$\int_S \left(\int_{-\frac{t}{2}}^{\frac{t}{2}} \boldsymbol{\sigma}\cdot z\boldsymbol{\kappa}^* dz \right) dS \ = \ \int_S \overline{\boldsymbol{T}}\cdot\boldsymbol{u}^*\ dS \quad , \tag{2.15}$$

where t is the thickness of the plate. Assuming pure bending of the plate, *i.e.* no in-plane forces, the generalized Hooke's law describing the stress-strain relation becomes

$$\begin{pmatrix} \sigma_{xx} \\ \sigma_{yy} \\ \sigma_{xy} \end{pmatrix} = \boldsymbol{Q} \begin{pmatrix} \varepsilon_{xx} \\ \varepsilon_{yy} \\ \varepsilon_{xy} \end{pmatrix} \quad , \tag{2.16}$$

with the in-plane stiffness matrix $\boldsymbol{Q}$. For isotropic materials it is given by:

$$\boldsymbol{Q} = \frac{E}{1-\nu^2} \begin{bmatrix} 1 & \nu & 0 \\ \nu & 1 & 0 \\ 0 & 0 & 1-\nu \end{bmatrix} \quad , \tag{2.17}$$

where E is the Young's modulus and ν the Poisson's ratio. Inserting eq. 2.16 into eq. 2.15 and using eq. 2.12 yields:

$$\int_S \left(\int_{-\frac{t}{2}}^{\frac{t}{2}} \boldsymbol{Q} \cdot z\boldsymbol{\kappa} \cdot z\boldsymbol{\kappa}^* \, dz \right) dS = \int_S \overline{\boldsymbol{T}} \cdot \boldsymbol{u}^* \, dS \quad . \tag{2.18}$$

Since $\boldsymbol{\kappa}$ and $\boldsymbol{\kappa}^*$ are independent of z, this is equivalent to:

$$\int_S \boldsymbol{\kappa} \cdot \boldsymbol{\kappa}^* \left(\int_{-\frac{t}{2}}^{\frac{t}{2}} z^2 \boldsymbol{Q} \, dz \right) dS = \int_S \overline{\boldsymbol{T}} \cdot \boldsymbol{u}^* \, dS \quad . \tag{2.19}$$

Introducing the bending stiffness matrix $\boldsymbol{D}$,

$$\boldsymbol{D} = \int_{-\frac{t}{2}}^{\frac{t}{2}} z^2 \boldsymbol{Q} \, dz \quad , \tag{2.20}$$

eq. 2.19 becomes:

$$\int_S \boldsymbol{\kappa}^* \cdot \boldsymbol{D} \cdot \boldsymbol{\kappa} \, dS = \int_S \overline{\boldsymbol{T}} \cdot \boldsymbol{u}^* \, dS \quad . \tag{2.21}$$

In the investigated case of transversal loading, the right-hand side is described by the pressure distribution:

$$\int_S \boldsymbol{\kappa}^* \cdot \boldsymbol{D} \cdot \boldsymbol{\kappa} \, dS = \int_S \boldsymbol{p} \cdot \boldsymbol{w}^* \, dS \quad . \tag{2.22}$$

To describe the present case of dynamic loading an acceleration term is added:

$$\int_S \boldsymbol{\kappa}^* \cdot \boldsymbol{D} \cdot \boldsymbol{\kappa} \, dS + \int_S \rho \, t_S \, \boldsymbol{w}^* a \, dS = \int_S \boldsymbol{p} \cdot \boldsymbol{w}^* \, dS \quad . \tag{2.23}$$

Here the acceleration, a, only acts in z-direction. ρ is the material density and t_S the plate thickness. Assuming that the material is isotropic, one obtains:

$$\begin{aligned} &\int_S D_{xx}\ \kappa_{xx}\kappa^*_{xx}\ dS + \int_S D_{xx}\kappa_{yy}\kappa^*_{yy}\ dS + \int_S D_{xy}\ (\kappa_{xx}\kappa^*_{yy} + \kappa_{yy}\kappa^*_{xx})\ dS\ ... \\ ... &+ \int_S \frac{D_{xx} - D_{xy}}{2}\ 4\ \kappa_{xy}\kappa^*_{xy}\ dS\ +\ \int_S \rho\ t_S\ w^* a\ dS\ =\ \int_S w^* p\ dS \quad , \end{aligned} \tag{2.24}$$

where D_{xx} and D_{xy} are the respective components of the bending stiffness matrix (2.16, 2.20) Further assuming a homogeneous material, the integrals are independent from the $\boldsymbol{D}$ components and eq. 2.24 becomes:

$$\begin{aligned} &D_{xx}\int_S \left(\kappa_{xx}\kappa^*_{xx} + \kappa_{yy}\kappa^*_{yy} +\ 2\ \kappa_{xy}\kappa^*_{xy}\right) dS\ ... \\ ... &+\ D_{xy}\int_S \left(\kappa_{xx}\kappa^*_{yy} + \kappa_{yy}\kappa^*_{xx} -\ 2\ \kappa_{xy}\kappa^*_{xy}\right) dS\ +\ \rho\ t_S \int_S w^* a\ dS\ =\ \int_S w^* p\ dS \quad . \end{aligned} \tag{2.25}$$

Here, the parameters D_{xx}, D_{xy}, ρ and t_S are known from the plate manufacturer. κ and a are obtained from deflectometry measurements. For the selection of the virtual fields w^* and κ^* one needs to take into account theoretical as well as practical restrictions of the problem like continuity, boundary conditions and sensitivity to noise.
The problem can be simplified by assuming the pressure p to be constant over the investigated area and by approximating the integrals with discrete sums.

$$\begin{aligned} p\ =\ \Bigg(&D_{xx}\sum_{i=1}^{N} \kappa^i_{xx}\kappa^{*i}_{xx} + \kappa^i_{yy}\kappa^{*i}_{yy} +\ 2\ \kappa^i_{xy}\kappa^{*i}_{xy}\ ... \\ ... &+\ D_{xy}\sum_{i=1}^{N} \kappa^i_{xx}\kappa^{*i}_{yy} + \kappa^i_{yy}\kappa^{*i}_{xx} -\ 2\ \kappa^i_{xy}\kappa^{*i}_{xy} +\ \rho\ t_S \sum_{i=1}^{N} a^i\ w^{*i}\Bigg)\ \left(\sum_{i=1}^{N} w^{*i}\right)^{-1} \quad . \end{aligned} \tag{2.26}$$

Here, N is the number of discretized surface elements $\mathrm{d}S^i$.

2.4 Virtual Field Definition

For the present problem of identifying an unknown load distribution, it is necessary to choose flexible virtual fields. So-called piecewise virtual fields which are defined over subdomains of the total surface area have been used successfully for similar problems in the past, *e.g.* in Toussaint et al., 2006; Berry et al., 2014; Robin and Berry, 2018; O'Donoughue et al., 2017. 4-node Hermite 16 element shape functions which are also used in FEM (Zienkiewicz, 1977) are employed throughout this study. They enforce the condition for virtual fields for deflections to be C^1 (differentiable with continuous derivatives) and for slopes to be C^0 (continuous), which is necessary for the application in plate bending. Further, they provide slopes and deflections that are zero around the edges, thus eliminating the influence of the unknown reaction forces and moments along the boundaries. The formulation of these shape functions as found in the literature is given in the following (see Pierron and Grédiac, 2012, chapter 14). The virtual deflections are:

$$w^* = \boldsymbol{N}\boldsymbol{q_{DOF}} \quad , \tag{2.27}$$

with the shape functions defined as follows:

$$\begin{aligned}\boldsymbol{N} := (\ & N_{p_1}(\xi_1)N_{q_1}(\xi_2)\ N_{p_2}(\xi_1)N_{q_1}(\xi_2)\ N_{p_1}(\xi_1)N_{q_2}(\xi_2)\ N_{p_2}(\xi_1)N_{q_2}(\xi_2)\ \dots \\ \dots\ & N_{p_3}(\xi_1)N_{q_1}(\xi_2)\ N_{p_4}(\xi_1)N_{q_1}(\xi_2)\ N_{p_3}(\xi_1)N_{q_2}(\xi_2)\ N_{p_4}(\xi_1)N_{q_2}(\xi_2)\ \dots \\ \dots\ & N_{p_3}(\xi_1)N_{q_3}(\xi_2)\ N_{p_4}(\xi_1)N_{q_3}(\xi_2)\ N_{p_3}(\xi_1)N_{q_4}(\xi_2)\ N_{p_4}(\xi_1)N_{q_4}(\xi_2)\ \dots \\ \dots\ & N_{p_1}(\xi_1)N_{q_2}(\xi_2)\ N_{p_2}(\xi_1)\ N_{q_3}(\xi_2)\ N_{p_1}(\xi_1)\ N_{q_4}(\xi_2)\ N_{p_2}(\xi_1)\ N_{q_4}(\xi_2)\ )\end{aligned} \tag{2.28}$$

where ξ_1, ξ_2 are parametric coordinates (see figure 2.2) and

$$\begin{aligned} N_{p_1}(\xi_1) &= \frac{1}{4}(1-\xi_1)^2(2+\xi_1) & N_{q_1}(\xi_2) &= \frac{1}{4}(1-\xi_2)^2(2+\xi_2) \\ N_{p_2}(\xi_1) &= \frac{a_N}{4}(1-\xi_1^2)(1-\xi_1) & N_{q_2}(\xi_2) &= \frac{b_N}{4}(1-\xi_2^2)(1-\xi_2) \\ N_{p_3}(\xi_1) &= \frac{1}{4}(1+\xi_1)^2(2-\xi_1) & N_{q_3}(\xi_2) &= \frac{1}{4}(1+\xi_2)^2(2-\xi_2) \\ N_{p_4}(\xi_1) &= \frac{a_N}{4}(-1+\xi_1^2)(1+\xi_1) & N_{q_4}(\xi_2) &= \frac{b_N}{4}(-1+\xi_2^2)(1+\xi_2) \end{aligned} \tag{2.29}$$

with the side lengths of the element in global coordinates $2a_N$, $2b_N$:

$$\begin{aligned} 2a_N &= x(2) - x(1) = x(3) - x(4) \\ 2b_N &= y(4) - y(1) = y(3) - y(2) \end{aligned} \tag{2.30}$$

$\boldsymbol{q_{DOF}}$ contains the degrees of freedom for each node, which are given by:

$$\begin{aligned} q^*_{DOF,i,1} &= w^* & q^*_{DOF,i2} &= \partial_x w^* \\ q^*_{DOF,i,3} &= \partial_y w^* & q^*_{DOF,i,4} &= \partial_x \partial_y w^* \end{aligned} \tag{2.31}$$

Here, all degrees of freedom were set to zero except for the virtual deflection of the center node, which was set to 1. Fig. 2.3 shows example virtual fields for the deflections and curvatures.

The virtual fields are defined over a window of chosen size and shifted over the entire surface S. One pressure value is calculated for each window. Throughout this study, this window is referred to as pressure reconstruction window, PRW.

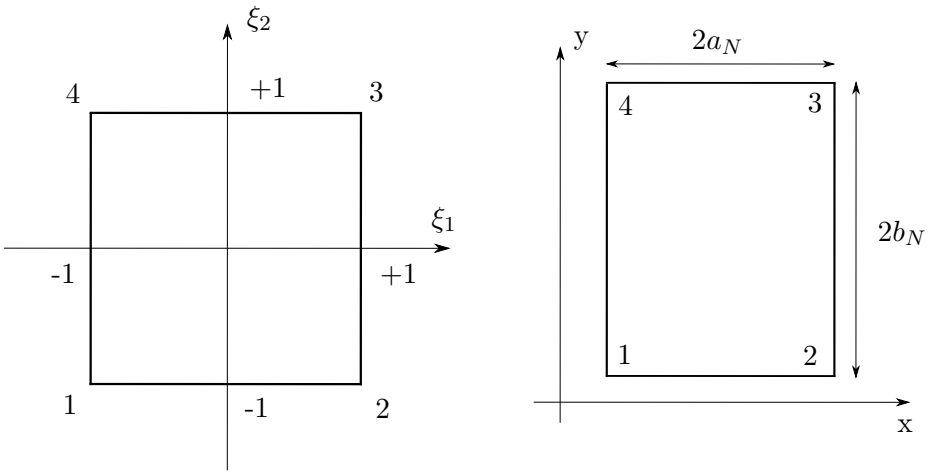

(a) Local coordinates. (b) Global coordinates.

Figure 2.2: Rectangular element for bending plates (redrawn from (Pierron and Grédiac, 2012, chapter 3.9.3)).

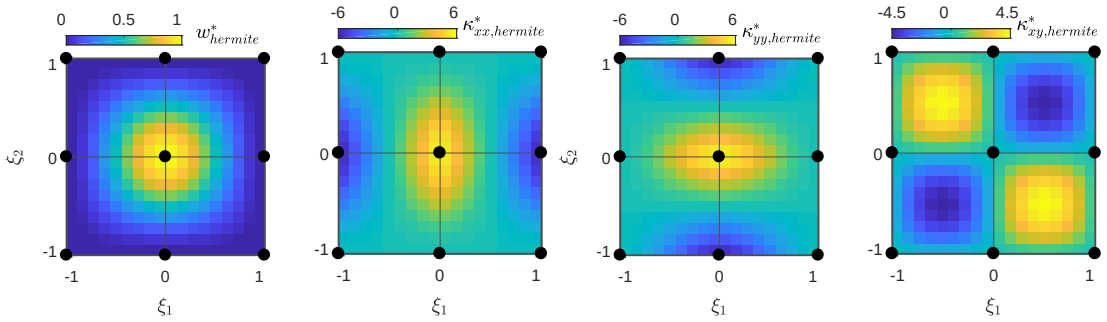

(a) Virtual displacements w^* (b) Virtual curvatures k^*_{xx} (c) Virtual curvatures k^*_{yy} (d) Virtual curvatures k^*_{xy}

Figure 2.3: Example Hermite 16 virtual fields with superimposed virtual elements and nodes (black). ξ_1, ξ_2 are parametric coordinates.

Chapter 3

Experimental Methods

This chapter introduces the general experimental setup and components. The experimental parameters as well as details of the three separate experiments can be found in the respective papers in Part II of this thesis.

3.1 Setup

A basic schematic setup of the experimental setup is shown in fig. 3.1. Air jets were used to apply pressure on the specimen. The specimen was glued around the borders on a square acrylic frame. The cross-hatched grid that was used as spatial carrier was printed on transparency and fixed between two glass plates in the setup. A white light source was placed behind it. The camera was placed next to the grid with the image sensor at the same distance from the sample and such that the reflected grid image was recorded at normal incidence. The distance between grid and sample was chosen to be as large as possible in order to minimise the angle θ (see fig. 2.1). All relevant experimental parameters are given in the respective papers in Part II of this thesis.

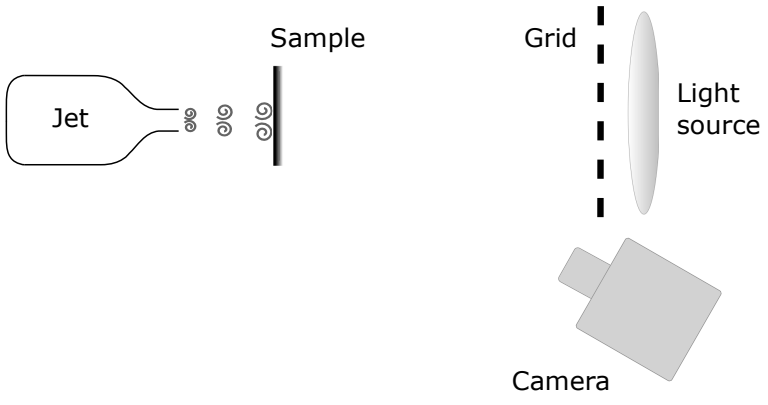

Figure 3.1: Experimental setup.

3.2 Sample

The choice of the specimen sets some crucial limitations for the experimental approach. The surface finish has to be sufficiently smooth to allow specular reflection of the small grid pitches. Glass mirrors proved suitable for the present setups. Further, the thickness of the investigated plate has to be chosen with respect to the expected loads. Surface deformations have to be large enough to be detected by the deflectometry setup. For large deformations however, the thin plate assumptions do not hold, resulting in an error. Finite element simulations were used to determine suitable sample thicknesses. In case of the loads investigated in papers 1 and 2, it was found that for the Gaussian distributions with ca. 600 Pa peak pressure and a 1 mm grid pitch, the plate should not be thicker than 3 mm to detect the local slopes. However, using a 0.7 mm thick glass plate would have resulted in deviations from the thin plate theory causing local errors in curvature of up to ca. 30%. Good results were achieved with a thickness of 1 mm, where the identified corresponding errors in curvature were well below 1%. Finally, mounting the specimen requires some care because particularly thin plates are prone to deform, making it harder to align the setup components and potentially inducing errors in the measured slopes.

3.3 Light Source

Selecting suitable light sources was an important part of the experiments. For low shutter speeds, a standard 500 W halogen lamp was used, which could easily be replaced by other white light sources. For higher shutter speeds however, a more powerful light source was required. 2000 W halogen lights were tested, but produced too much heat, damaging the printed grid and other nearby components and heating up the camera. The heat can further cause density fluctuations in the air between grid, sample and camera, distorting the light beams. Instead, a custom LED panel was built out of 9 100 W LED chips. In case of the phase-locked measurements conducted in paper 3, experiments lasted for several hours despite the high shutter speed. As the LED panel would heat up and take damage when operated over such long times, it was replaced with a Bowens Gemini Pro 1000 Flash light.

3.4 Jets

Different kinds of impinging jets were used to apply loads on the specimen. These jets were chosen as generic applications of fluid dynamics. Both types of jet are well described in the literature, which facilliated the planning of the setups and allowed confirming the validity of the results obtained with VFM reconstructions from deflectometry measurements. For paper 1 and 2 a round, fan-driven air jet was used. A honeycomb was placed behind the fan to reduce turbulence and achieve a laminar flow region around the jet core at nozzle exit. Fig. 3.2 shows a schematic of the jet. The 3D printed jet had a nozzle diameter of 5 cm. It was

modified with a 3D printed nozzle extension, reducing the nozzle diameter from to 2 cm. Due to the relatively rough surface structure of the extension, the jet was fully turbulent after a short distance downstream from the nozzle exit.
For paper 3, a synthetic jet was used. It was actuated using an acoustic speaker connected to a cavity which was milled out of aluminium. A curved, converging nozzle with rectangular shape was 3D printed and fit into the cavity. A schematic of the synthetic jet can be found in fig. 3.3.
Information on the relevant physics of these jets is given in the respective papers in Part II of this thesis.

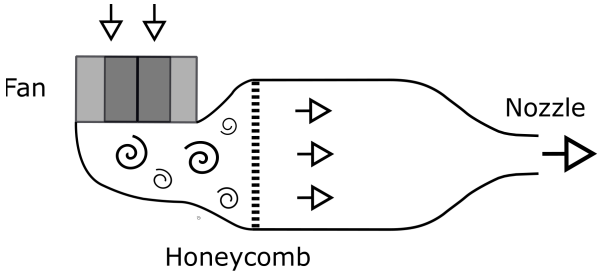

Figure 3.2: Schematic of the fan-driven jet.

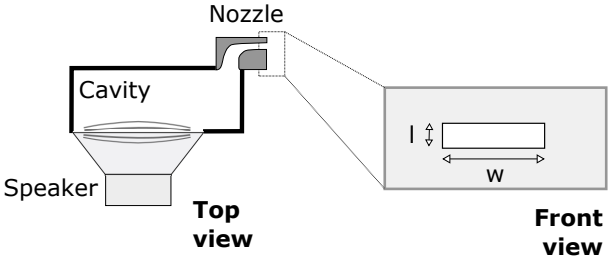

Figure 3.3: Schematic of the synthetic jet. l, w are the slot length and width respectively.

3.5 Transducer Measurements

Pressure sensors were used for comparison with VFM reconstruction results. Endevco 8507C-2 type piezoresistive pressure transducers were employed. Pressure acting on such sensors causes deformations which result in a change of the electric resistance. The latter can then be measured using a Wheatstone bridge. Here, a NI PXIe-4330 module was used for these measurements.

Chapter 4

Paper Overview and Conclusions

The main content of this work is presented in the three papers which can be found in Part II of this thesis. Paper 1 has been submitted for review. As paper 2 and 3 rely on several core references to paper 1, they will be submitted as soon as the latter has been accepted. This chapter provides a brief overview of the content and conclusions of the three papers. Supervision and remarks on all papers have been given by B. Ganapathisubramani and F. Pierron.

Paper 1

Kaufmann, R., Ganapathisubramani, B. and Pierron, F. (accepted 13.06.2019). Full-field surface pressure reconstruction using the Virtual Fields Method, *Journal of Experimental Mechanics*.

This study addresses the reconstruction of static pressure distributions from time-averaged slope measurements. The technique was demonstrated on a round air jet impinging on a flat plate specimen. VFM pressure reconstructions were compared to transducer measurements. The study also introduces an approach for simulating the conducted experiments numerically. This was used for the assessment of systematic errors and the accuracy of the pressure reconstruction results. Experimental error sources were investigated by comparing pressure reconstructions from deflectometry data to pressure transducer measurements and to numerical simulations. Finally, a finite element correction procedure was introduced to compensate for the identified systematic processing error.

Paper 2

Kaufmann, R., Pierron, F. and Ganapathisubramani, B. (unpublished). Reconstruction of surface pressure fluctuations using deflectometry and the Virtual Fields Method. *Intended for submission to the Journal Experiments in Fluids*

This paper investigates dynamic pressure distributions induced by a round, impinging air jet. Time-resolved slope data was processed to obtain instantaneous VFM pressure reconstructions. Temporal filters were employed to extract statistical properties, which were compared to data obtained with pressure transducer measurements. Dynamic Mode Decomposition (DMD) was

used to extract information on relevant spatial-temporal events. The capabilities and limitations of this approach were discussed in detail.

Paper 3

Kaufmann, R., Pierron, F. and Ganapathisubramani, B. (unpublished). Surface pressure reconstruction from phase-averaged deflectometry measurements using the Virtual Fields Method. *Intended for submission to the Journal of Experimental Mechanics*

The third paper, *Surface pressure reconstruction from phase-averaged deflectometry measurements using the Virtual Fields Method*, investigates the capabilities and limitations of phase-locked deflectometry measurements as basis for pressure reconstructions. This allowed capturing information on dynamic flow events induced by an impinging synthetic jet without the necessity to employ temporal filters. Both the pressure amplitudes and the shapes of the spatial structures occurring during different phases and for different jet settings were investigated. Error sources were identified and the limitations and challenges for future applications were discussed.

Part II

Papers

Paper 1

Full-field surface pressure reconstruction using the Virtual Fields Method

R. Kaufmann, B. Ganapathisubramani, F. Pierron

Faculty of Engineering and Physical Sciences, University of Southampton, Southampton SO17 1BJ, UK

Submitted for review to the Journal of Experimental Mechanics, January 2019

Abstract This work presents a methodology for reconstructing full-field surface pressure information from deflectometry measurements on a thin plate using the Virtual Fields Method (VFM). Low-amplitude pressure distributions of the order of few $\mathcal{O}(100)$ Pa from an impinging air jet are investigated. These are commonly measured point-wise using arrays of pressure transducers, which require drilling holes into the specimen. In contrast, the approach presented here allows obtaining a large number of data points on the investigated specimen without impact on surface properties and flow.
Deflectometry provides full-field deformation data on the specimen surface with remarkably high sensitivity. The VFM allows extracting information from the full-field data using the principle of virtual work. A finite element model is employed in combination with artificial grid deformation to assess the uncertainty of the pressure reconstructions. Both experimental and model data are presented and compared to show capabilities and restrictions of this method.

1 Introduction

Full-field surface pressure measurements are highly relevant for engineering applications like material testing, component design in aerodynamics and the use of impinging jets for cooling, de-icing and drying. Surface pressure information can be used to determine aerodynamic loads (Usherwood, 2009) and to evaluate the performance of impinging jets used for heat and mass transfer (N. B. Livingood and Hrycak, 1973). They are however difficult to achieve, as available methods are not universally applicable. Most commonly, large numbers of pressure transducers are fitted into the investigated surface. This is an invasive technique as it requires one to drill holes into the sample. Further, it yields limited spatial resolution (Corcos, 1963, 1964). Pressure sensitive paints allow obtaining full-field data, but are not suited for low-range differential pressure measurements (Tropea et al., 2007; Yang et al., 2012, chapter 4.4). They further require extensive calibration efforts, as well as a controlled experimental environment. Calculating pressure from Particle Image Velocimetry (PIV) is a non-invasive method that yields full-field data in the flow field (van Oudheusden, 2013; Ragni et al., 2009). This allows estimations of surface pressure only along lines where the field of view capturing the flow field coincides with the surface.

Another approach is the reconstruction of pressure information from full-field surface deformation measurements by solving the local equilibrium equations. Recently, wall pressure was calculated from 3D-Digital Image Correlation (DIC) measurements on a flexible Kevlar wind-tunnel wall in an anechoic chamber (Brown et al., 2018). This was achieved by projecting the measured deflections onto polynomial basis functions and inserting their derivatives into the corresponding equilibrium equations. The obtained pressure coefficients compared well to transducer data for the relatively large spatial scales that were investigated. Many problems in the field of fluid-structure interactions can be simplified to low amplitude loads acting on thin plates. This allows employing the Love-Kirchhoff thin plate theory (Timoshenko and Woinowsky-Krieger, 1959) to write the local equilibrium of the plate. The required full-field deformation information on the test surface can be obtained using a number of measurement techniques, *e.g.* DIC, Laser Doppler Vibrometers (LDV) or interferometry techniques. However, the fourth order deflection derivatives required to solve the Love-Kirchhoff equilibrium equation make an application in the presence of experimental noise challenging, particularly for low signal-to-noise ratios. To a degree, this issue can be addressed by applying regularisation techniques. In studies based on solving the equilibrium equation locally by employing a finite difference scheme, regularisation was achieved by applying wave number filters (Pezerat and Guyader, 2000) or by adapting the number of data points used for the finite differences (Leclére and Pézerat, 2012). This allowed an identification and localisation of external vibration sources acting on the investigated specimen. Similarly, the acoustic component of a flow was identified using wave number filters in an investigation of a turbulent boundary layer (Lecoq et al., 2014). Generally, the accuracy of this approach in terms of localisation and amplitude identification depends strongly on the chosen regularisation.

An alternative for solving the thin plate problem using full-field data is the Virtual Fields Method (VFM), which is based on the principle of virtual work and only requires second order deflection derivatives. The VFM is an inverse method that uses full-field kinematic measurements to identify mechanical material properties from known loading or *vice versa*. A detailed overview of the method and the range of applications is given in Pierron and Grédiac, 2012. It notably does not require detailed knowledge of the boundary conditions and does not rely on computationally expensive iterative procedures. A study comparing Finite Element Model Updating, the Constitutive Equation Gap Method and the VFM for constitutive mechanical models using full-field measurements found that the VFM consistently performed best in terms of computational cost with reasonable results (Martins et al., 2018). The VFM has been adapted for load reconstruction in a number of studies, including dynamic load identification in a Hopkinson bar (Moulart et al., 2011 Pierron et al., 2011). The data were found to compare reasonably well to standard measurement techniques. The VFM was also used to reconstruct spatially-averaged sound pressure levels from an acoustic field using a scanning Laser Doppler Vibrometer (LDV) (Robin and Berry, 2018). Dynamic transverse loads, as well as vibrations caused by acoustic pressure were identified using the same technique in Berry et al., 2014. The results were found to be accurate for distributed loads. The latter used a VFM approach based on piecewise virtual fields, which allows more accurate descriptions of boundary conditions for complex shapes and heterogeneous materials (Toussaint et al., 2006). This approach

was extended to random spatial wall pressure excitations in Berry and Robin, 2016, reconstructing power spectral density functions from measured data and using the VFM to describe the plate response. The authors found that this method requires piecewise virtual fields to be defined over small regions. Recently, the VFM approach was combined with deflectometry for the identification of mechanical point loads of several $\mathcal{O}(1)$ N (O'Donoughue et al., 2017). Deflectometry is a highly sensitive technique for slope measurement (Surrel et al., 1999). It was successfully used in a range of applications like damage detection of composites (Devivier et al., 2012), the analysis of stiffness and damping parameters of vibrating plates (Giraudeau et al., 2010) and for imaging of ultrasonic Lamb waves (Devivier et al., 2016). Since deflectometry measurements yield surface slopes, the combination with the VFM reduces the required order of derivatives of experimental data for pressure reconstruction to one. Known loads were reconstructed in O'Donoughue et al., 2017 with good accuracy for certain reconstruction window sizes which were found empirically. Deflectometry and the VFM were also used to identify pressure auto-spectra of spatially averaged random excitations in O'Donoughue et al., 2019. The results agreed well with microphone array measurements, except at the structural resonance frequencies and for poor signal-to-noise-ratios. In the same study, the VFM approach was extended to membranes and the applicability was investigated using a simulated experiment. A shortcoming of these previous studies was that the accuracy was not assessed for unknown input loads. This is an important step because neither the resolution in space nor the uncertainty in pressure amplitude can be predicted directly as they depend on the signal amplitude and distribution, the noise level and the reconstruction parameters.
The main focus of the work presented here is the determination of static low-amplitude pressure distributions with peak values of few $\mathcal{O}(100)$ Pa from time-averaged full-field slope measurements, as well as an assessment of the uncertainties of the method. In the following sections 2 and 3, a brief overview of the theoretical background and experimental setup is given. In section 4, experimental results are presented for two different specimen and for several reconstruction parameters. The pressure reconstructions are compared to pressure transducer measurements. Section 5 introduces a numerical model for simulated experiments. This allows an assessment of the uncertainty of the method in terms of both systematic errors and the influence of random noise. In section 5, a finite element updating procedure is proposed to compensate for systematic errors.

2 Theory

2.1 Impinging Jets

A fan-driven, round air jet was used to apply a load on the specimen. The flow generated by this impinging jet can be divided into the free jet, stagnation and wall region (Kalifa et al., 2016). These regions, shown in fig. 1, consist of subregions with distinct flow features which are governed by the ratio between downstream distance and nozzle diameter H/D and Reynolds number Re. Directly downstream from the nozzle exit, the free jet develops for

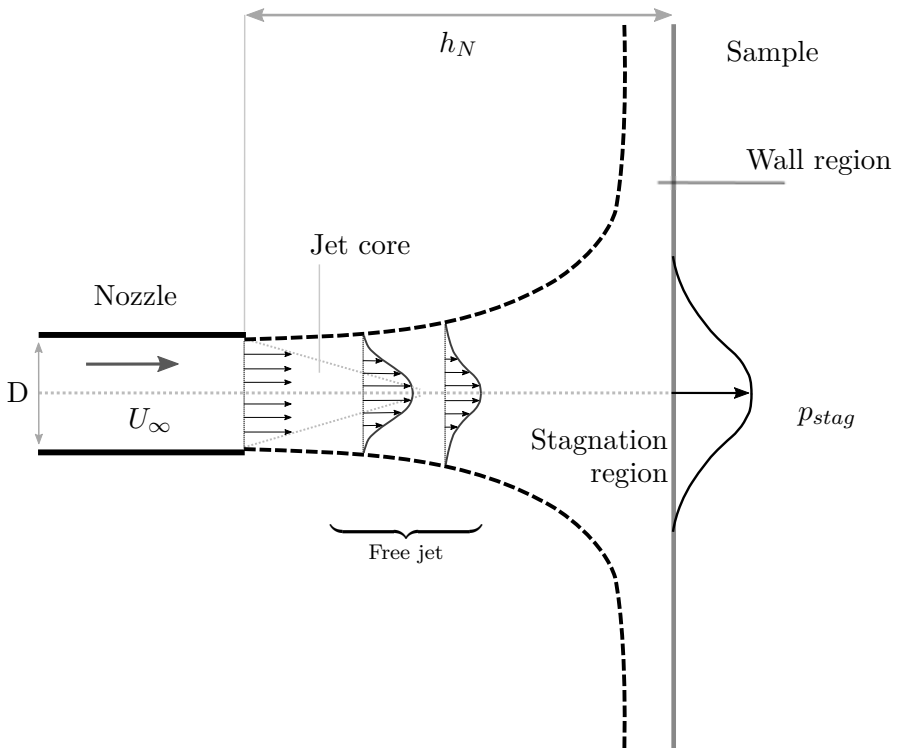

Figure 1: Impinging jet regions.

sufficiently large $H/D \gtrsim 2$ (Zuckerman and Lior, 2006). The velocity profile spreads as it moves downstream due to entrainment and viscous diffusion causing a transfer of momentum to surrounding fluid particles. Upon approaching the impingement plate a stagnation region forms, characterized by an increase in static pressure up to the stagnation point on the plate surface. The rising static pressure results in pressure gradients diverting the flow radially away from the jet centerline. The laterally diverted flow forms the wall region. The pressure distribution on the impingement surface is approximately Gaussian (Beltaos, 1976). This study focuses on the measurement of the mean load distribution on the impingement plate.

2.2 Deflectometry

Deflectometry is an optical full-field measurement technique for surface slopes, Surrel et al., 1999. Fig. 2 shows a schematic of the setup. A camera measures the reflected image of a periodic spatial signal, here a cross-hatched grid, on the surface of a specular reflective sample. The distance between the grid and sample is denoted by h_G and the grid pitch by p_G. The angle θ has to be sufficiently small to minimize grid distortion in the recorded image. A pixel directed at point M on the specimen surface will image the reflected grid at point P in an unloaded configuration. If a load is applied to the surface, it deforms locally and the same pixel will now image the reflected grid at point P$'$. It is assumed here that rigid body movements and out of plane deflections are negligible (for details see section 7 below). The displacement $\boldsymbol{u}$ between P and P$'$ relates to the phase difference dϕ in the grid signal in x-

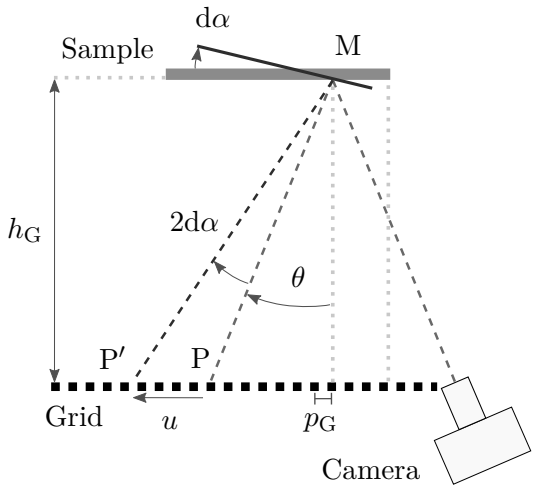

Figure 2: Deflectometry setup, top view.

and y-direction respectively as follows:

$$d\phi_x = \frac{2\pi}{p_G} u_x, \quad d\phi_y = \frac{2\pi}{p_G} u_y \tag{1}$$

A spatial shift by one grid pitch p_G corresponds to a phase shift of 2π. However, a direct displacement estimation from the phase difference between a reference and a deformed image does not take into account that the physical point on the plate surface is subject to a small in-plane displacement. An iterative procedure to improve the displacement results given in Grédiac et al., 2016, section 4.2 is employed here:

$$\boldsymbol{u}_{n+1}(\boldsymbol{x}) = -\frac{p_G}{2\pi}(\phi_{def}(\boldsymbol{x} + \boldsymbol{u}_n(\boldsymbol{x})) - \phi_{ref}(\boldsymbol{x})) \ , \tag{2}$$

with the phases of the deformed and reference configurations, ϕ_{def} and ϕ_{ref} respectively. A relationship between slopes and displacement is derived *e.g.* in (Ritter, 1982). It is based on geometric considerations and assumes that α is sufficiently small, so the camera records images in normal incidence and h_G is large against the shift $\boldsymbol{u}$:

$$d\alpha_x = \frac{u_x}{2h_G}, \quad d\alpha_y = \frac{u_y}{2h_G} \tag{3}$$

Otherwise, a more complex calibration is required, Balzer and Werling, 2010; Surrel and Pierron, 2019. Equation 3 will be used here.

The spatial resolution of the method is driven by p_G. The phase resolution is noise dependent and can be defined as the standard deviation of a phase map detected between two stationary images. Consequently, slope resolution depends on p_G, h_G and the phase resolution.

Phase detection

The literature describes a number of methods for retrieving phase information from grid images, *e.g.* Surrel, 2000; Dai et al., 2014; Grédiac et al., 2016. Here, a spatial phase-stepping

algorithm is employed which allows investigating dynamic events, Surrel, 1996; Poon et al., 1993. One phase map is calculated per image. The chosen algorithm needs to be capable of coping with miscalibration, *i.e.* a slightly non-integer number of pixels per grid period. This can occur due to imperfections in the printed grid, misalignment between camera, sample and grid, lens distortion, as well as fill factor issues, which can lead to sampling issues. In addition, the investigated signal is not generally sinusoidal. This requires an algorithm suppressing harmonics and sets a lower limit to the required number of samples, *i.e.* pixels recorded per grid pitch, Hibino et al., 1995. A windowed discrete Fourier transform algorithm using triangular weighting and a detection kernel size of two grid periods as used in *e.g.* Surrel, 2000 and (Badulescu et al., 2009) will be used in this study.

2.3 Pressure Reconstruction

The problem investigated here is a thin plate in pure bending, which allows the Love-Kirchhoff theory to be employed (Dym and Shames, 1973). Assuming that the plate material is linear elastic, isotropic and homogeneous, the principle of virtual work is expressed by:

$$\begin{aligned} \int_S p\ w^* dS \ &= \ D_{xx} \int_S \left(\kappa_{xx}\kappa^*_{xx} + \kappa_{yy}\kappa^*_{yy} + 2\ \kappa_{xy}\kappa^*_{xy} \right) dS \\ &+\ D_{xy} \int_S \left(\kappa_{xx}\kappa^*_{yy} + \kappa_{yy}\kappa^*_{xx} - 2\ \kappa_{xy}\kappa^*_{xy} \right) dS + \ \rho\ t_S \int_S a\ w^* dS \quad . \end{aligned} \tag{4}$$

S is the surface area, p the investigated pressure, D_{xx} and D_{xy} the plate bending stiffness matrix components, κ the curvatures, ρ the plate material density, t_S the plate thickness, a the acceleration, w^* the virtual deflection and κ^* the virtual curvatures. Here, the parameters D_{xx}, D_{xy}, ρ and t_S are known from the plate manufacturer. κ and a are obtained from deflectometry measurements, see section 3.5 below. For the selection of the virtual fields w^* and κ^* one needs to take into account theoretical as well as practical restrictions of the problem like continuity, boundary conditions and sensitivity to noise.
The problem can be simplified by assuming the pressure p to be constant over the investigated area and by approximating the integrals with discrete sums.

$$\begin{aligned} p \ = \ \Bigg(& D_{xx} \sum_{i=1}^{N} \kappa^i_{xx}\kappa^{*i}_{xx} + \kappa^i_{yy}\kappa^{*i}_{yy} + 2\ \kappa^i_{xy}\kappa^{*i}_{xy} \\ & + \ D_{xy} \sum_{i=1}^{N} \kappa^i_{xx}\kappa^{*i}_{yy} + \kappa^i_{yy}\kappa^{*i}_{xx} - 2\ \kappa^i_{xy}\kappa^{*i}_{xy} + \ \rho\ t_S \sum_{i=1}^{N} a^i\ w^{*i} \Bigg) \left(\sum_{i=1}^{N} w^{*i} \right)^{-1} \quad . \end{aligned} \tag{5}$$

Here, N is the number of discretised surface elements dS^i.

2.4 Virtual Fields

For the present problem of identifying an unknown load distribution, it is beneficial to choose piecewise virtual fields due to their flexibility (Toussaint et al., 2006; Berry et al., 2014; Robin and Berry, 2018; O'Donoughue et al., 2017). In this study, the virtual fields are defined over a window of chosen size which is then shifted over the surface S until the entire area is covered. One pressure value is calculated for each window. In the following, this window will be referred to as pressure reconstruction window PRW. This procedure also allows for oversampling in the spatial reconstruction by shifting the window by less than a full window size.

Here, the only theoretical requirements for the virtual fields are continuity and differentiability. Since curvatures relate to deflections through their second spatial derivatives for a thin plate in pure bending, the virtual deflections are required to be C^1 continuous. It is further necessary to eliminate the unknown contributions of virtual work along the plate boundaries. This is achieved by choosing virtual displacements and slopes that are zero around the window borders. 4-node Hermite 16 element shape functions as used in FEM (Zienkiewicz, 1977) fulfill these requirements. The full equations defining these functions can be found in Pierron and Grédiac, 2012, chapter 14. Fig. 3 shows example virtual fields. 9 nodes are defined for a PRW. All degrees of freedom are set to zero except for the virtual deflection of the center node, which is set to 1.

The size of the PRW is an important parameter for the pressure reconstruction. Generally, the presence of random noise requires a larger PRW in order to average out the effect of noise on the pressure value within the window. A smaller PRW however can perform better at capturing small scale spatial structures, as large windows may average out amplitude peaks. One challenge in varying the window size is that the systematic error varies with it, as well as the effect of random noise on pressure reconstruction. This problem is investigated numerically in section 5.

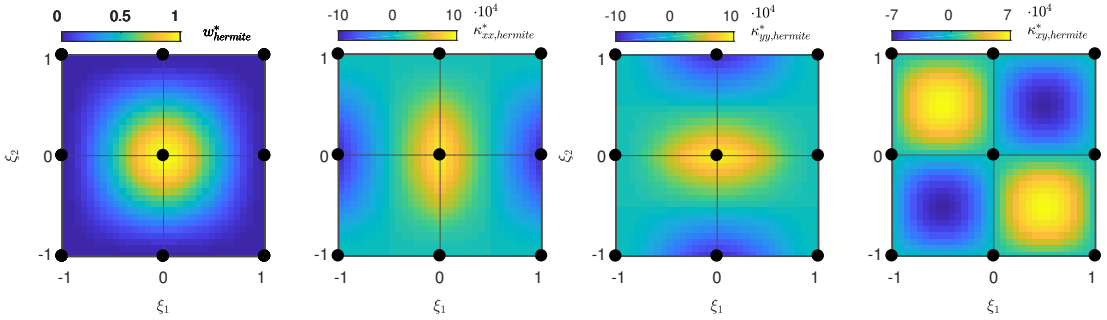

(a) Virtual displacements w^* (b) Virtual curvatures k^*_{xx} (c) Virtual curvatures k^*_{yy} (d) Virtual curvatures k^*_{xy}

Figure 3: Example Hermite 16 virtual fields with superimposed virtual elements and nodes (black). ξ_1, ξ_2 are parametric coordinates. The example window size is 32 points in each direction. Full equations can be found in Pierron and Grédiac, 2012, chapter 14.

3 Experimental Methods

3.1 Setup

Fig. 4 shows a schematic of the experimental setup. A round, fan-driven impinging air jet was used to apply pressure on the specimen. The jet was fully turbulent at a downstream distance of 1 cm from the nozzle exit. The specimen was glued on a square acrylic frame. The grid was printed on transparency and fixed between two glass plates in the setup. A white light source was placed behind it. The camera was placed next to the grid at the same distance from the sample such that the reflected grid image is recorded at normal incidence. The distance between the sample and grid was chosen to be as large as possible in order to minimise the angle θ (see fig. 2). Two different glass sample plates were investigated, one with thickness of 1 mm and the other 3 mm. All relevant experimental parameters are listed in table 1.

3.2 Grid

A cross-hatched grid printed on a transparency was used as the spatial carrier. Sine grids printed in x- and y-direction would be preferable for phase detection as they do not induce high frequency harmonics in the phase detection. Printing these in sufficient quality is however difficult to achieve with standard printers. Using a hatched grid and slightly defocusing the image achieves a similar result because the discrete black and white areas become blurred, effectively yielding a grey scale transition between minimum and maximum intensity. This does however result in a slightly lower signal to noise ratio. It should be noted that when printing the grid, an integer number of printed dots per half pitch is required to avoid aliasing (*e.g.* Devivier, 2012). For the current setup, grids with 1 mm pitch were printed on transparencies using a *Konica Minolta bizhub C652* printers at 600 dpi.

3.3 Sample

The choice of the sample plate material and finish proved crucial for the investigation of small pressure amplitudes and spatial scales. The surface slopes under loading need to be large

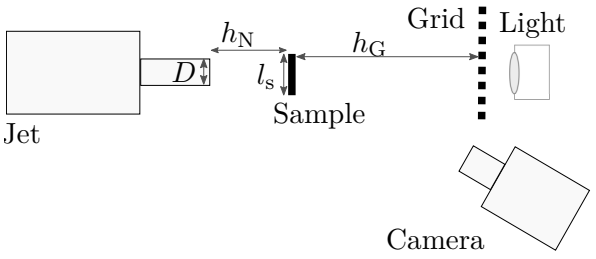

Figure 4: Experimental setup.

enough for detection, while at the same time the sample surface has to be plane enough for the grid image to be sufficiently in focus over the entire field of view. Perspex mirrors, polished aluminium and glass plates with reflective foils proved either too diffusive due to the Rayleigh criterion or insufficiently plane, resulting in a lack of depth of field when trying to image the reflected grid. Optical glass mirrors were chosen instead, as they provide adequate stiffness parameters and remain sufficiently plane when mounted. As it was possible to estimate the slope resolution from the noise level observed when recording two undeformed images on any sample thickness, deformation estimations based on the expected experimental load were used as input for finite element simulations to select suitable plate parameters. It was found that plates with thickness of 3 mm or lower were required. Good results were achieved using a 1 mm thick first-surface glass mirror as specimen. Still, fitting the 1 mm glass mirror on the frame caused it to bend slightly, resulting in small deviations from a perfect plane and subsequent local lack of depth of field. This was addressed by closing the aperture. A second, 3 mm thick mirror was used for comparison as it did not bend notably when mounted, though signal amplitudes for this case proved to be very low. The sample plates were glued onto a perspex frame along all edges, resulting in simply supported boundary conditions. The frame thickness of 10 mm was sufficient to prevent noticeable deformations during the tests (see also section 7).

3.4 Transducer Measurements

Pressure transducer measurements allowed a validation of the pressure reconstructions from deflectometry and the VFM. Endevco 8507C-2 type transducers were fitted in an aluminium plate along a line from the stagnation point outwards. The transducers have a diameter of 2.5 mm and were fitted with a spacing of 5 mm. They were fitted to be flush with the surface to within approximately 0.5 mm. Data was acquired at 10 kHz over 20 s using a NI PXIe-4330 module.

3.5 Data Acquisition and Processing

One reference image was taken in an unloaded configuration before activating the jet. The jet required approximately 20 s to settle, after which a series of images was recorded. One data point was calculated per grid pitch during phase detection. Slopes were calculated relative to the reference image. Time averaged mean slope maps were calculated over $N = 5400$ measurements at 50 Hz, limited by camera storage. From the slope maps the curvatures were obtained through spatial differentiation using centered finite differences. This requires knowledge of the physical distance between two data points on the specimen. It corresponds to the portion of the mirror required to observe the reflection of one grid pitch, which can be determined geometrically assuming θ is sufficiently small (see fig. 2). In the present setup, camera sensor and grid were at the same distance from the mirror h_G, such that the distance was half a printed grid pitch. Since differentiation tends to amplify the effect of noise, it can

Optics		
Camera		Photron Fastcam SA1.1
Technology		CMOS
Camera pixel size		20 μm
Surface Fill Factor		52 %
Dynamic range		12 bit
Settings		
Resolution		1024×1024 pixels
Frame rate	f	50 fps
Exposure		1/100 s
Region of interest		64×64 mm^2
Magnification	M	0.32
f-number	N_{Lens}	32
Focal length	f_{Lens}	300 mm
Light source		Halogen, 500 W
Sample		
Type		First-surface mirror
Material		Glass
Young's modulus	E	74 GPa
Poisson's ratio	ν	0.23
Density	ρ	2.5 10^3 kg m^{-3}
Thickness	t_{S}	1 mm, 3 mm
Side length	l_{s}	ca. 90 mm, 190 mm
Grid		
Printed grid pitch	p_{G}	1.02 mm
Grid-sample distance	h_{G}	1.03 m
Pixels per pitch	ppp	8
Jet		
Nozzle shape		Round
Nozzle diameter	D	20 mm
Area contraction ratio		0.13
Nozzle exit dynamic pressure	p_{exit}	630 Pa
Air density	ρ_{air}	1.17 kg m^{-3}
Reynold's number	Re	4·10^4
Sample-nozzle distance	h_{N}	40 mm

Table 1: Setup parameters.

be beneficial to filter slope data before calculating curvatures. Here, the mean slopes were filtered using a 2D Gaussian filter, performing a convolution in the spatial domain. The filter kernel is characterized by its side length which is determined by the standard deviation, here denoted σ_α, and truncated at 3 σ_α in both directions. Because of its size, the filter kernel cannot be applied to the data points at the border of the field of view without padding. As padding should be avoided to prevent bias, 6 $\sigma_\alpha - 1$ data points were cropped along the edges of the field of view. While acting as a low-pass filter which reduces the effect of random noise, this technique also tends to reduce signal amplitude.

For the investigated problem of a mean flow profile, the accelerations average out to zero. This was confirmed with vibrometer measurements on several points along the test surface using a Polytec PDV 100 Portable Digital Vibrometer. Data was acquired at 4 kHz over 20 s. The noise level in LDV measurements was 0.3 ms^{-2}. The observed standard deviations varied with the position along the plate surface and reached up to 1.4 ms^{-2}. Therefore, the term involving accelerations in equation 4 is zero as well and will therefore be neglected in the following.
Pressure reconstructions were conducted for several PRW sizes. The results were oversampled by shifting the PRW over the investigated field of view by one data point per iteration. Note that due to the finite size of these windows, half a PRW of data points is lost around the edges of the field of view.

4 Experimental Results

Slope maps obtained from deflectometry measurements were processed and temporally averaged as described in section 3.5. Results for both specimens are presented in the following, one plate with 1 mm thickness and 90 mm side length, and one with 3 mm thickness and 190 mm side length. The region of interest is 64 mm in both directions for each test cases. Fig. 5a-5d show the measured mean slope maps for both test plates. Distances are given in terms of radial distance from the impinging jet's stagnation point r, normalized by the nozzle diameter D, in x- and y-direction respectively. Note that the region of interest showing the jet center does not coincide with the plate center, so the slope amplitudes are not necessarily symmetric. The signal amplitudes for the 3 mm test case are significantly lower than for the 1 mm case. Slope shapes are different for both cases because the plates have different side length while the field of view remains the same size. Further, the stagnation point is off-center in the 3 mm test.
Fig. 5e-5p shows mean curvature maps with and without Gaussian filter. Stripes are visible in all curvature maps for the unfiltered 1 mm test data. This indicates the presence of a systematic error source in the experimental setup. Without slope filter, curvatures obtained from the 3 mm plate test are governed by noise. The curvature map for $\bar{\kappa}_{xx}$ (fig. 5g) additionally shows fringes. These disappear after slope filtering, though filtered data still appear asymmetric, again indicating a systematic error. To assure that this issue occurring in for both plates does not originate from a lack of convergence, mean and instantaneous curvature maps were calculated and compared. All maps show the same bias, with small variations in amplitude.
This may be caused by misalignment between grid and image sensor due to imperfections in the printed grid, combined with the CMOS chip's fill factor. This results in a slightly varying number of pixels per grid pitch over the field of view, which leads to errors in phase detection and fringes. While this issue could be mitigated by careful realignment of camera and grid as well as slightly defocusing the image to address the low camera fill factor, it could not be fully eliminated. Another possible error source is the deviation of the plate surface from a perfect plane, *e.g.* due to deformations of the sample during mounting. Since differentiation

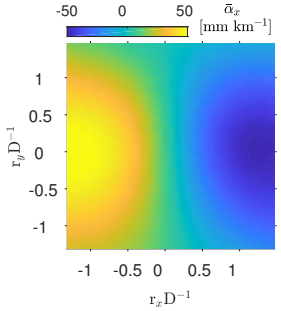

(a) $\bar{\alpha}_x$ for $t_S = 1$ mm plate test.

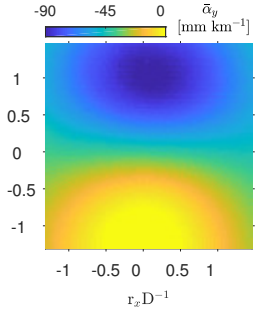

(b) $\bar{\alpha}_y$ for $t_S = 1$ mm plate test.

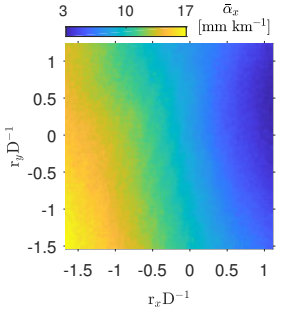

(c) $\bar{\alpha}_x$ for $t_S = 3$ mm plate test.

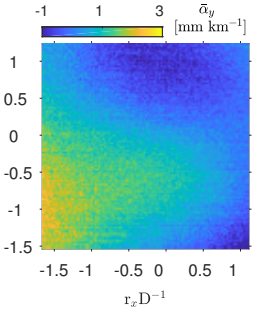

(d) $\bar{\alpha}_y$ for $t_S = 3$ mm plate test.

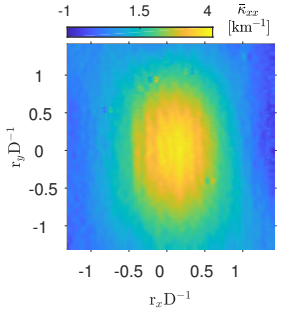

(e) $\bar{\kappa}_{xx}$ from unfiltered slopes for $t_S = 1$ mm plate test.

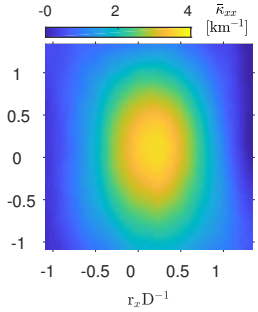

(f) $\bar{\kappa}_{xx}$ from filtered slopes for $t_S = 1$ mm plate test, $\sigma_\alpha = 3$.

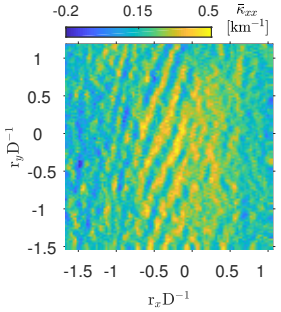

(g) $\bar{\kappa}_{xx}$ from unfiltered slopes for $t_S = 3$ mm plate test. .

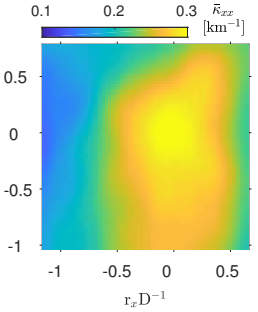

(h) $\bar{\kappa}_{xx}$ from filtered slopes for $t_S = 3$ mm plate test, $\sigma_\alpha = 6$.

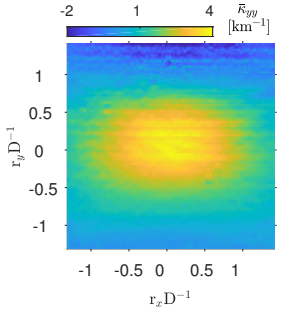

(i) $\bar{\kappa}_{yy}$ from unfiltered slopes for $t_S = 1$ mm plate test.

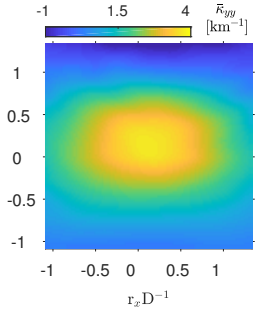

(j) $\bar{\kappa}_{yy}$ from filtered slopes, $\sigma_\alpha = 3$ for $t_S = 1$ mm plate test.

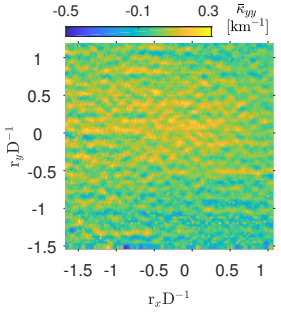

(k) $\bar{\kappa}_{yy}$ from unfiltered slopes for $t_S = 3$ mm plate test.

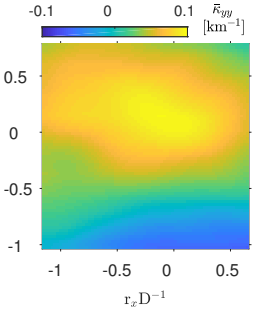

(l) $\bar{\kappa}_{yy}$ from filtered slopes for $t_S = 3$ mm plate test, $\sigma_\alpha = 6$.

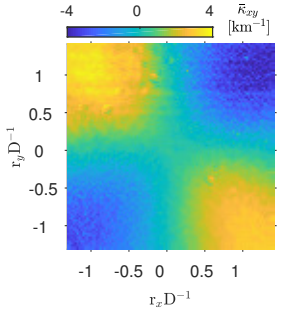

(m) $\bar{\kappa}_{xy}$ from unfiltered slopes for $t_S = 1$ mm plate test.

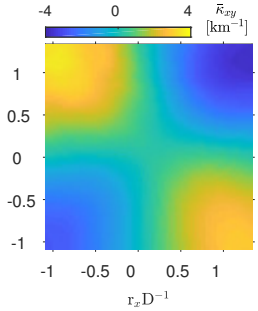

(n) $\bar{\kappa}_{xy}$ from filtered slopes for $t_S = 1$ mm plate test, $\sigma_\alpha = 3$.

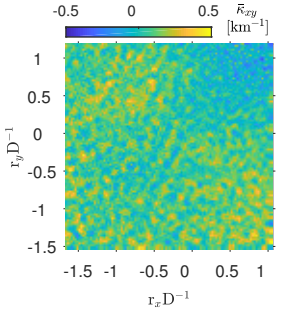

(o) $\bar{\kappa}_{xy}$ from unfiltered slopes for $t_S = 3$ mm plate test.

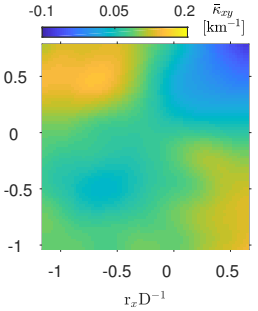

(p) $\bar{\kappa}_{xy}$ from filtered slopes for $t_S = 3$ mm plate test, $\sigma_\alpha = 6$.

Figure 5: Measured mean slope and curvature maps.

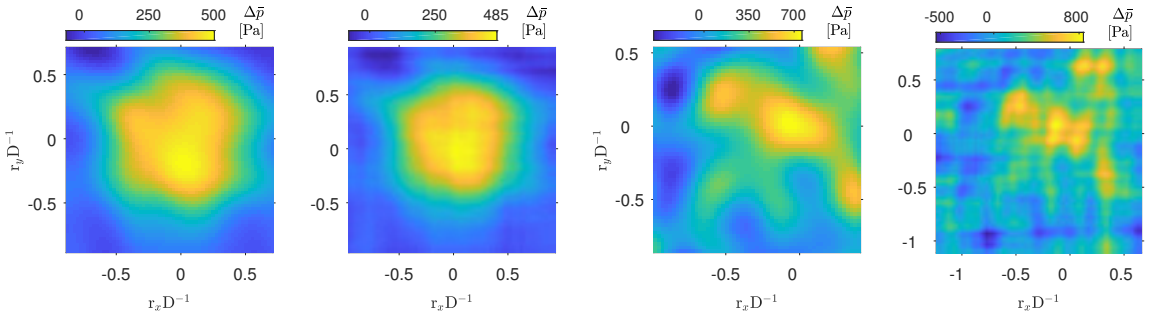

(a) $\Delta\bar{p}$ for 1 mm plate test, $\sigma_\alpha = 3$, PRW = 28.

(b) $\Delta\bar{p}$ for 1 mm plate test, $\sigma_\alpha = 0$, PRW = 34.

(c) $\Delta\bar{p}$ for 3 mm plate test, $\sigma_\alpha = 6$, PRW = 18.

(d) $\Delta\bar{p}$ for 3 mm plate test, $\sigma_\alpha = 0$, PRW = 34.

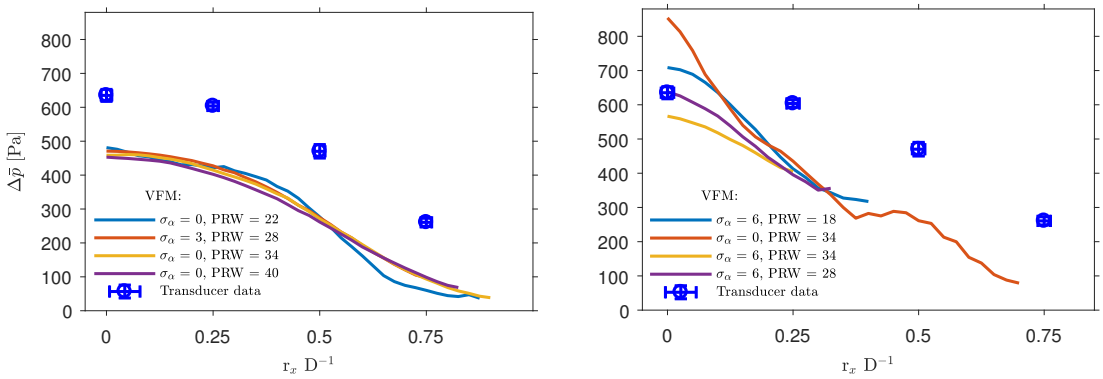

(e) Comparison between transducer measurements and VFM pressure reconstructions for 1 mm plate test.

(f) Comparison between transducer measurements and VFM pressure reconstructions for 3 mm plate test.

Figure 6: Comparison of VFM pressure reconstruction with pressure transducer data.

amplifies the impact of noise, filtering the slope maps yields much smoother curvature maps. The downside is a possible loss of signal amplitude and of data points along the edges (see section 3.5).

Fig. 6a-6d show pressure reconstructions using different PRW sizes. Pressure is given in terms of difference to atmospheric pressure, Δp. Here, one data point corresponds to a physical distance of 0.5 mm, such that a PRW of 28 points corresponds to a window side length of 14 mm or 0.7 rD^{-1}. The large number of data points is a result of oversampling by shifting the PRW over the investigated area by one point per iteration. The expected Gaussian shape of the distribution is found to be well reconstructed for filtered data and sufficiently large PRW, here above ca. 22 data points, for the 1 mm plate. Reconstructions from 3 mm plate tests are less symmetric. The position of the stagnation point, which was approximately determined during setup, is visible for all shown parameter combinations, but the shape of the distribution shows a recurring pattern which stems from the systematic error already observed in curvature maps. For both tests, some reconstructions show areas of negative differential pressure, which is unexpected for the mean distributions in this flow. This is likely to be a consequence of random noise, as similar patterns were observed in simulated experiments for noisy model data (see section 5.3 below). For comparisons with the transducer measurements, pressure reconstructions were averaged circumferentially for each corresponding radial distance from the stagnation point. Fig. 6e and 6f show the results. The vertical error bars on transducer

data represent both the systematic errors of the equipment as well as the random error of the mean pressure value. The horizontal error bars indicate the uncertainty in placing the transducers relative to the jet. Results from the 1 mm plate measurements appear to show a systematic underestimation of the pressure amplitude at all points. Possible sources for this error are discussed in detail in section 7 below. However, the shape of the distribution is captured reasonably well. The 3 mm plate results show a good reconstruction of the peak amplitude, but the shape of the pressure distribution deviates due to the influence of random noise patterns. The results clearly show that the effects of the size of the PRW and the Gaussian smoothing kernel σ_α on the reconstruction outcome are significant. Therefore, the influence of the reconstruction parameters is investigated numerically in the following section.

5 Simulated Experiments

Comparisons of the VFM pressure reconstruction with the pressure transducer data shows that there are discrepancies between the results. Furthermore, it is unclear what parts of the reconstructed pressure amplitude stems from signal, random noise or systematic error. Processing experimental data with noise can produce pressure distributions that are indistinguishable from the signal of interest. It is also important to note that the complex measurement chain from images to pressure does not allow for analytical expressions to be obtained and only numerical simulations can shed light on the problem.
Numerical studies allow addressing this problem and estimating the effects of random and systematic error (Grédiac et al., 2016). As a first step, a finite element model of the investigated thin plate problem is created. By applying a model load, the local displacements and slopes that result from the bending experiment can be simulated. For the next step, the grid image recorded with the camera is modelled numerically. The simulated displacements are used to calculate the deformations of the model grid image. Experimentally observed grey level noise is added to these grids. The simulated grids serve as input for a study of the influence of processing parameters on the pressure reconstruction. Comparisons with the model load allow an assessment of the uncertainties of the processing technique in the presence of random noise. In the last subsection, a finite element correction procedure is introduced to compensate for the reconstruction error.

5.1 Finite Element Model

Numerical data of slope maps from a thin plate bending under a given load distribution was calculated using a finite element simulation. This was conducted using the software ANSYS APDLv181. SHELL181 elements were chosen as they are well suited for modelling the investigated thin plate problem (Barbero, 2013). Both experimental test plates were simulated as homogeneous with the parameters detailed in table 1. All degrees of freedom, in case of SHELL181 3 for translation and 3 for rotation, were fixed along the edges. For both plates a square mesh was used with 1440 elements for the 1 mm thick plate and 2280 elements

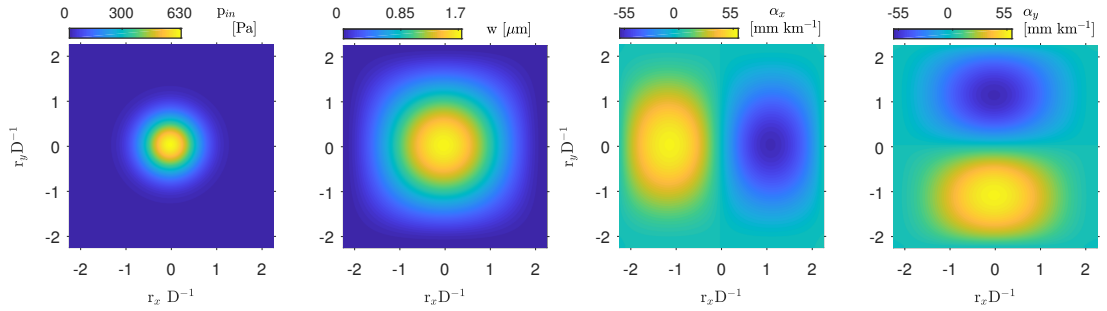

(a) Input load distribution. (b) Modelled deflections. (c) Modelled slopes α_x. (d) Modelled slopes α_y.

Figure 7: ANSYS model in- and output for 1 mm plate model.

for the 3 mm thick plate. This allowed obtaining 1024 points in a window corresponding to 64 mm, which corresponds to the experimental number of camera pixels and field of view. Fig. 7a shows the Gaussian pressure distribution used as input, with an amplitude of 630 Pa and $\sigma_{\text{load}} = 9$ mm, based on the results of the pressure transducer measurements. Fig. 7b shows the resulting deflections, fig. 7c and 7d the model slopes for the 1 mm plate case.

5.2 Systematic Error

The simulated slopes can be used as input for the VFM pressure reconstruction the same way as those obtained experimentally. This allows an assessment of the systematic error of the processing technique independent from experimental errors. A metric for estimating the error of a reconstruction was defined taking into account the difference between reconstructed and input pressure amplitude in terms of the local input amplitude at each point:

$$\epsilon = \frac{1}{N}\sum_{i=1}^{N}\left|\sqrt{(\mathrm{p}_{rec,i} - \mathrm{p}_{in,i})^2}/\mathrm{p}_{in,i}\right| \tag{6}$$

$p_{\text{rec, i}}$ is the reconstructed and $p_{\text{in, i}}$ the input pressure at each point i with a total number of points N. Pressure values below 1 Pa were omitted for this metric. Fig. 8a shows the results for the accuracy estimate for pressure reconstructions from noise free slope data for different PRW. The results are oversampled as in the experimental case by shifting the PRW by one point per iteration. A minimum exists at PRW $=$ 22 with $\epsilon = 0.12$, which indicates an average accuracy of ca. 88% of the local amplitude. The corresponding pressure reconstruction map is shown in fig. 8b. It should be noted that the local pressure amplitudes are underestimated for all investigated cases. For increasing PRW sizes, the peak amplitude is underestimated because the virtual fields act as a weighted average over the entire window. Small PRWs were expected to yield best results in a noise free environment since they average over fewer data points. This is not confirmed here. Different finite element mesh sizes were tested to rule out model convergence issues. The low accuracy obtained for small windows is probably due to a lack of heterogeneity of (real) curvature in small windows. If curvatures are constant, they can be taken out of the integral in eq. 4. Because the virtual curvatures average out to zero over

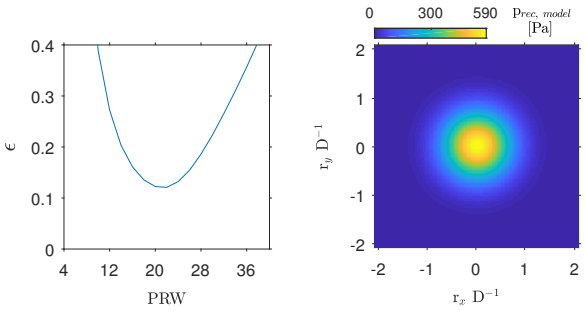

(a) Uncertainty estimate for varying PRW size.

(b) Example pressure reconstruction from simulated slopes using PRW = 22.

Figure 8: Systematic error estimate for VFM.

one window, the integral then yields zero. For small windows, this situation is approached, likely leading to wrong pressure values. Choosing heterogeneous virtual curvature fields could be used to address this issue in future studies. One approach could be to define more nodes on each virtual field and a non-zero virtual deflections on a node other than the center one to increase heterogeneity. Another way could be to employ higher order approaches for pressure calculation within one window, which is expected to yield higher accuracy for large PRW.

5.3 Grid Deformation Study

Artificial grid deformation allows for a more comprehensive assessment of error propagation by including the effects of camera resolution and noise. Following the approach described in Rossi and Pierron, 2012, a periodic function with a wavelength corresponding to the experimental grid pitch was used in x- and y-direction to generate the artificial grid.

$$\begin{aligned} I(x,y) \;=\; & I_{min} + \frac{I_{min} - I_{max}}{2} + \frac{I_{max}}{4} \\ & \cdot \left(\cos\left(\frac{2\pi x}{p_G}\right) + \cos\left(\frac{2\pi y}{p_G}\right) \right. \\ & \left. - \left| \cos\left(\frac{2\pi x}{p_G}\right) - \cos\left(\frac{2\pi y}{p_G}\right) \right| \right) \end{aligned} \tag{7}$$

Here, $I_{\min}$ and $I_{\max}$ are the minimum and maximum intensity values of the experimental grid images. The signal amplitude values were discretised to match the camera's dynamic range. All simulated image parameters were set to replicate the experimental conditions as described in table 1. This spatial grid signal was oversampled by a factor of 10 and spatially integrated to simulate the signal recording process of the camera, as detailed in Rossi and Pierron, 2012. To further assess the actual experiment, random noise was added to the artificial grid images based on the grey level noise measured during experiments, here 0.95% and 0.61% of the used dynamic range in case of the 1 mm and 3 mm plate tests respectively. It varies because the

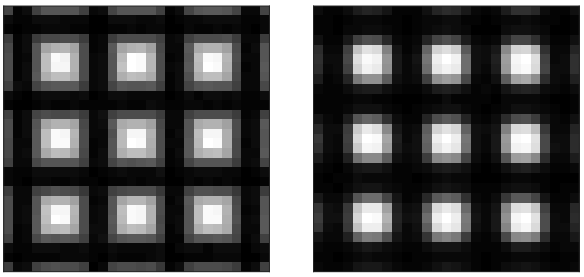

(a) Artificial grid after integration and with added noise.

(b) Experimental grid.

Figure 9: Example grid sections.

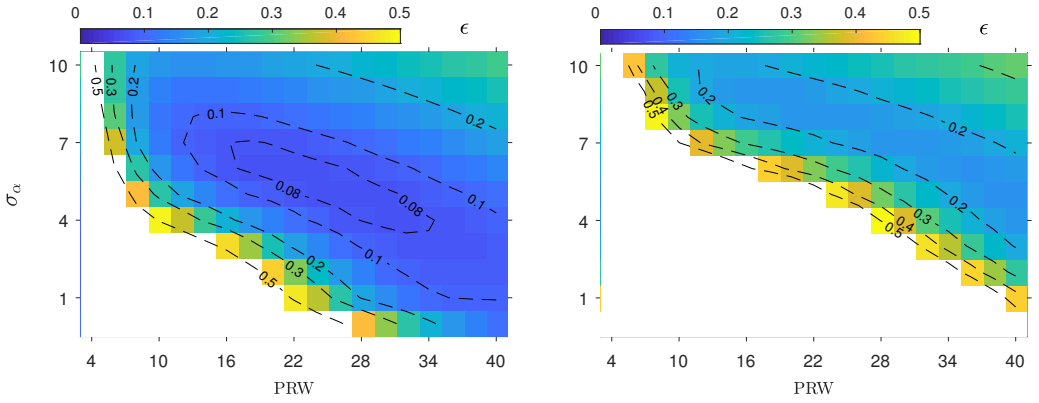

(a) Error estimates for varying slope filter kernel and PRW size for 1 mm plate test and with grey level noise 0.95 % of the dynamic range.

(b) Error estimates for varying slope filter kernel and PRW size for 3 mm plate test and with grey level noise 0.6 % of the dynamic range.

Figure 10: Pressure reconstruction accuracy analysis.

illumination varied between both experiments, such that the used dynamic range was different. The amount of random noise is reduced with the number of measurements over which the mean value is calculated. However, the reduction of noise is not described by $1/\sqrt{N}$ as would be expected. The same observation was made in Devivier, 2012. It was investigated by taking a series of images without applying a load to the specimen. It was found that the amount of noise in phase maps increases with the time that has passed between two images being taken. It is likely that this is a result of small movements or deformations of the sample, printed grid and camera due to vibrations and temperature changes during the measurement. This does not fully account for the observed effect however. As a consequence, the amount of random noise for averages over multiple measurements has to be determined experimentally. For 5400 measurements on the undeformed sample, it was found that the random noise in phase was reduced by a factor of ca. 2.5 compared to two measurements. The values are statistically well converged after 30 realisations of simulated noise.

The simulation neglects the effects of grid defects, lens imperfections, inhomogeneous illumination and imperfections of the specimen. However, it does account for any systematic errors associated with the number of pixels on the camera sensor and the random errors coming from grey level noise in the images. Fig. 9 shows a close-up view of simulated and experimental grid

images. Simulated slopes yield corresponding deformations of the artificial grid at every point using eqs. 1 and 3. The obtained artificial grids for deformed and undeformed configurations can now be used as input for the phase detection algorithm which was used for processing the experimental data.

Areas with negative pressure amplitude were observed in reconstructions from noisy model data, very similar to those observed experimentally. A lower limit for pressure resolution was determined by adding noise to two undeformed artificial grids and processing them. The standard deviation of pressure values obtained from this reconstruction can be interpreted as a metric for the lower detection limit of the pressure reconstruction for the corresponding parameter combination. Values below the obtained threshold are neglected in all reconstructions in the following.

Phases obtained from artificial, deformed grids were processed and the reconstructed and input pressure were compared using the metric introduced in eq. 6. This allows quantifying the systematic error of phase detection and VFM for all combinations of the relevant processing parameters. Oversampling in the phase detection algorithm, *i.e.* calculating more than one phase value per grid pitch, was found to improve the results, though at high computational cost. Particularly in combination with larger PRW and slope filter kernels, phase oversampled slope maps yield diminishing improvements in accuracy in terms of the overall cost. In the VFM pressure reconstruction, oversampling provided a significant improvement at acceptable cost. The slope filter kernel size σ_α also increases computational cost, but mitigates the effects of random noise efficiently. The influence of both the size of σ_α and PRW are investigated in the following as they yield the most significant improvements.

Figs. 10a and 10b show the findings for varying parameters σ_α and PRW for each plate. These allow selecting parameter combinations with highest precision in terms of amplitude over the entire field of view. Fig. 12-13 show example comparisons of pressure reconstructions for different ϵ. Fig. 12 shows experimental data with two different parameter combinations for both plates and fig. 13 below shows the corresponding results obtained using model data. For reference, fig. 11 shows on top the model input distribution sections in the respective field of view. As expected, reconstructions using larger smoothing kernels tend to yield lower peak amplitudes. However, the amplitudes in other areas are captured better, as noise induced peaks are filtered more efficiently. The fact that some numerical reconstructions do not represent Gaussian distributions well shows that noise effects are not averaged out entirely. For the low signal to noise ratio encountered in the 3 mm plate case, some reconstructions overestimate the peak pressure amplitude. This is a consequence of the differentiation of slope noise, which leads to large curvature and thus pressure values. Since this also leads to areas in which the pressure amplitude is underestimated, the effect averages out for sufficiently large slope smoothing kernel and PRW.

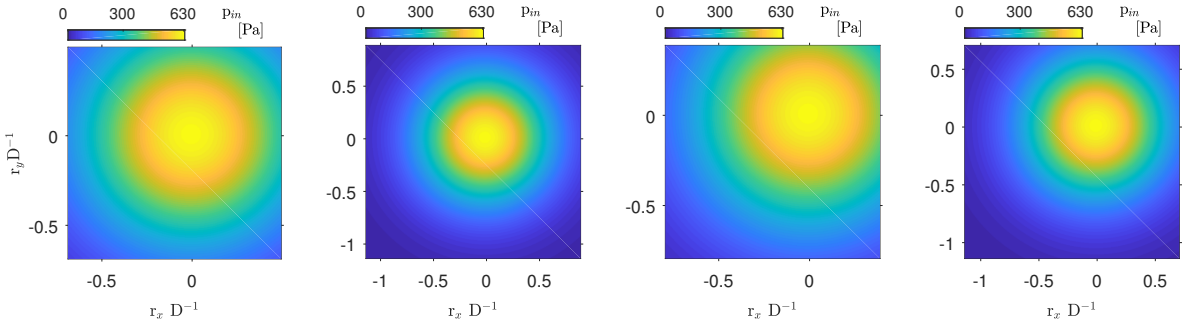

(a) Section corresponding to $\sigma_\alpha = 6$, PRW = 28 reconstruction.

(b) Section corresponding to $\sigma_\alpha = 0$, PRW = 22 reconstruction.

(c) Section corresponding to $\sigma_\alpha = 6$, PRW = 34 reconstruction.

(d) Section corresponding to $\sigma_\alpha = 2$, PRW = 28 reconstruction.

Figure 11: Model input pressure distribution sections for comparison with reconstruction results.

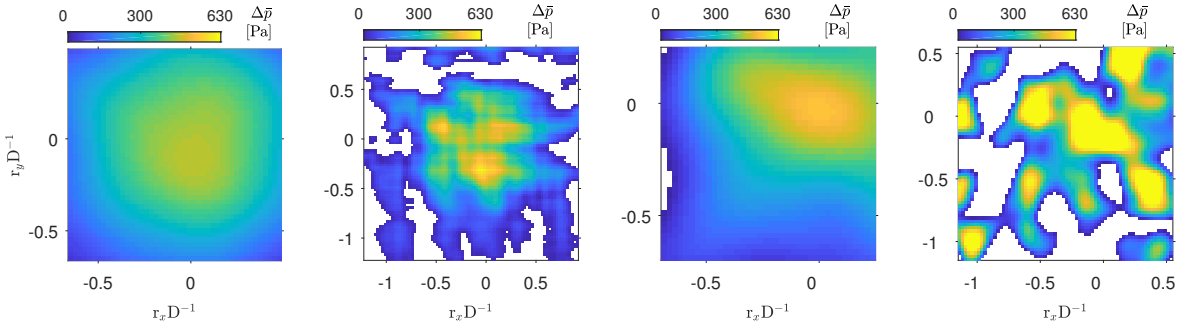

(a) Pressure reconstruction for 1 mm plate good accuracy estimate ($\sigma_\alpha = 6$, PRW = 28, $\epsilon = 0.08$).

(b) Pressure reconstruction for 1 mm plate for $\sigma_\alpha = 0$, PRW = 22, $\epsilon = 0.4$.

(c) Pressure reconstruction for 3 mm plate for good accuracy estimate ($\sigma_\alpha = 6$, PRW = 34, $\epsilon = 0.2$).

(d) Pressure reconstruction for 3 mm plate for poor accuracy estimate ($\sigma_\alpha = 2$, PRW = 28, $\epsilon > 0.5$).

Figure 12: Comparison of pressure reconstructions from experimental data for different parameter combinations.

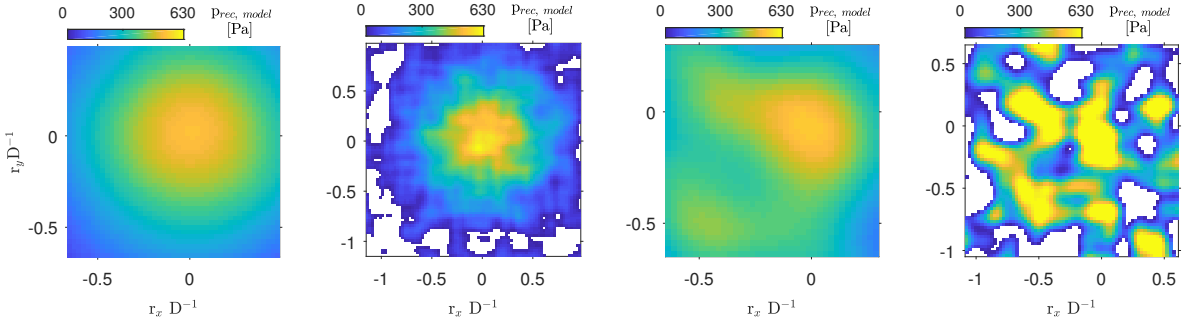

(a) Pressure reconstruction for 1 mm plate for good accuracy estimate ($\sigma_\alpha = 6$, PRW = 28, $\epsilon = 0.08$).

(b) Pressure reconstruction for 1 mm plate for poor accuracy estimate ($\sigma_\alpha = 0$, PRW = 22, $\epsilon = 0.4$).

(c) Pressure reconstruction for 3 mm plate for good accuracy estimate ($\sigma_\alpha = 6$, PRW = 34, $\epsilon = 0.2$).

(d) Pressure reconstruction for 3 mm plate for poor accuracy estimate ($\sigma_\alpha = 2$, PRW = 28, $\epsilon > 0.5$).

Figure 13: Comparison of pressure reconstructions from noisy model data for different parameter combinations.

6 Finite Element Correction

The systematic error caused by the reconstruction technique which was identified above shows an underestimation of the input pressure for noise free data. In the presence of noise, a similar observation is made for large enough signal to noise ratio as in the 1 mm plate case. This error source can be mitigated with a finite element correction procedure. For this approach, an initial reconstructed pressure distribution is used as input for the numerical model described above. In practice, this is the experimentally identified distribution from the VFM. Processing the resulting slope maps obtained using the finite element model (see section 5.1) yields the first iterated pressure distribution. The difference between this iteration and the original pressure reconstruction corresponds to the systematic error at every point of the pressure map. This difference is generally lower in amplitude than that between the original reconstruction and the real pressure distribution caused by systematic error, but it serves as a first estimation of that difference. Adding this difference to the original reconstruction yields an updated approximation of the real pressure distribution:

$$dp_{\mathrm{update,n}} = p_{\mathrm{rec}} + (p_{\mathrm{rec}} - p_{\mathrm{it,n}}) \tag{8}$$

This procedure can be repeated until $(p_{\mathrm{rec}} - p_{\mathrm{it,n}})$ falls below a chosen threshold. Fig. 14 shows how the input load is well recovered after only few iterations for modelled, noise free data. For the shown case, the second iteration result is already well converged and much closer to the input distribution, with an improvement from ca. 15% average error to below 6%. Similar results were found for the other investigated PRW sizes.

An application to experimental data is more challenging. Each iteration tends to amplify noise patterns in pressure maps from both random and systematic error sources. Reconstructions from smoothed slope maps mitigate this issue, but suffer from a reduced number of available data points. Note that for each iteration, the size of one smoothing window, *i.e.* 6 σ_α, plus half a PRW of data points is lost around the edges (see also section 3.5). Here, this can be mitigated by using reconstructions with small slope smoothing kernels and by calculating circumferential averages from the stagnation point outwards, thus averaging out some of the random noise. These are then extrapolated to 2D distributions to obtain a suitable input for

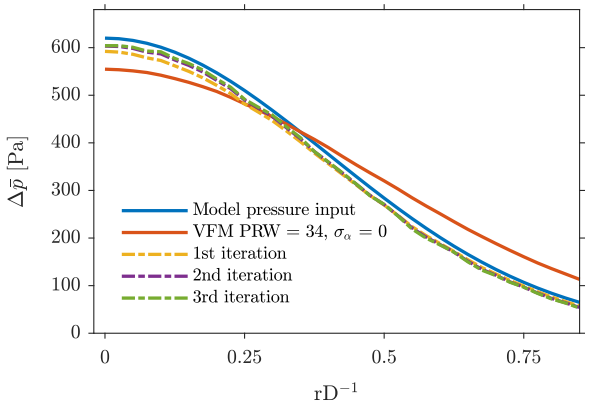

Figure 14: FE corrected results for noise free model data.

the finite element updating procedure. The entire process is applied to both numerical and experimental data, allowing for a comparison of the results and thus further assessment of the influence of systematic experimental errors.

To select the correct reconstruction parameters for this approach, the accuracy assessment was repeated using circumferential averages instead of the entire field of view. The results vary, because low amplitude pressures are now averaged over a larger number of data points. Further, part of the field of view with low pressure amplitude is not taken into account as it is rectangular. The result is shown in fig. 15. Fig. 16 shows the results for iterations of experimental data and noisy model data. A 10% error bar corresponding to the estimated uncertainty resulting from the material's Young's modulus is shown for the iterations on experimental data at the positions of transducers for comparison. Fig. 16a shows that for $\sigma_\alpha = 3$ and PRW = 28 the peak amplitude from transducer measurements is approximated to about 10% after 2 iterations of the experimental data. Since slope smoothing leads to a significant loss in data points, no further iterations are possible for this case. The corresponding numerical case, see fig. 16b, shows a close approximation of the input load.

For experimental data and $\sigma_\alpha = 0$ and PRW = 34, see fig. 16c, the influence of noise patterns becomes visible. These patterns are amplified by the correction procedure. Numerical data show a very good approximation of the input load, whereas experimental VFM data deviate from transducer data by ca. 10% after correction.

For $\sigma_\alpha = 0$ and PRW = 22, see fig. 16e, noise effects in experimental data are significant. Therefore, regularisation is necessary before iterating the results. Here, a fourth order polynomial was fitted to the averaged results. The iterated corrections once again approximate the transducer data to within ca. 10% of the peak amplitude. Fig. 16f shows that for noisy model data an acceptable original estimation of the input amplitude is obtained. The corresponding corrected pressure distribution overestimates the peak and low range pressure amplitudes of the input distribution by ca. 5% of the peak amplitude. The in comparison to numerical data more pronounced noise patterns in experimental data (see also figs. 11b and 12b) were found to stem not only from random but also from systematic error sources (see section 4). They

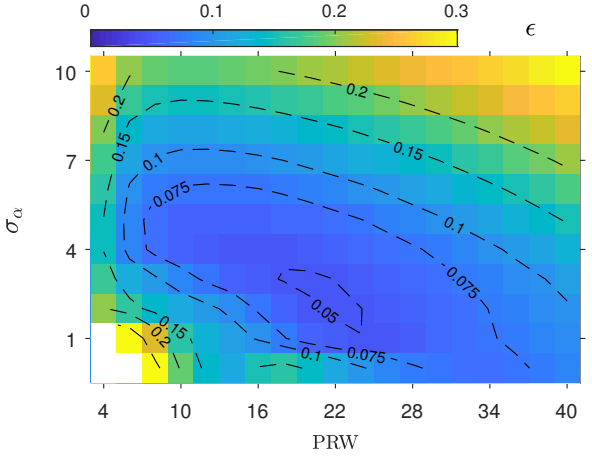

Figure 15: Error estimates for circumferentially averaged pressure reconstructions for varying slope filter kernel and PRW size for 1 mm plate test and with grey level noise 0.95% of the dynamic range.

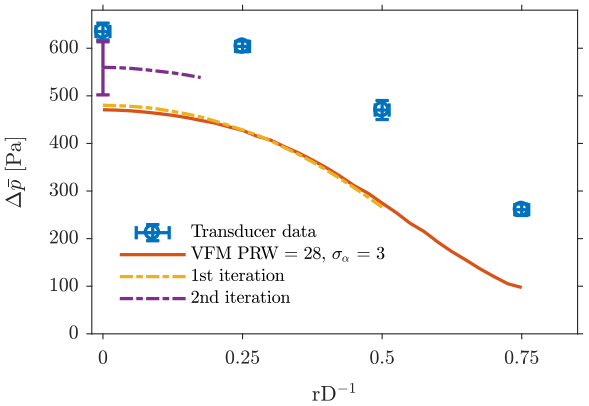

(a) Iteration of experimental data, $\sigma_\alpha = 3$ and PRW = 28.

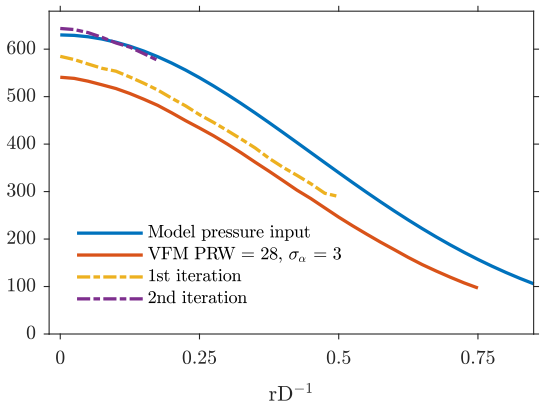

(b) Iteration of model data with noise, $\sigma_\alpha = 3$ and PRW = 28.

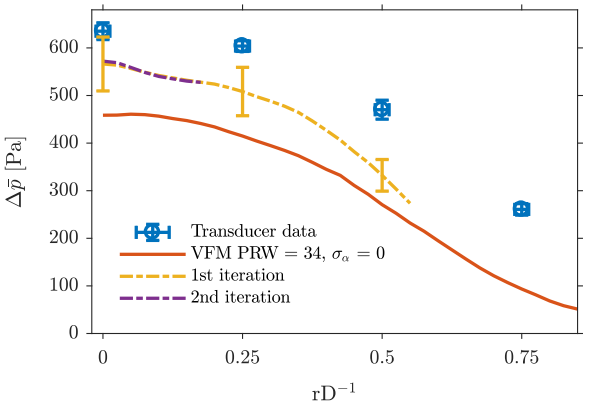

(c) Iteration of experimental data, $\sigma_\alpha = 0$ and PRW = 34.

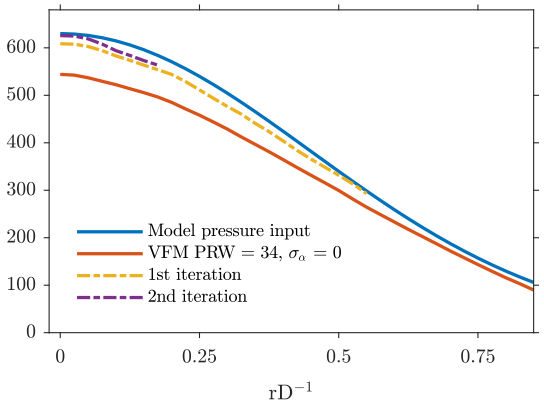

(d) Iteration of model data with noise, $\sigma_\alpha = 0$ and PRW = 34.

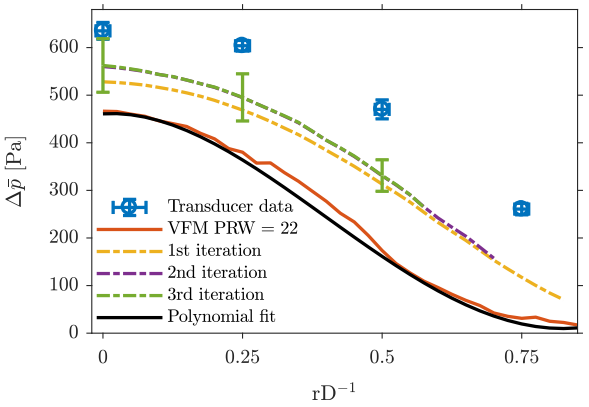

(e) Iteration of experimental data, $\sigma_\alpha = 0$ and PRW = 22.

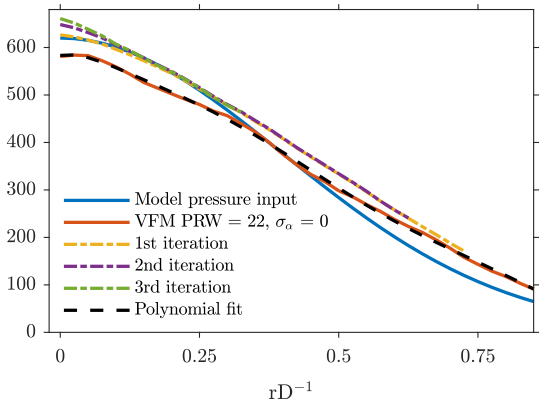

(f) Iteration of model data with noise, $\sigma_\alpha = 0$ and PRW = 22.

Figure 16: Finite element updating results. Error bars on VFM represent the estimated uncertainty resulting from the material's Young's modulus. Error bars on transducer data represent both the systematic errors of the equipment as well as the random error of the mean pressure value.

may also be the reason for the large difference between experimental and numerical data in the initial reconstruction amplitude, here for PRW = 22 ca. 15%.
All iterations appear reasonably well converged after the second iteration. Notably, the difference in peak amplitude is reduced to around 10% or better for all investigated cases. The outcome depends on the prevalence of noise patterns, which is more pronounced for small PRWs and small or no slope filters. However, larger reconstruction windows and filter kernels do not allow for many iterations since the loss of data points around the edges increases with PRW size.

7 Error Sources

The presented comparisons between real and simulated experiments have shown the influence of random noise and processing parameters on the pressure reconstruction. Experimental random noise patterns were qualitatively reproduced with the modelled data for all investigated cases. The presence of random noise was found to have a significant impact on the reconstruction results. A systematic error in the processing method was found to result in an underestimation of pressure amplitudes for noise-free model data. This error varies with the processing parameters. Further, a systematic experimental error appears between reconstructed and transducer-measured pressures. It was found that reconstructions from model data were consistently closer to the input data than the experimental reconstructions were to pressure transducer data, which are an established measurement technique. Based on the comparisons of numerical and experimental data shown in section 6, this error resulted in an additional underestimation of approximately 10% of the peak amplitude.
There are several possible sources for this experimental error. Miscalibration, *i.e.* non-integer numbers of pixels per pitch in the recorded grid, can lead to errors in the detected phases. It can be caused by misalignments between camera sensor and printed grid. Even with careful arrangement, small deformations of the specimen surface can cause misalignment issues. Note that these can also occur due to the deformations of the specimen under the investigated (dynamic) load. Misalignment can particularly result in fringes which can lead to the unexpected patterns observed in curvature maps in section 4. Irregularities and damages in the printed grid can also result in errors during phase detection. The influence of these error sources on pressure amplitude is however difficult to quantify. Another possible error source is wrong material parameter values, particularly the Young's modulus. The data information provided by the manufacturer gives a value of $E = 74$ GPa, but values between 47 GPa - 83 GPa are found for glass in the literature (*e.g.* Ashby, 2011, table 15.3). 3- and 4-point bending tests on the specimen yielded values between 69 GPa and 83 GPa before the sample broke. Note that the relationship between Young's modulus and plate stiffness matrix components, and thus pressure amplitudes (see eq. 4), is linear, *i.e.* a 10% higher value of E would increase all pressure amplitudes by 10%, compensating for the discrepancy observed here. Deviations of the Poisson's ratio from the manufacturer information would have a similar impact. Since

the plate stiffness matrix components are proportional to the third power of the plate thickness, errors in its determination have a higher impact than is the case for the other material parameters. Several measurements did however confirm the thickness values provided by the manufacturer. Assuming an error of 0.1% in the plate thickness as worst case estimate, one obtains a 3% error in the pressure amplitude.
Also, the assumptions of negligibility of rigid body movement and out of plane displacement need to be considered. LDV measurements on the frame holding the specimen showed no results above noise level, which corresponds to 0.1 μm here. Rigid body movement can therefore be ruled out as a relevant error source. The effect of out of plane displacements can be estimated based on the expected deflections, w, and the distance between grid and specimen. A detailed derivation of this relationship is given in Devivier, 2012, chapter 2.1.2. The resulting error on curvature maps is $\kappa_{oop} = \frac{w}{h_S}$. The finite element simulations from section 5 showed that the deflections for the 1 mm plate test can be expected to be smaller than 2 μm, which would correspond to an error in curvature of $\kappa_{oop} = 2\ 10^{-3}\ \mathrm{km}^{-1}$. This worst-case estimate corresponds to an error of only 0.05% of the peak curvature signal amplitude. Finally, the thin plate assumptions were tested using the finite element simulation introduced in section 5.1. The chosen SHELL181 elements are suited for linear as well as for large rotation and large strain nonlinear applications. This means that simulated slopes and curvatures could deviate from those calculated from the deflections using thin plate assumptions (see *e.g.* (Timoshenko and Woinowsky-Krieger, 1959)), if the latter were in fact not applicable. The simulated and the calculated slopes and curvatures were compared to verify the validity of the assumptions. For the 1 mm thick plate it was found that the difference was five orders of magnitude below the signal amplitude in case of slopes and thee orders of magnitude in case of curvatures.

8 Limitations and Future Work

This study shows that it is possible to obtain full-field pressure measurements of the order of few $\mathcal{O}(100)$ Pa amplitude with the described setup and processing technique. A number of experimental limitations were encountered from applying this method to low amplitude loads. Small grid pitches are required to provide the required slope resolution. These require a very smooth and plane specular reflective specimen surface. Further decreasing the grid pitch would require more camera pixels to investigate the same region of interest, as the phase detection algorithm requires a minimum amount of pixels per pitch. Alternatively, the distance between grid and sample could be increased, which would require a different lens to achieve the same magnification. Furthermore, the specimen has to be stiff enough to provide a plane surface when mounted to avoid bias errors, but is required to deform sufficiently to provide enough signal for the measurement technique. The issue of misalignment could be addressed by using high precision components like micro stages with stepper motors to arrange camera, sample and grid.
Another approach is the use of infrared instead of visible light for deflectometry, with heated grids as spatial carrier Toniuc and Pierron, 2018. Since infrared light has a longer wavelength

than visible light, it allows achieving specular reflection on specimens that do not have mirror-like but reasonably smooth surfaces with up to about 1.5 μm of RMS roughness, like perspex and metal plates. However, available cameras are limited in terms of spatial and temporal resolutions. Further issues are the lack of an aperture ring and that the lenses required to achieve comparable magnification are more expensive. An extension of the application of deflectometry to moderately curved surfaces was presented recently Surrel and Pierron, 2019. This approach requires a calibration for deformation measurement. Furthermore, the required depth of field is a restricting factor for the use of small grid pitches. A successful combination of deflectometry measurements on curved surfaces with VFM pressure reconstruction would be of great value, as it would allow direct measurements on practically relevant surfaces like *e.g.* aerofoils, fuselages and ship hulls.
In future studies, the turbulent fluctuations that occur in many practical flows like the impinging jet used here will be investigated. Typically they have pressure amplitudes of the order of few $\mathcal{O}(10)$ Pa and below. These could not be resolved in this study. Preliminary analyses of time resolved data taken at 4 kHz show that this is in parts due to a systematic experimental error, which results in spatial distributions fluctuating at low frequency and relatively high amplitude. The application of Fourier analyses and Dynamic Mode Decomposition (DMD) are currently being investigated with promising first results. Dynamic full-field pressure reconstruction of turbulent fluctuations are a continuous challenge for current experimental measurement techniques due to their low amplitudes and small spatial scales, rendering the further development of the technique presented here highly relevant.
Another currently investigated improvement involves employing the aforementioned higher resolution cameras and smaller grid pitches to increase slope sensitivity and spatial resolution. This approach does not allow for time resolved measurements due to frame rate limitations of high resolution cameras, but first tests using phase averaging for periodic flows generated by synthetic jets are very promising.
Finally, the selection of virtual fields is an important factor in improving the quality of reconstructions. Particularly higher order approaches in pressure identification are likely to reduce the systematic error.

9 Conclusion

This work presents a method for surface pressure reconstructions from slope measurements using a deflectometry setup combined with the VFM. Experimental and numerical methods have been introduced to assess the pressure reconstructions.

- Low amplitude pressure distributions were reconstructed from full-field slope measurements using the material constitutive mechanical parameters.
- Experimental results are presented and compared for several reconstruction parameters and for two different specimen.

- VFM pressure reconstructions were compared to pressure transducer measurements.
- Simulated experiments employing a finite element model and artificial grid deformation were used to assess the uncertainty of the method.
- The numerical results were used to select optimal reconstruction parameters, taking into account experimentally observed noise.
- A finite element correction procedure was proposed to mitigate the systematic error of VFM pressure reconstructions.
- Error sources were discussed based on the findings of both the experimental and the simulated results.

A systematic processing error leading to an underestimation of the pressure amplitude was identified. Since the shape of the distribution is still reconstructed well, it is possible to compensate for this error using the proposed numerical approaches as long as noise patterns are not too pronounced. A systematic experimental error was found to result in an additional underestimation of the pressure amplitude by ca. 10% more than simulated reconstructions. Yet, the results stand out in terms of the low pressure amplitudes and the large number of data points obtained.

10 Data Provision

All relevant data produced in this study will be made available upon publication of this manuscript.

Acknowledgements This work was funded by the Engineering and Physical Sciences Research Council (EPSRC). F. Pierron acknowledges support from the Wolfson Foundation through a Royal Society Wolfson Research Merit Award (2012-2017). Advice and assistance given by Cédric Devivier, Yves Surrel, Manuel Aguiar Ferreira and Lloyd Fletcher has been a great help in conducting simulations and planning of experiments. The comments provided by Manuel Aguiar Ferreira and Lloyd Fletcher have greatly improved this paper.

Paper 2

Reconstruction of surface pressure fluctuations using deflectometry and the Virtual Fields Method

R. Kaufmann, F. Pierron, B. Ganapathisubramani

Faculty of Engineering and Physical Sciences, University of Southampton, Southampton SO17 1BJ, UK

Intended for submission to the Journal Experiments in Fluids

Abstract This study presents an approach for obtaining full-field dynamic surface pressure reconstructions with low differential amplitudes. The method is demonstrated in a setup where an air jet is impinging on a flat plate. Deformations of the flat plate under dynamic loading of the impinging jet were obtained using a deflectometry setup that allows measurement of surface slopes with high accuracy and sensitivity. The measured slope information was then used as input for the Virtual Fields Method (VFM) to reconstruct pressure. Pressure fluctuations with amplitudes of down to $\mathcal{O}(1)$ Pa were extracted from time-resolved deflectometry data using temporal band-pass filters. Pressure transducer measurements allowed comparisons of the results with an established measurement technique. Dynamic Mode Decomposition (DMD) was used to identify relevant spatial information that correspond to specific frequencies. These dynamically important spatio-temporal events can for the first time be observed despite their low differential amplitudes. Finally, the limitations of the proposed pressure determination method and strategies for future improvements are discussed.

1 Introduction

The measurement of dynamic surface pressure distributions is crucial for a range of applications in fluid dynamics, material design and testing, as well as for the investigation of impinging jets for heat and mass transfer. Time resolved measurements that provide a large number of data points for low-range differential pressures are challenging for current techniques. Larger pressure amplitudes can be measured optically in full-field using pressure sensitive paints (PSP), *e.g.* Tropea et al., 2007, chapter 4.4. Pressure transducers are commonly used for the measurement of small differential pressure amplitudes but they allow only point-wise measurements. Fitting these transducers requires drill-holes in the investigated specimen, changing the material response. Particle Image Velocimetry (PIV) allows full-field pressure reconstructions, *e.g.* de Kat and van Oudheusden, 2012; Jaw et al., 2009, but is limited to the flow field. Near the surface, the technique is restricted by reflections and the finite size of the reconstruction window.

Alternatively, surface deformation measurements can be used to calculate the pressure acting

on a specimen by solving the mechanical equilibrium equations. For thin plates in pure bending, the local equilibrium equation can be obtained using the Love-Kirchhoff theory, which involves fourth order derivatives of the surface deflections (Timoshenko and Woinowsky-Krieger, 1959). Such high order derivatives lead to significant noise amplification and therefore require regularisation. In Pezerat and Guyader, 2000 local deflections were measured with a Laser Doppler Vibrometer (LDV). Wave number filters were then applied prior to solving the equilibrium equation locally, which allowed an identification of external vibration sources. The acoustic component of a turbulent boundary layer flow was identified with a similar approach in Lecoq et al., 2014. Generally, the spatial as well as the signal resolution that can be achieved vary with the chosen regularisation technique and parameters.

The Virtual Fields Method (VFM) is an alternative identification method that is based on the principle of virtual work. For the purpose of pressure identification, the VFM requires full-field kinematic data, the mechanical constitutive material parameters of the specimen, and suitable virtual fields. The latter need to be selected with respect to the theoretical and practical requirements of the investigated problem, such as boundary conditions and continuity. In the case of thin plates in pure bending, the principle of virtual work yields an equation that only involves second order deflection derivatives. Interestingly, the virtual fields can be selected to provide different levels of regularization adapted to a given signal-to-noise ratio. The VFM is described in detail with a range of applications in Pierron and Grédiac, 2012. It was used in combination with scanning Laser Doppler Vibrometer (LDV) measurements for investigating acoustic loads on plates. This allowed reconstructing spatially-averaged sound pressure levels in Robin and Berry, 2018 and transverse loads and vibrations in Berry et al., 2014, as well as random external wall pressure excitations in Berry and Robin, 2016. In an investigation of the sound transmission of plates, comparisons of spatially averaged pressure auto-spectra with microphone array measurements showed good agreement except at structural resonance frequencies in Robin and Berry, 2018. A limitation of these studies was that full-field data could not be obtained simultaneously with LDV measurements. This can be addressed by using alternative measurement techniques. Deflectometry is an optical full-field technique for the measurement of surface slopes (Surrel et al., 1999), which can be combined with high speed cameras to investigate dynamic events. It can achieve very high sensitivities. In Devivier et al., 2016, ultrasonic lamb waves were imaged using deflectometry, and in Giraudeau et al., 2010 it was used to identify stiffness and damping on vibrating plates. Since deflectometry measurements yield surface slopes, the required order of derivatives of experimental data in the VFM is reduced to one. A combination of deflectometry and the VFM was employed in O'Donoughue et al., 2017 to reconstruct dynamics of mechanical point loads on an aluminium plate of several $\mathcal{O}(1)$ N. Spatially averaged random excitations were identified with this method in O'Donoughue et al., 2019. In Kaufmann et al., 2019a it was used to measure mean pressure distributions of an impinging air jet with differential pressure amplitudes of several $\mathcal{O}(100)$ Pa. The study also proposes a methodology to assess the accuracy of pressure reconstructions and to select optimal reconstruction parameters. However, in several aerodynamic and hydrodynamic applications, it is important to obtain surface pressure fluctuations (both broadband as well as at certain frequencies). In the present study, the

work of Kaufmann et al., 2019a is extended to measure the spatio-temporal evolution of low differential pressure events generated by the flow on a surface. The method is demonstrated in a canonical flow problem: a jet impinging on a flat surface. This work is specifically concerned with reconstructing the pressure footprint of large-scale vortices impinging on the plate. These pressure fluctuations will have very low differential pressure compared to the mean flow. This specific flow problem is chosen to highlight the pros and cons of the proposed surface pressure determination technique.

2 Theory

2.1 Deflectometry

Deflectometry is an optical technique that allows full-field slope measurements on specular reflective surfaces using a periodic spatial signal Surrel et al., 1999. A schematic of the setup is shown in fig. 1. $\mathrm{p_G}$ is the pitch of the spatial signal, here a cross-hatched grid, and $\mathrm{h_G}$ the distance between grid and specimen surface. The camera is placed next to the grid, such that a pixel directed at point M on the specimen surface records the reflected grid at point P. Applying a load deforms the surface locally, resulting in a change in surface slope, $\mathrm{d}\alpha$, such that the same pixel will now record the reflected point P′. Rigid body movements and out-of-plane deflections are neglected here, as the specimen bending stiffness is sufficiently large and the investigated loads small.

Phase maps are extracted from grid images using a spatial phase-stepping algorithm featuring a windowed discrete Fourier transform algorithm with triangular weighting and using a detection kernel size of two periods Surrel, 2000; Badulescu et al., 2009. This algorithm suppresses some harmonics resulting from the use of a non-sinusoidal signal and mitigates the effects of miscalibration. The displacement, $\boldsymbol{u}$, between P and P′ is calculated iteratively from the obtained phase maps Grédiac et al., 2016, section 4.2:

$$\boldsymbol{u}_{n+1}(\boldsymbol{x}) = -\frac{p_G}{2\pi}(\phi_{\mathrm{def}}(\boldsymbol{x}+\boldsymbol{u}_n(\boldsymbol{x})) - \phi_{\mathrm{ref}}(\boldsymbol{x}))\ , \tag{1}$$

where the subscripts def and ref refer to a deformed and a reference configuration, as the phase difference between a loaded and unloaded configuration is of interest.

For sufficiently small $\mathrm{d}\alpha$, $h_\mathrm{G} \gg \boldsymbol{u}$, small angle θ and assuming that the camera records images in normal incidence, geometric considerations yield a simplified, linear relationship between the change in surface slope $\mathrm{d}\alpha$ and $\boldsymbol{u}$ (*e.g.* Ritter, 1982):

$$d\alpha_x = \frac{u_x}{2h_G}, \quad d\alpha_y = \frac{u_y}{2h_G}\ . \tag{2}$$

If this hypothesis is not valid, then full calibration needs to be performed, which is more complex Balzer and Werling, 2010; Surrel and Pierron, 2019. The printed grid pitch p_G drives the spatial resolution. The slope resolution depends on measurement noise as well as p_G and h_G.

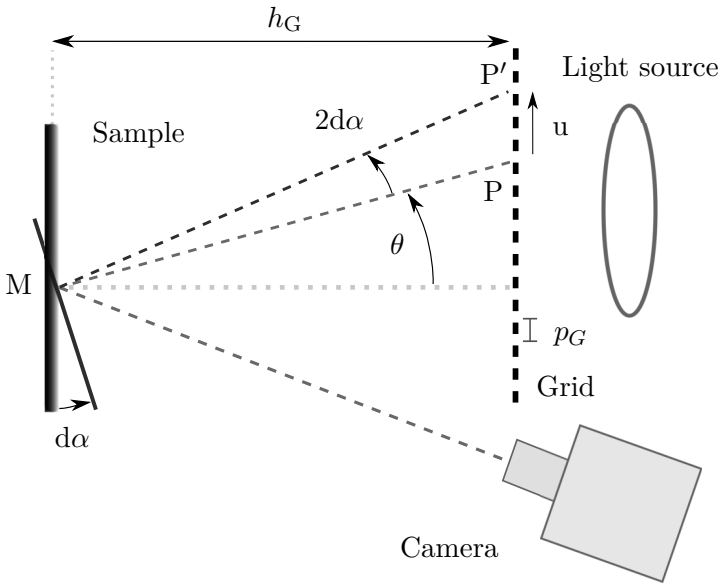

Figure 1: Top view of deflectometry setup and working principle (redrawn from (Kaufmann et al., 2019a)).

2.2 Pressure Reconstruction

Assuming that the plate material is linear elastic, isotropic and homogeneous, the principle of virtual work is expressed by:

$$\begin{aligned}\int_S p\ w^* dS \ &= \ D_{xx} \int_S \left(\kappa_{xx}\kappa^*_{xx} + \kappa_{yy}\kappa^*_{yy} + 2\ \kappa_{xy}\kappa^*_{xy}\right) dS \\ &+ \ D_{xy} \int_S \left(\kappa_{xx}\kappa^*_{yy} + \kappa_{yy}\kappa^*_{xx} - 2\ \kappa_{xy}\kappa^*_{xy}\right) dS + \ \rho\ t_S \int_S a\ w^* dS \quad ,\end{aligned} \tag{3}$$

where S denotes the surface area, p the investigated pressure, D_{xx} and D_{xy} the plate bending stiffness matrix components, κ the curvatures, ρ the plate material density, t_S the plate thickness, $\boldsymbol{a}$ the acceleration, w^* the virtual deflections and κ^* the virtual curvatures. In the present study D_{xx}, D_{xy}, ρ and t_S were known from the plate manufacturer. κ and a were obtained from deflectometry measurements. The virtual fields w^* and κ^* have to be chosen with respect to theoretical as well as practical restrictions of the problem such as continuity, boundary conditions and sensitivity to noise.

2.3 Virtual Fields

In this study, 4-node Hermite 16 element shape functions were used to define virtual fields over subdomains of the plate surface S. The formulation of these fields can be found in Pierron and Grédiac, 2012, chapter 14. They provide C^1 continuous virtual deflections, which yield the required continuous virtual slopes. They also allow defining virtual displacements and slopes that are zero over the edges of each element, which eliminates unknown contributions

of virtual work along the plate boundaries. The definition of virtual fields over subdomains, also called piecewise virtual fields, provides more flexibility than globally defined virtual fields, in particular when unknown and complex load distributions are investigated. In the following, the subdomain over which a virtual field was defined is referred to as pressure reconstruction window (PRW). 9 nodes were defined for one PRW. All degrees of freedom were set to zero except for the virtual deflection of the center node, which was set to 1. One pressure value was calculated for each window. The size of the PRW has to be chosen according to the signal-to-noise ratio as well as the spatial distribution of the signal. Larger windows filter noise more efficiently, but can lead to a loss of signal amplitude and limit the spatial resolution.
Assuming constant pressure within a piecewise virtual field and approximating the integrals in equation 3 with discrete sums, one obtains a simplified expression for the pressure:

$$\begin{aligned} p \;=\; \Bigg(& D_{xx} \sum_{i=1}^{N} \kappa_{xx}^{i}\kappa_{xx}^{*i} + \kappa_{yy}^{i}\kappa_{yy}^{*i} + 2\;\kappa_{xy}^{i}\kappa_{xy}^{*i} \\ & +\; D_{xy} \sum_{i=1}^{N} \kappa_{xx}^{i}\kappa_{yy}^{*i} + \kappa_{yy}^{i}\kappa_{xx}^{*i} - 2\;\kappa_{xy}^{i}\kappa_{xy}^{*i} +\; \rho\; t_S \sum_{i=1}^{N} a^{i}\; w^{*i} \Bigg) \; \left(\sum_{i=1}^{N} w^{*i} \right)^{-1} \quad , \end{aligned} \tag{4}$$

where N is the total number of discrete surface elements dS^i.

3 Experimental Methods

3.1 Setup

The experiment consisted of a deflectometry setup with a reflective specimen and an impinging air jet (see fig. 2). The cross-hatched grid used for deflectometry was printed on transparency with 600 dpi using a *Konica Minolta bizhub C652* printer. A custom made panel with 9×100 W LEDs was used as white light source. The camera was placed at an angle beside the printed grid to record the reflected grid in normal incidence. 5400 images were recorded per deflectometry measurement series due to limited camera storage. A 1 mm thick first-surface glass mirror served as specimen. A fan-driven, round air jet was used to generate the investigated flow, which can be divided into a free jet, stagnation and wall region, *e.g.* Kalifa et al., 2016;

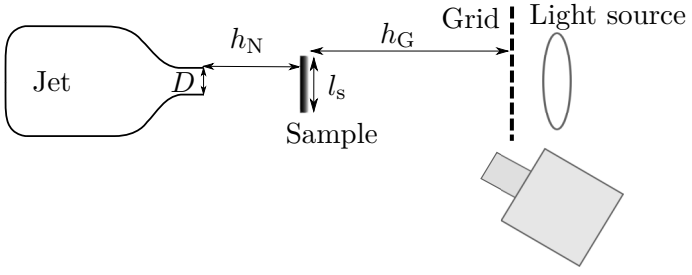

Figure 2: Experimental setup (redrawn from (Kaufmann et al., 2019a)).

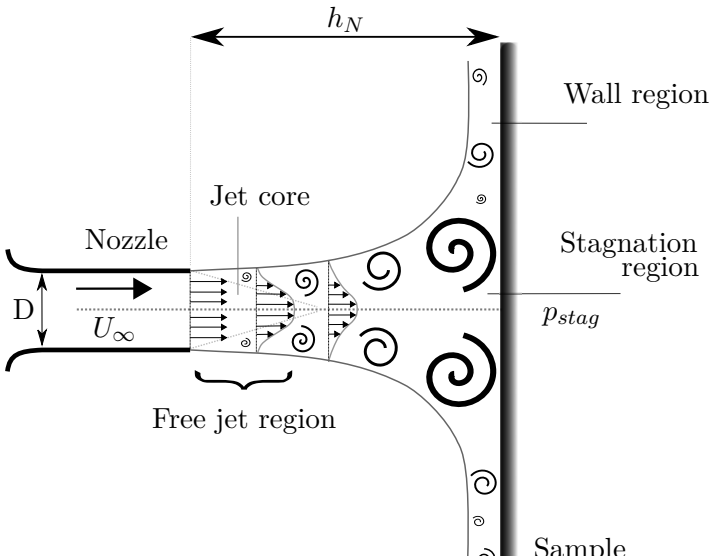

Figure 3: Impinging jet setup and flow features (redrawn from (Kaufmann et al., 2019a)).

Zuckerman and Lior, 2006 (fig. 3). So-called primary vortices form upstream in the shear layer around the jet core, propagate downstream and impinge on the specimen Zuckerman and Lior, 2006. The mean pressure distribution on the impingement surface is approximately Gaussian Beltaos, 1976. Table 1 lists the relevant experimental parameters.

3.2 Data Processing

One phase map was calculated from each image using the phase detection algorithm, with one data point per full grid pitch in each direction. Curvatures were calculated from slope maps with three-point centered finite differences. Deflections were obtained from the slope maps using an inverse (integrated) gradient based on a sparse approximation (D'Errico, 2009). The second time derivative of these deflections yields accelerations. However, this requires knowledge of the integration constant, *i.e.* of the deflection at one reference point at each time step. These were not measured in the present setup. Instead, plate deformations were assumed to be quasi-static, which allows neglecting the acceleration term in equation 4. Separate LDV measurements were used to obtain an estimate for the resulting error. VFM pressure reconstructions were conducted as described in section 2.2. The pressure reconstructions were oversampled in space by shifting the PRW by one data point in either direction until the entire surface was covered. Fig. 4 shows a flowchart of the main processing steps. For the calculation of standard deviations, data from 20 runs was used to improve convergence.

The mean pressure distributions obtained from time-resolved measurements in the present study are compared to the mean distributions obtained from uncorrelated snapshots in Kaufmann et al., 2019a. Figure 5 shows the azimuthally averaged mean pressure distribution for both methods and pressure transducer data for comparison. Even though the time-resolved measurements presented here suffer from a lower signal-to-noise ratio due to poorer illumination, the results agree well. It is clear that the mean flow was captured well using the VFM

Optics		
Camera		Photron Fastcam SA1.1
Technology		CMOS
Camera pixel size		20 μm
Surface Fill Factor		52 %
Dynamic range		12 bit
Settings		
Resolution		1024×1024 pixels
Frame rate	f_{aq}	4000 fps
Exposure		1/4000 s
ROI		64×64 mm^2
Magnification	M	0.32
f-number	N_{Lens}	32
Focal length	f_{Lens}	300 mm
Light source		LED panel, 900 W
Sample		
Type		First-surface mirror
Material		Glass
Young's modulus	E	74 GPa
Poisson's ratio	ν	0.23
Density	ρ	2.5·10^3 kg m^{-3}
Thickness	t_S	1 mm, 3 mm
Side length	l_s	ca. 90 *mm*, 190 *mm*
Grid		
Printed grid pitch	p_G	1.02 mm
Grid-sample distance	h_G	1.03 m
Pixels per pitch	ppp	8
Jet		
Nozzle shape		Round
Nozzle diameter	D	20 mm
Nozzle exit dynamic pressure	p_{exit}	630 Pa
Reynold's number	*Re*	4·10^4
Sample-nozzle distance	h_N	40 mm

Table 1: Setup parameters.

(to within 30%) in both the snapshot data and the time-resolved data. It was shown that this discrepancy between VFM and transducer data could be reduced to approximately 10% using a finite element correction procedure. This is comparable to or better than other optical based pressure determination techniques like PSP. Further details of the mean flow comparison and the selection of optimal pressure reconstruction parameters required to achieve this can be found in Kaufmann et al., 2019a. Given the agreement in the mean flow, the time-resolved data can now be further examined to obtain surface pressure fluctuations. These dynamic events were investigated here with two different filtering approaches.

First, a temporal bandpass filter was implemented by calculating the Fourier transform of

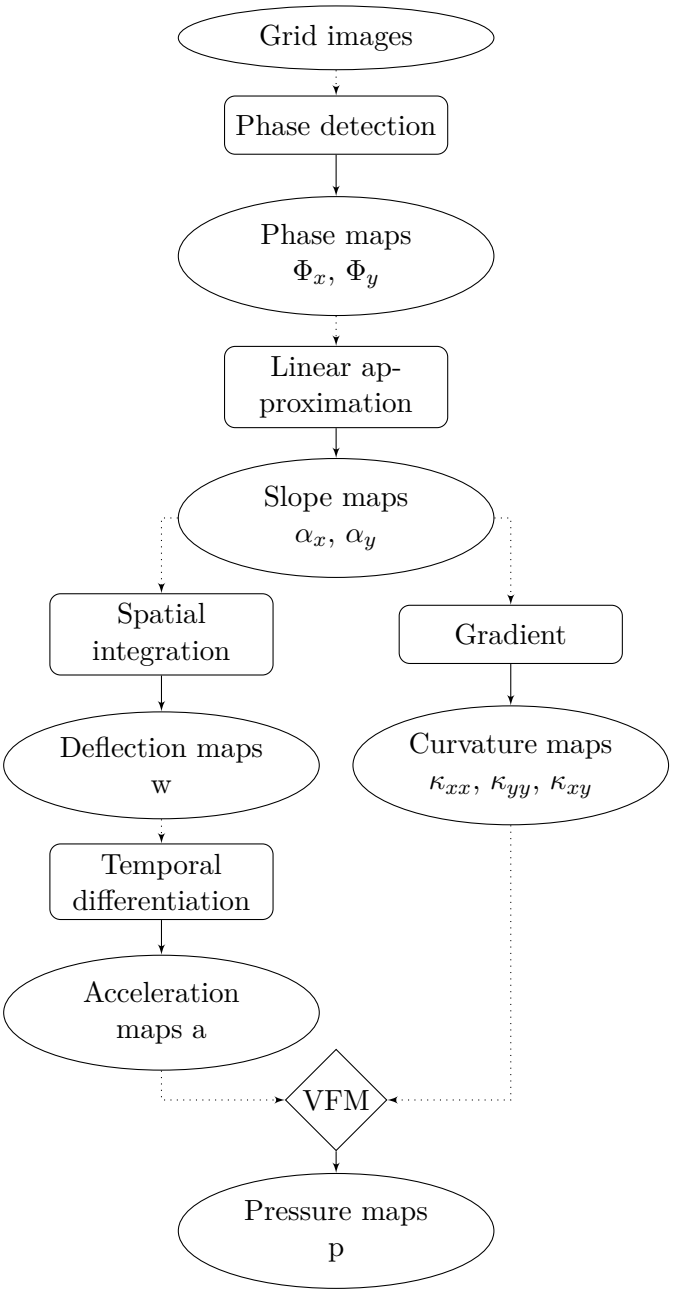

Figure 4: Data processing steps.

the slope maps and setting the amplitudes of filtered frequencies to zero. This filter has a poor impulse response, but yields the best achievable frequency resolution, which allows an application down to very narrow frequency bands. Second, Dynamic Mode Decomposition (DMD) Schmidt, 2010 was applied to instantaneous pressure reconstructions. The technique dedicated to using DMD on large and streaming data sets introduced in Hemati et al., 2014 was employed here.

3.3 Validation

Reference pressure measurements were conducted using Endevco 8507C-2 type pressure transducers. These transducers have a diameter of 2.5 mm. They were placed along a line beginning from the stagnation point radially outwards with a spacing of 5 mm. Accelerations were measured using a Polytec PDV 100 Laser Doppler Vibrometer (LDV). The acquisition frequency for both measurements was 4 kHz and the acquisition time 20 s.

3.4 Processing Parameters

A methodology for selecting optimal processing parameters based on simulated experiments and artificial grid deformation was proposed in Kaufmann et al., 2019a, section 5. It requires an estimate of the expected load distribution to obtain model slope maps. These allow to numerically deform a reflected grid image, which is used as input to the processing algorithm. By systematically varying the PRW size, its influence on pressure reconstruction can be evaluated to identify its optimal value.
Since this study aims at identifying dynamic events which are governed by the primary vortices impinging on the specimen, a circular load distribution with a peak amplitude of 10 Pa was chosen as model input (fig. 6a). The results of the analysis are shown in fig. 6b. The error estimate, ϵ, is defined as the difference between reconstructed and input pressure amplitude, $p_{rec,i}$ and $p_{in,i}$, divided by the local amplitude of the input pressure distribution at each point i:

$$\epsilon = \frac{1}{N}\sum_{i=1}^{N}\left|\sqrt{(p_{rec,i}-p_{in,i})^2}/p_{in,i}\right| , \tag{5}$$

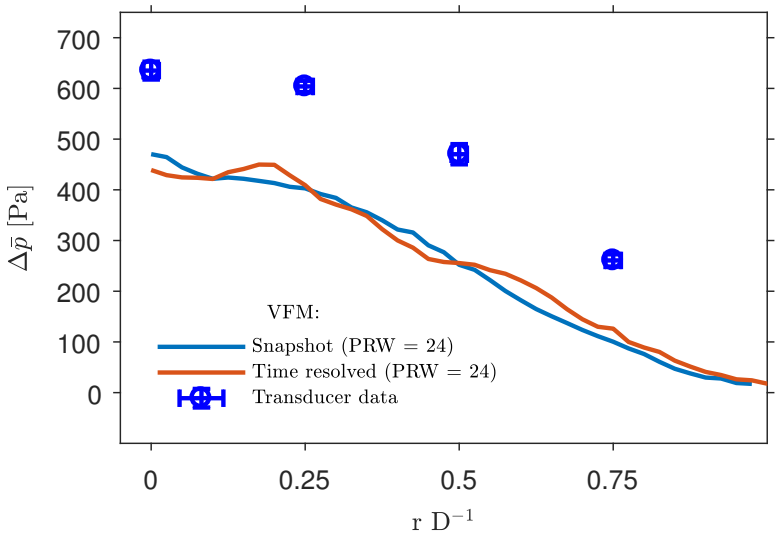

Figure 5: Comparison between transducer measurements and VFM pressure reconstructions for different processing parameters. r denotes the radial distance from the stagnation point. Snapshot and transducer data from Kaufmann et al., 2019a.

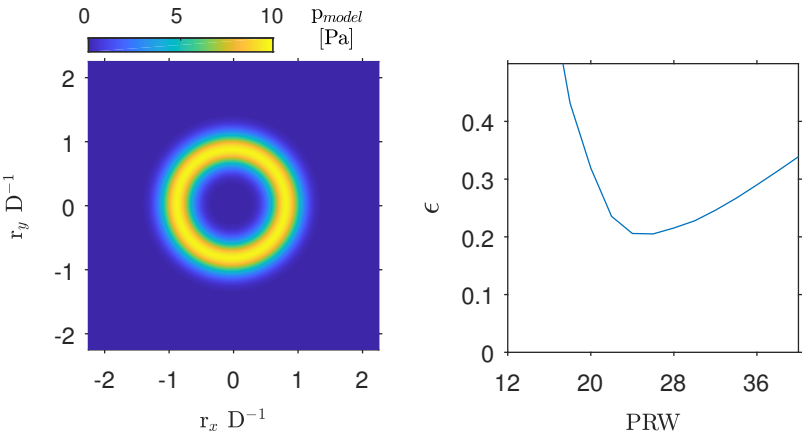

(a) Model input pressure distribution. r denotes the radial distance from the stagnation point, D the nozzle diameter. $rD^{-1} = 0$ is the stagnation point.

(b) Accuracy estimate from simulated experiment for model input data.

Figure 6: Simulated experiment input and results.

where N is the number of points. With an estimated average error of ca. 20%, PRW = 24 was identified as optimal size and will therefore be employed in the following. Note that a PRW side length of 24 data points corresponds to a physical distance of 12 mm. This PRW size and error is consistent with what was found for the mean flow. Despite the PRW size of 12 mm, it will be shown later that the spatial structures of the impinging vortices are well captured. The outcomes can be further improved by optimising the setup.

4 Experimental Results

4.1 Fluctuations

Instantaneous pressure maps were reconstructed from each measured slope map. The corresponding standard deviations, s_p, obtained from these maps allowed a first evaluation of the captured pressure fluctuations. Fig. 7a shows that the spatial distribution obtained for s_p appears to resemble noise patterns. This data was compared to pressure transducer measurements. VFM standard deviation results were averaged over all data points with the same radial distance from the stagnation point at $rD^{-1} = 0$. Fig. 7b shows that the VFM results significantly overestimate the standard deviations when compared to transducer data. The error bars show the estimated uncertainty of VFM pressure reconstructions from processing bias, experimental error and the assumption of quasi-static behaviour.

To investigate the reason for the poor agreement of these results, the Fourier spectra of deflectometry as well as transducer data were compared. The spectrum obtained from transducer data is shown in fig. 8a. Slope data (fig. 8b) was averaged over 21 data points which corresponds to an area of 5.3 mm^2, approximately matching the 4.9 mm^2 surface area of the pressure transducers. The comparison shows that the slope measurements capture relevant

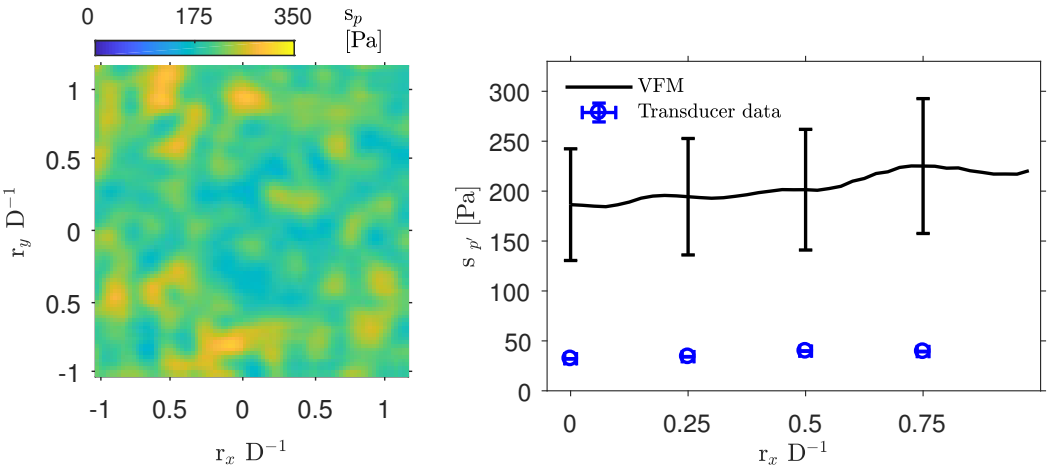

(a) Standard deviation of p_{qs}.

(b) Comparison of standard deviations of VFM and transducer data.

Figure 7: Pressure fluctuations obtained through VFM reconstructions from unfiltered slope data and comparison to transducer data.

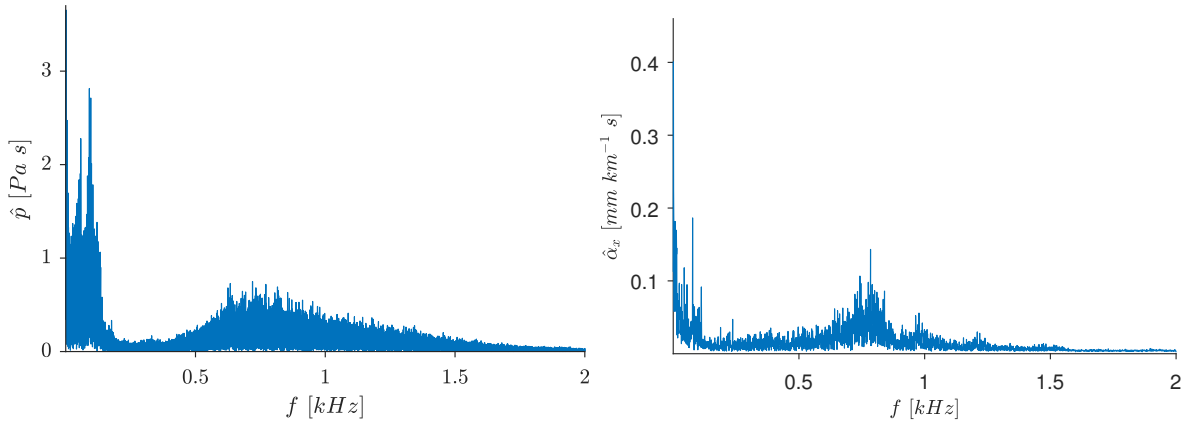

(a) Pressure spectrum from transducer data.

(b) Slope spectrum α_x.

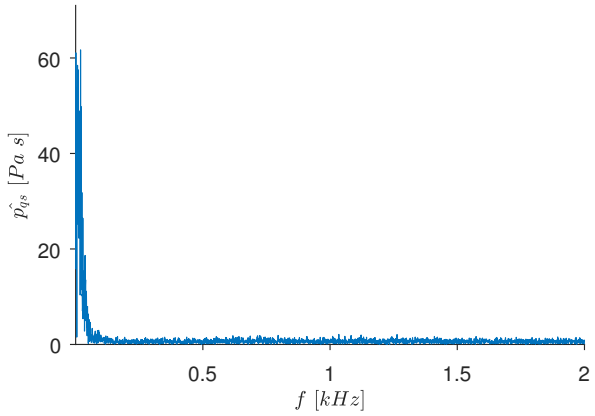

(c) Pressure spectrum from VFM reconstruction.

Figure 8: Qualitative comparison of Fourier spectra from different measurement sources on specimen surface at position $\mathrm{rD}^{-1} = 0$.

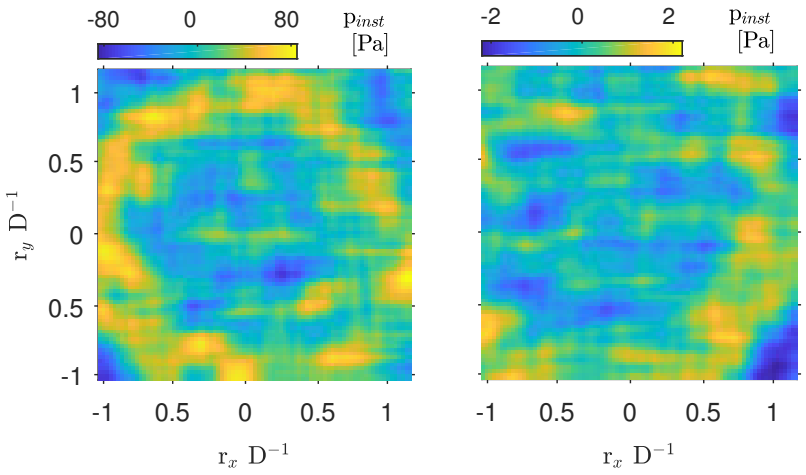

(a) Pressure reconstruction from slope maps filtered with bandpass range from 200 Hz to 1500 Hz.

(b) Pressure reconstruction from slope maps filtered with bandpass range from 700 Hz to 772 Hz.

Figure 9: Instantaneous VFM pressure reconstructions from temporally filtered slope data.

information on the dynamics of the impinging jet in the observed spectrum between ca. 200 Hz and 1500 Hz. However, the spectrum obtained from VFM pressure reconstructions (fig. 8c) shows only random noise for all frequencies above ca. 50 Hz. This suggests that low frequencies contain sufficient noise sources to overwhelm the signal when the slopes are converted to pressure using the VFM. This is likely because the VFM requires processing the slopes to accelerations (obtained from slopes by spatial integration and subsequent double temporal differentiation) and curvatures (computed from slopes by spatial differentiation). Obtaining these quantities appears to amplify noise to the extent that the low differential pressures are masked. However, the VFM is a linear method and therefore the methodology can be applied either to the entire range of frequencies or to specific frequency bands. If the method were applied to specific bands, then it might be possible to obtain the sought low differential pressure events since the lower frequency noise sources could be effectively filtered out. It is therefore necessary to employ further processing steps to extract dynamic pressure information from the slope measurements.

4.2 Temporal Filter

A temporal bandpass filter was applied to the slope maps (see section 3.5) in order to extract information on dynamic flow events in the identified relevant frequency range between 200 Hz and 1500 Hz. Fig. 9 shows instantaneous VFM pressure reconstructions from slope maps which were filtered within a broad (fig. 9a) and a narrow (fig. 9b) frequency band. The observed pressure distributions agree qualitatively with the expected distributions from primary vortices impinging on the flat surface.

The standard deviations of these VFM pressure reconstructions (fig. 10a and 11a) are compared with pressure transducer data, which are filtered within the same frequency band as

the slope maps (fig. 10b and 11b). The VFM reconstructions compare well with transducer data, particularly for the broader bandpass filter range. The discrepancy between both measurement techniques increases for $\mathrm{rD}^{-1} > 0.5$, which corresponds to the expected radius of the vortices and thus the area of their impingement. It is likely that the assumption of quasi-static behaviour leads to a larger error in this area.

The results show that information on surface pressure fluctuations was captured by the deflectometry measurements and that it is possible to reconstruct the corresponding pressure distributions and amplitudes with reasonable accuracy. It is now possible to employ further methods to address the low signal-to-noise ratio and to extract additional dynamic information from the data.

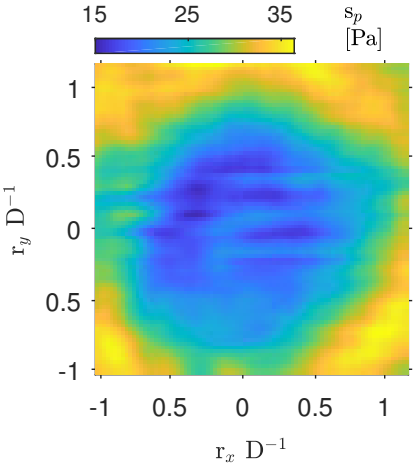

(a) Standard deviations of filtered pressure reconstructions.

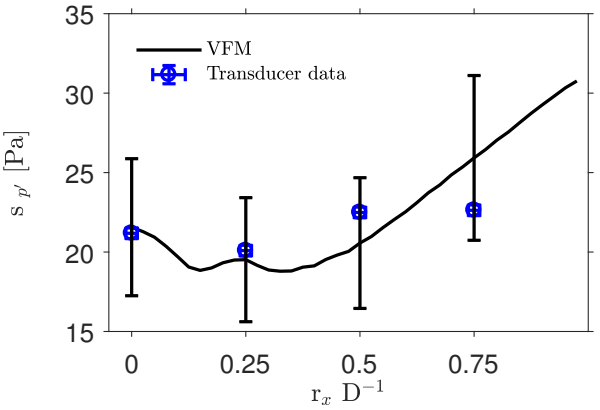

(b) Comparison of standard deviations from VFM reconstruction and transducer data.

Figure 10: Pressure fluctuations obtained using VFM reconstructions from slope data filtered with bandpass range from 200 Hz to 1500 Hz and comparison to filtered transducer data.

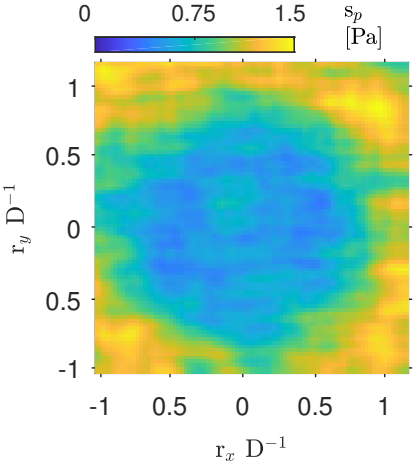

(a) Standard deviations of filtered pressure reconstructions.

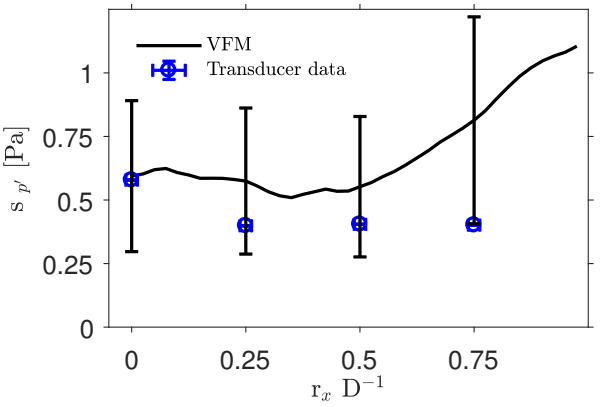

(b) Comparison of standard deviations from VFM reconstruction and transducer data.

Figure 11: Pressure fluctuations obtained using VFM reconstructions from slope data filtered with bandpass range from 770 Hz to 772 Hz and comparison to filtered transducer data.

4.3 Dynamic Mode Decomposition

Dynamic Mode Decomposition (DMD) is a suitable tool for extracting relevant dynamic information from a data sequence. It allows identifying spatially coherent features and their temporal behaviour within the entire observed frequency spectrum. The main challenge in applying this technique to the present case is that the computational cost and required resources increase with the amount of data points in space as well as with the number of snapshots. The approach introduced in Hemati et al., 2014 allows processing all instantaneous pressure maps by incrementally updating the calculated POD basis as well as the DMD modes and coefficients. It is therefore employed here.

DMD was applied to VFM pressure reconstructions from slopes which were filtered within a bandpass range from 200 Hz to 1500 Hz. This eliminated modes stemming from the mean flow and from low frequency experimental noise sources. The calculated POD basis was truncated at 200 modes, since higher modes primarily stem from random noise. Fig. 12a and 12b show

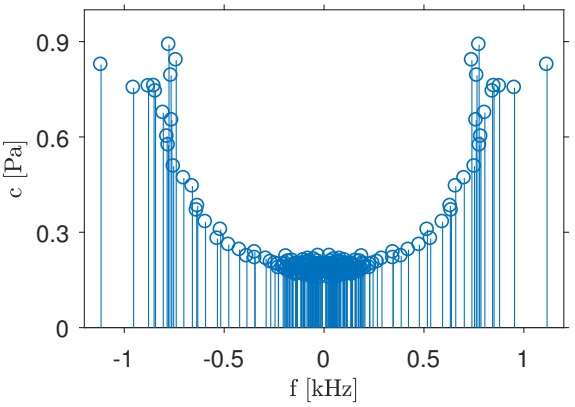

(a) DMD amplitude coefficients.

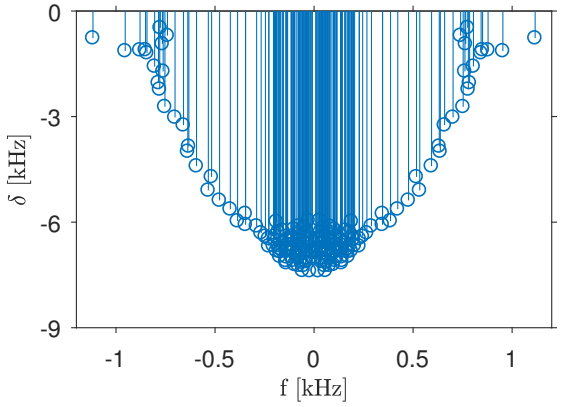

(b) DMD damping coefficients.

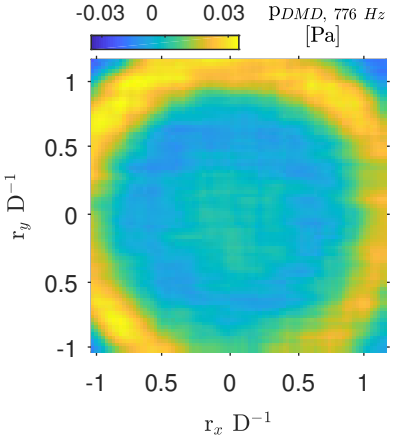

(c) Streaming DMD pressure reconstruction of 776 Hz mode at t = 0.

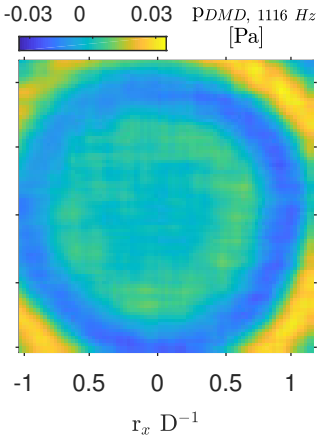

(d) DMD pressure reconstruction of 1116 Hz mode at t = 0.

Figure 12: DMD results obtained with $108{\cdot}10^3$ snapshots from VFM pressure reconstructions using slope maps which were bandpass filtered within the range from 200 Hz to 1500 Hz. 200 POD modes were calculated.

the amplitude and damping coefficients. The modes identified for frequencies below 200 Hz stem from noise introduced by data processing, since this frequency range was filtered out from the slope information. These modes resemble noise patterns, have low amplitude and high damping coefficients. The most relevant modes corresponding to the impinging primary vortices were identified to be around 770 Hz. They have the highest amplitude and the lowest damping coefficients of all identified modes. Examples of pressure reconstructions from two modes are shown in fig. 12c and 12d. The modal shapes are coherent with only small amounts of noise and resemble the expected spatial distributions. A video of the 776 Hz mode with damping coefficient set to zero can be found in the supplementary material of this paper.
This clearly shows that the low differential pressure events generated by impinging vortices were captured by the new surface pressure determination method. It is important to note here that the differential pressure amplitude captured here is $\mathcal{O}(1)$ Pa, which would be impossible to capture in full-field with any extant measurement technique. More importantly, we are now able to identify the spatio-temporal evolution of the pressure footprint of flow structures on a surface, which was previously not possible. Combining deflectometry and VFM with flow information will allow investigations of the flow-structure interactions in more detail. To improve this methodology for further applications requires considerations of the error sources and future ways in which these can be minimised. This is discussed in the next section.

5 Error Sources

This section discusses the systematic error sources encountered in the experimental setup as well as in the processing technique. In terms of experimental error sources, several elements of the deflectometry setup should be considered. Irregularities in the recorded grid as well as miscalibration, *i.e.* non-integer numbers of pixels per grid pitch, can lead to errors in the detected phases. The main factors causing these irregularities are damages on the specimen surface and defects of the printed grid. Miscalibration can be caused by misalignments between camera sensor and printed grid, as well as by irregularities and harmonics in the printed grid. Misalignment can also result in fringes. These error sources and their effect are highly dependent on the precise alignment between grid, specimen surface and camera. They can further be time dependent, because the specimen deforms under the dynamic load. Using the LDV to measure vibrations of the camera, it was also found that the camera cooling fans caused vibrations at several frequencies below 100 Hz, which were also identified in the measured slope spectrum. Based on comparisons with numerical data presented in Kaufmann et al., 2019a, the effect of these experimental errors could amount to up to 10% of the peak pressure value for the mean flow.
An additional issue concerning experimental bias is that the mechanical constitutive material parameters provided by the plate manufacturer, in particular the Young's modulus, may not be accurate. In Kaufmann et al., 2019a it was estimated that the resulting error on pressure amplitudes was up to 10%.

The systematic error resulting from the processing approach employed in this study was investigated in Kaufmann et al., 2019a. VFM pressure reconstructions were found to underestimate the local amplitudes because the virtual fields act as a low pass spatial filter over the area of a reconstruction window. The exact error value depends on the chosen reconstruction parameters as well as the investigated load distribution and signal-to-noise-ratio. In the present study, the error associated with data processing can be estimated using the analysis presented in section 3.4. It is approximately 20% for instantaneous pressure maps when using a PRW size of 24 data points side length. Note that this estimate does not take into account the influence of random noise or the filtering techniques.
The error resulting from assuming quasi-static behaviour was assessed using LDV measurements to obtain accelerations at discrete points along the specimen surface. Values of up to 1.4 ms^{-2} were found for the standard deviation of the accelerations. A worst case estimate for the resulting error in pressure was obtained by assuming an acceleration value of $a = 1.4$ ms^{-2} over the entire specimen. The resulting dynamic pressure value was calculated using the acceleration term in equation 4. For pressure reconstructions from unfiltered slopes, it yields a value of $p_{dyn} = 84$ Pa, which corresponds to approximately 13% of the estimated peak pressure amplitude of 630 Pa. For reconstructions from bandpass filtered slopes, significantly lower error values were identified. Using a bandpass filter range of 200 Hz to 1500 Hz for slope maps, worst case estimates of $a = 0.1$ ms^{-2} and $p_{dyn} = 6$ Pa were obtained. For the filter range of 770 Hz to 772 Hz, these values were further reduced with $a = 0.01$ ms^{-2} and $\mathrm{p}_{dyn} = 0.6$ Pa. Based on the low amplitude of noise patterns in the extracted dynamic pressure distributions, it appears that experimental errors from the deflectometry setup were filtered efficiently. The systematic processing errors as well as the assumption of quasi-static behaviour are likely to result in an underestimation of instantaneous pressure reconstructions, which can be estimated to up to 30%. The latter is also the most likely reason for the increasing discrepancy between pressure fluctuations identified from transducer data and from VFM reconstructions when moving into the region in which vortices first impinge on the plate.

6 Limitations and Future Work

Low-amplitude differential pressure fluctuations were extracted from VFM pressure reconstructions using two techniques. However, in order to achieve convergence and due to the low signal-to-noise ratio, a large number of snapshots was required. This is a challenge for available high-speed cameras due to limited storage and data transfer rates. Experiments based on phase-locked measurements can address this issue. This also allows using cameras with higher resolutions, which can be combined with smaller grid pitches to increase slope resolution. Slope resolution can also be improved by increasing the distance between grid and sample, though the quality and availability of suitable camera lenses is an issue. Another limitation of the approach presented here is that the specimen is required to be of optical mirror quality. Non-mirror-like, but reasonably smooth surfaces were successfully used for deflectometry measurement using an infrared camera and heated grids Toniuc and Pierron,

2018. Due to the relatively long wavelength of infrared light, sufficiently specular reflection for slope measurements was achieved using unpolished metal plates as well as perspex with approximately 1.5 μm surface RMS roughness. An approach for applications of deflectometry measurements to curved surfaces is proposed in Surrel and Pierron, 2019. Though the results were promising, a sophisticated calibration was required and time-resolved measurements are currently not possible. For future studies, the present setup could be improved to obtain accurate acceleration information. This could potentially be achieved by simultaneously measuring deflections at a known point in the field of view using an LDV. Finally, improved virtual fields and higher order pressure reconstruction approaches could reduce the systematic processing error of the VFM.

7 Conclusion

This study presents an approach for obtaining full-field dynamic pressure information from surface slope measurements. Surface slopes were measured using a highly sensitive deflectometry setup. Pressure reconstructions were obtained using the VFM. The extracted differential pressure amplitudes range down to few $\mathcal{O}(1)$ Pa. 85×85 data points were obtained, corresponding to a field of view of 4.25 $cm \times 4.25$ cm. The VFM pressure reconstruction results were compared to pressure transducer data. Results were found to agree well for band pass filtered data. DMD was used to extract relevant dynamic information. Error sources associated with experimental limitations and the processing technique were identified and discussed. The achieved high data point density and the low magnitude of the extracted pressure amplitudes make the presented technique highly relevant for a large range of applications in engineering and science.

8 Data Provision

All relevant data produced in this study will be made available upon publication of this manuscript.

Acknowledgements This work was funded by the Engineering and Physical Sciences Research Council (EPSRC). F. Pierron acknowledges support from the Wolfson Foundation through a Royal Society Wolfson Research Merit Award (2012-2017).

Paper 3

Surface pressure reconstruction from phase-averaged deflectometry measurements using the Virtual Fields Method

R. Kaufmann, F. Pierron, B. Ganapathisubramani

Faculty of Engineering and Physical Sciences, University of Southampton, Southampton SO17 1BJ, UK

Intended for submission to the Journal Experimental Mechanics

Abstract In this study, pressure distributions were reconstructed from phase-locked surface deformation measurements on a thin plate. Slope changes on the plate surface were induced by an external flow interacting with the specimen and measured with a highly sensitive deflectometry setup. The Virtual Fields Method (VFM) was used to obtain pressure reconstructions from the processed surface slopes and the plate material constitutive mechanical parameters. The applicability of the approach in combination with phase-locked measurements is demonstrated using a synthetic jet setup generating a periodic flow in air. Phase-averaging slope data allows mitigating random noise effects and resolving low-range differential pressure amplitudes despite the turbulent flow. The size of the spatial structures of the investigated low amplitude flow events identified in full-field with the present method are $\mathcal{O}(1)$ mm, which is beyond the capabilities of other available pressure measurement techniques. Challenges and limitations in achieving the metrological performance for resolving the observed surface slopes of $\mathcal{O}(0.1)$ mm km^{-1} are described and improvements for future applications are discussed.

1 Introduction

Full-field surface pressure information is required for the research of flow-structure interactions, the design of aerodynamic components, and applications for heat and mass transfer. Extant techniques are limited in terms of the differential pressure amplitude ranges that can be resolved and in terms of the achievable spatial resolutions. Particle Image Velocimetry (PIV) is a technique that allows full-field investigations of pressure in the flow field, *e.g.* de Kat and van Oudheusden, 2012; Jaw et al., 2009, but cannot be applied directly on a surface. Pressure sensitive paints, *e.g.* Tropea et al., 2007, chapter 4.4, yield full-field surface pressure information directly on surfaces, but are typically restricted to limited ranges of large differential pressure amplitudes. Pressure transducers allow accurate measurements for low-range differential pressures. They can be integrated into the investigated surface by drilling holes into the specimen. This can however change the material response. In order to investigate surface pressure distributions, a large number of pressure transducers is required, which then still yield very limited spatial resolution.

A number of studies have focused on obtaining pressure information from optical deformation measurements on surfaces instead. This was achieved by solving the mechanical equilibrium equations of the investigated specimen. A common problem of these approaches is that regularization is necessary in order to mitigate the influence of experimental noise. *E.g.* in Brown et al., 2018, deflections measured with 3D-Digital Image Correlation on a flexible Kevlar wind tunnel wall section were projected onto polynomial basis functions to reconstruct pressure using the equilibrium equation. In other studies, surface deformation measurements on thin plates were used as basis for force and pressure reconstruction. The local equilibrium equation for a thin plate in pure bending, which can be obtained using the Love-Kirchhoff theory, requires fourth-order deflection derivatives to calculate pressure. This leads to an amplification of the experimental noise and thus increases the need for regularization. In Pezerat and Guyader, 2000; Lecoq et al., 2014, noise amplification was addressed using wave number filters on the deformation data, which was obtained with Laser Doppler Vibrometer (LDV) measurements. These were used to solve the equilibrium equation and identify external mechanical vibration sources, as well as the acoustic component of a turbulent boundary layer.

To address the issues of experimental noise and noise amplification due to differentiation, the Virtual Fields Method (VFM), which is based on the principle of virtual work, has been used in a series of studies. In case of the problem of a thin plate in pure bending, the principle of virtual work only requires second order spatial derivatives of the surface deflections to calculate pressure. It was used in combination with LDV measurements to reconstruct spatially-averaged sound pressure levels in Robin and Berry, 2018, transverse loads and vibrations in Berry et al., 2014, random external wall pressure excitations in Berry and Robin, 2016 and sound transmission of plates in Robin and Berry, 2018. These studies used piecewise virtual fields, which allow pressure reconstructions over subdomains and act as as a spatial low-pass filter. In the above studies, numerical simulations and microphone measurements revealed that the performance of the method varies with the chosen size of the subdomains and that it can be affected by the structural resonance frequencies of the thin plate specimen. In order to acquire time-resolved full-field pressure information, the VFM was combined with optical measurements using deflectometry in recent studies. Since deflectometry is a technique for the measurement of surface slopes (Surrel et al., 1999), this combination reduces the order of derivatives of experimental data for calculating pressure with principle of virtual work to two. Dynamic mechanical point loads were measured this way in O'Donoughue et al., 2017. In Kaufmann et al., 2019a, pressure reconstructions of an impinging air jet on a flat plate were obtained for mean distributions. The study also addressed the accuracy and systematic processing error of the approach, as well as a procedure to mitigate the latter. Dynamic loads of the same impinging jet were reconstructed in Kaufmann et al., 2019b. The slope resolution in these experiments were of the order of $\mathcal{O}(1)\ mm \cdot km^{-1}$. The surface slopes caused by dynamic flow events were well below this limit, such that they could not be measured directly. Instead, the spatio-temporal evolution of low differential pressure events in the flow were extracted using a temporal filter and Dynamic Mode Decomposition (DMD).

The present study explores an alternative approach for obtaining low-range differential pressure amplitudes in dynamic flows. It further aims at resolving flow events on small spatial

scales of $\mathcal{O}(1)$ mm. Phase-locked deflectometry measurements were used to measure pressure distributions caused by an impinging synthetic air jet. This allowed implementing changes in the deflectometry setup that improve the metrological performance to resolve the surface slopes caused by the low differential pressure events. The dynamic range and signal-to-noise ratio in grid images was improved by using a flash light to achieve an optimal illumination. This was a shortcoming in Kaufmann et al., 2019b, where continuous lighting was required for the time-resolved measurements. Since camera storage is not an issue for phase-locked measurements, it was further possible to use higher camera resolutions. These allowed using smaller pitches for the hatched grid which was used as spatial carrier signal in the deflectometry setup. Smaller grid pitches increase the spatial resolution as well as the resolution in slope, allowing measurements of the extremely small deformations associated with the investigated flow events.
This study demonstrates the feasibility of the approach as well as its limitations and discusses possible improvements for future applications.

2 Deflectometry

Deflectometry is an optical full-field slope measurement technique (Surrel et al., 1999). Figure 1 shows a schematic of the setup. It requires a periodic spatial signal, here a cross-hatched grid with printed pitch p_G, a specular reflective specimen, a camera and a light source. The printed grid is placed at a distance h_G from the specimen surface. The camera is placed at an angle next to the grid, such that it records the reflected grid in normal incidence. The angle θ should be minimized to avoid distortions in the recorded image.
The principle of deflectometry is also visualized in figure 1. In an unloaded specimen configuration, a camera pixel records the reflected grid point P when directed at point M on the specimen surface. In a loaded configuration, deformations cause local changes of the surface slopes, $d\alpha$. Neglecting rigid body movements and out-of-plane deflections, this means that the pixel directed at point M records the reflected grid point P′ after the surface deformation.
Recorded grid images can be used to extract phase information and thus the phase shift induced by applying a load to the specimen. Here, a spatial phase-stepping algorithm was employed to obtain phase maps (Surrel, 1996; Poon et al., 1993). In order to suppress some harmonics and errors from miscalibration, a detection algorithm featuring a windowed discrete Fourier transform algorithm with triangular weighting was used (Surrel, 2000; Badulescu et al., 2009). The chosen detection kernel size was two grid pitches, here 18 pixels.
The phase maps obtained from the unloaded reference configuration and the deformed configuration allow calculating the displacement, $\boldsymbol{u}$, between P and P′. To account for the physical displacement of the point on the specimen surface, an iterative procedure is employed, which is described in Grédiac et al., 2016, section 4.2:

$$\boldsymbol{u}_{n+1}(\boldsymbol{x}) = -\frac{p_G}{2\pi}(\phi_{def}(\boldsymbol{x} + \boldsymbol{u}_n(\boldsymbol{x})) - \phi_{ref}(\boldsymbol{x})) \quad , \tag{1}$$

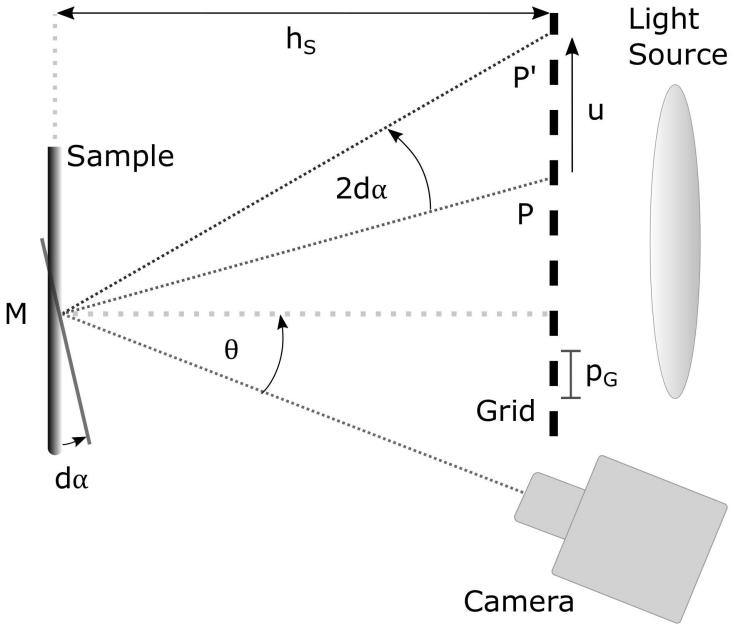

Figure 1: Top view of deflectometry setup and working principle (redrawn from Kaufmann et al., 2019a).

A linear approximation of the slopes dα corresponding to $\boldsymbol{u}$ can be derived using geometrical considerations, assuming that dα is small, $h_G \gg \boldsymbol{u}$, θ is negligible and that the camera records images in normal incidence (*e.g.* Ritter, 1982):

$$d\alpha_x = \frac{u_x}{2h_G}, \quad d\alpha_y = \frac{u_y}{2h_G} \quad . \tag{2}$$

If the assumptions are not met, a more complicated full calibration is required (Balzer and Werling, 2010; Surrel and Pierron, 2019). The printed grid pitch p_G drives the spatial resolution. The slope resolution is driven by measurement noise, the printed grid pitch p_G and the distance h_G, the spatial resolution by p_G.

3 Pressure Reconstruction

Assuming that the plate material is linear elastic, isotropic and homogeneous, the principle of virtual work is expressed by:

$$\begin{aligned} \int_S p\ w^* dS \ &= \ D_{xx} \int_S \left(\kappa_{xx}\kappa^*_{xx} + \kappa_{yy}\kappa^*_{yy} + 2\ \kappa_{xy}\kappa^*_{xy} \right) dS \\ &+ \ D_{xy} \int_S \left(\kappa_{xx}\kappa^*_{yy} + \kappa_{yy}\kappa^*_{xx} - 2\ \kappa_{xy}\kappa^*_{xy} \right) dS + \ \rho\ t_S \int_S a\ w^* dS \quad , \end{aligned} \tag{3}$$

where S denotes the surface area, p the investigated pressure, D_{xx} and D_{xy} the plate bending stiffness matrix components, κ the curvatures, ρ the plate material density, t_S the plate thickness, a the acceleration, w^* the virtual deflections and κ^* the virtual curvatures. In the

present study D_{xx}, D_{xy}, ρ and t_S were known from the plate manufacturer. κ and a were obtained from deflectometry measurements. The virtual fields w^* and κ^* have to be chosen according to theoretical as well as practical restrictions of the problem such as continuity, boundary conditions and sensitivity to noise.
Assuming pressure to be constant over the investigated area yields a simplified equation. Approximating the integrals with discrete sums yields:

$$\begin{aligned} p \;=\; \Bigg(& D_{xx} \sum_{i=1}^{N} \kappa_{xx}^{i}\kappa_{xx}^{*i} + \kappa_{yy}^{i}\kappa_{yy}^{*i} + 2\;\kappa_{xy}^{i}\kappa_{xy}^{*i} \\ & + \; D_{xy} \sum_{i=1}^{N} \kappa_{xx}^{i}\kappa_{yy}^{*i} + \kappa_{yy}^{i}\kappa_{xx}^{*i} - 2\;\kappa_{xy}^{i}\kappa_{xy}^{*i} + \;\rho\; t_S \sum_{i=1}^{N} a^{i}\; w^{*i} \Bigg) \left(\sum_{i=1}^{N} w^{*i} \right)^{-1} \quad , \end{aligned} \tag{4}$$

where N is the total number of discrete surface elements dS^i. By defining this equation over subdomains of the total surface area, pressure distributions can be reconstructed iteratively. These subdomains are referred to as pressure reconstruction windows (PRW) in the following. In the present study, the spatial data was oversampled by overlapping these windows.

3.1 Virtual Fields

Virtual fields were defined with 4-node Hermite 16 element shape functions, which are used in FEM Zienkiewicz, 1977. The full formulation of these fields as well as an implementation example can be found in Pierron and Grédiac, 2012. They yield the required C^1 continuous virtual deflections and continuous virtual slopes. They further allow eliminating the unknown contributions of virtual work over the plate boundaries because the obtained virtual displacements and curvatures vanish at the borders. Here, 9 nodes were defined for one PRW. All degrees of freedom were set to zero except for the virtual deflection of the center node, which was set to 1.

4 Experimental Methods

4.1 Setup

Figure 2 shows a schematic of the experimental setup. A first-surface glass mirror was used as specimen. The grid was printed on transparency and fixed between two glass plates. A flash light was used for illumination. The light source was placed behind the grid. The camera was placed next to the grid at the same distance from the specimen, recording images at normal incidence. The distance between the sample and grid was chosen to be as large as possible in order to minimise the angle θ.
A synthetic jet was used to generate the flow impinging on the specimen. It was generated using a driver connected to a cavity with orifice. The driver changes the cavity volume, inducing a pressure difference which results in fluid being either sucked in or ejected through the orifice.

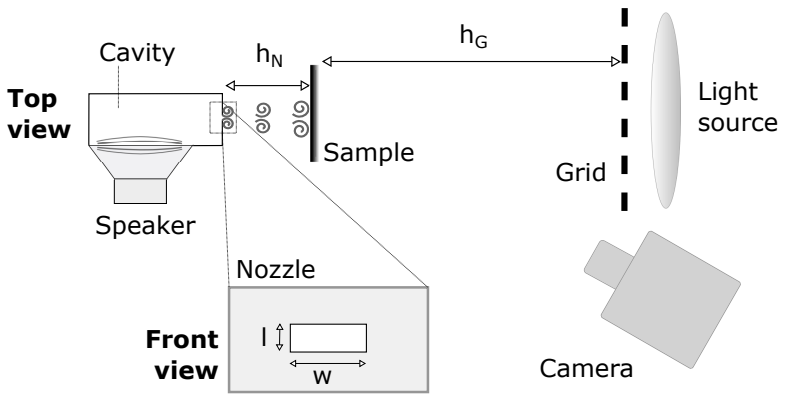

Figure 2: Experimental setup and nozzle geometry.

During ejection, vortical structures form around the edges of the nozzle exit due to shear. For sufficiently small Strouhal numbers $St < \pi^{-1}$, the fluid forming the vortices around the edge of the orifice is not sucked back into the cavity but convects downstream (Holman et al., 2005). If the actuator is operated continuously, this leads to a train of vortices (Glezer and Amitay, 2002). Here, a rectangular nozzle was used as orifice. For such nozzle symmetries, the vortices form structures with a major and a minor axis upon formation, which deform after some distance downstream and switch axes (*e.g.* Amitay and Cannelle, 2006; Van Buren et al., 2014; Chen and Yu, 2014). They eventually break down entirely and form a turbulent jet (Glezer and Amitay, 2002). The jet was driven by a speaker which was actuated using a sinusoidal signal, generating a continuous train of vortices. The jet was directed at the flat plate specimen. Depending on the distance between nozzle and plate, either the described vortical structures or a circular turbulent jet impinge on the plate, leading to an increase of static pressure and a subsequent diversion of the flow along the wall, *e.g.* Xu and Wang, 2016a. All relevant experimental parameters are listed in table 1. The jet amplitude is given in terms of the peak-to-peak input voltage amplitude of the speaker, U_{pp}, as well as the peak velocity at the nozzle exit, v_{peak}, which was determined using hot wire anemometry measurements. Two jet setups were used to investigate the capabilities in resolving high and low differential amplitudes, as well as different spatial shapes. Since the sample plate was found to deform over time, *e.g.* due to temperature fluctuations, a set of images for unloaded and loaded configuration was taken for each phase sample.

4.2 Data Processing

Each phase map was calculated from a set of grid images taken in an unloaded and a loaded configuration. The slope maps were calculated from phase maps which were averaged from approximately 500 snapshots. In order to mitigate the amplification of noise in later processing steps, slope maps were smoothed using a 2D Gaussian filter. The filter kernel is characterised by its side length, which is given in terms of the standard deviation σ_α. Here, the side length was truncated at $3\sigma_\alpha$ in both directions. This low-pass filter reduces the effect of both random noise and high-frequency bias, but also leads to a reduction of the signal amplitude. Note that

Optics		
Camera		Imperx IGV-B6620M
Technology		CCD
Camera pixel size		5.5 μm
Surface Fill Factor		98%
Dynamic range		8 bit
Maximum resolution		6600×4400 pixels
Settings		
Used resolution		4400×4200 pixels
Exposure		1/2000 s
ROI		73.3×70 mm^2
Magnification	M	0.33
f-number	N_{Lens}	32
Focal length	f_{Lens}	300 mm
Light source		Bowens Gemini Pro 1000 Flash
Sample		
Type		First-surface mirror
Material		Glass
Young's modulus	E	74 GPa
Poisson's ratio	ν	0.23
Density	ρ	2.5 10^3 kg m^{-3}
Thickness	t_S	1 mm
Grid		
Printed grid pitch	p_G	0.3 mm
Grid-sample distance	h_G	ca. 1000 mm
Pixels per pitch	ppp	9
Jet		
Actuator		Acoustic speaker Visaton SC 8 N
Nozzle shape		Rectangular
Slot length	l	1 mm
Slot width	w_S	8 mm
Jet frequency	f	100 Hz
Sample-nozzle distance	h_N	25 mm, 10 mm
Jet amplitude	U_{pp}	20 V, 46 V
Peak velocity at nozzle exit	v_{peak}	31 m s^{-1}, 45 m s^{-1}

Table 1: Setup parameters.

this Gaussian filter leads to a loss of data points around the borders, depending on the filter kernel size.

Three-point centered finite differences were used to differentiate slope maps and calculate curvatures. Using geometrical considerations, one can determine that the distance between two data points on the specimen surface, which is required for the finite differences, is $p_G/2$ if the camera is positioned at the same distance h_G from the specimen surface as the printed grid.

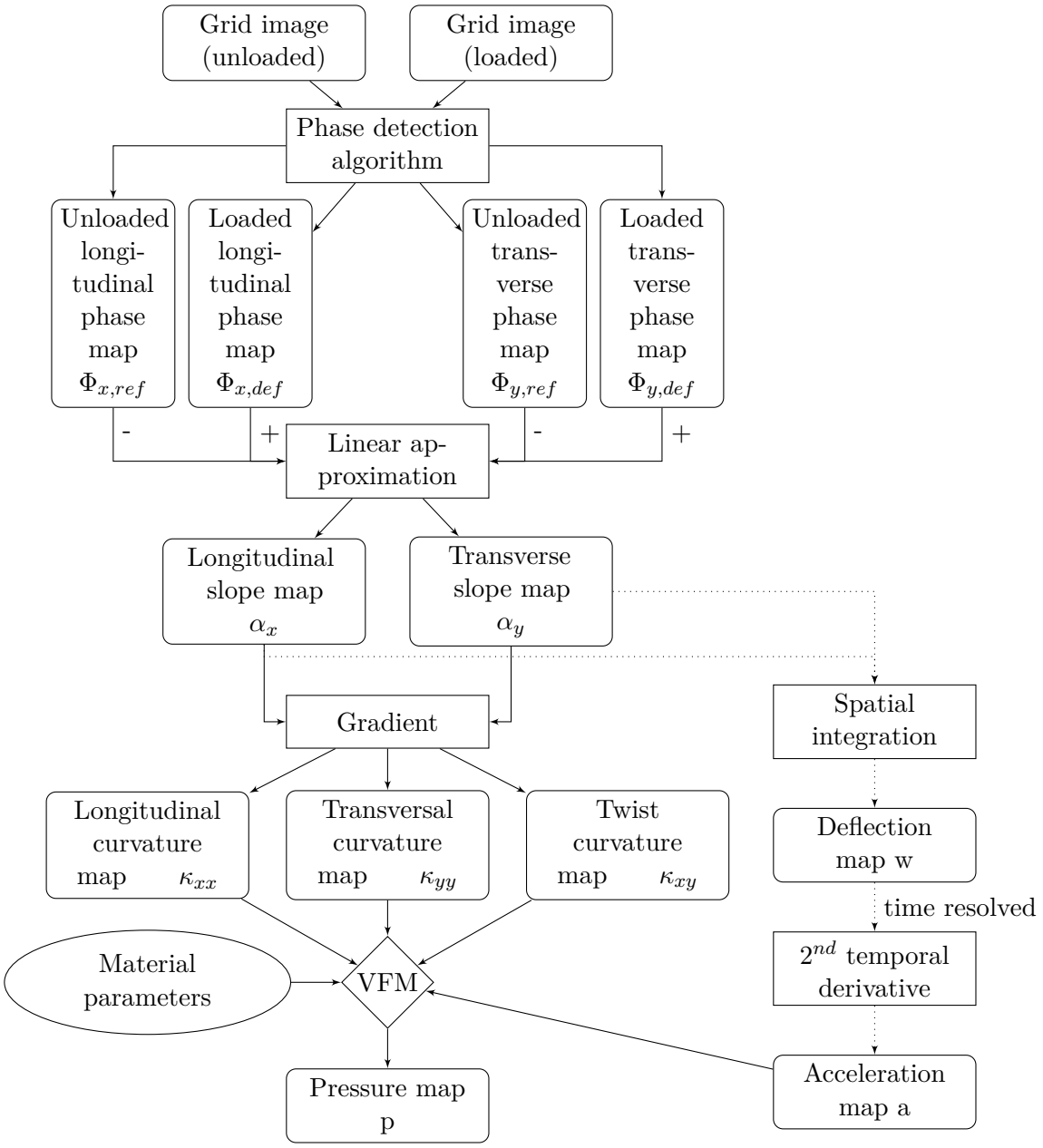

Figure 3: Data processing steps for reconstruction of quasi static pressure maps from deflectometry measurements.

Deflections were obtained from the slope maps using an inverse (integrated) gradient based on a sparse approximation (D'Errico, 2009). Accelerations were then obtained from the second temporal derivative of the deflection maps. The acquired deflections and accelerations did however show unexpected distributions for a number of phase points. It is possible that the number of acquired phase points were insufficient to resolve accelerations accurately. Further, since the integration constant for calculating deflections was unknown and set to 0, a comparison with an established measurement technique was necessary. Accelerations were however found to be below the noise level of 0.3 m s^{-2} found for the Polytec PDV 100 laser Doppler vibrometer which was used for reference measurements. Fig. 4 shows deflections and accelerations obtained from slope measurements using a high amplitude jet setup with $U_{\mathrm{pp}} = 23\ V$ and

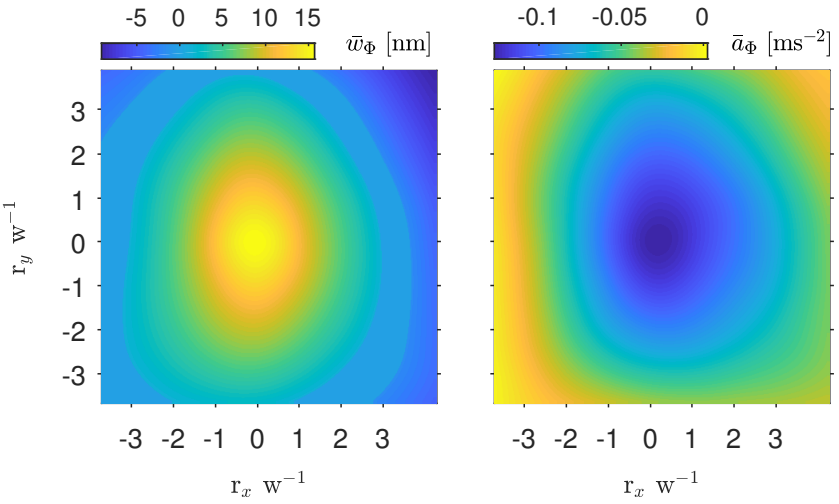

(a) Deflection map. (b) Acceleration map.

Figure 4: Phase averaged deflections and accelerations for $\Phi = 15 \cdot \frac{2\pi}{20}$. $U_{\mathrm{pp}} = 23$ V, $h_{\mathrm{N}} = 10$ mm.

$h_{\mathrm{N}} = 10$ mm. Higher acceleration amplitudes of up to 0.4 m s^{-2} were observed for different phase points, but with unexpected and asymmetric distributions. Since LDV measurements did not confirm these values and due to the potential inaccuracy of the results, accelerations were not taken into account and set to 0 in the following. The resulting error in pressure amplitude from neglecting accelerations can be estimated to up to 35 Pa.

Pressure maps were reconstructed using the curvatures and the material constitutive mechanical parameters as described in section 3. The results were oversampled by shifting the reconstruction window by one data point in both directions until the full field of view was covered. The reconstruction steps are summarised in fig. 3.

4.3 Processing Parameters

The chosen processing parameters, in particular the slope filter kernel size, σ_α, and the PRW size, significantly impact the pressure reconstruction outcome. Large PRW sizes act as more efficient low-pass filter, but can lead to an underestimation of pressure amplitude and average out small-scale spatial distributions. Kaufmann et al., 2019a introduced a methodology for selecting optimal processing parameters in terms of local pressure amplitudes. It addresses the complex interactions between pressure signal, random noise and systematic processing errors. In the present study however, random noise is averaged out reasonably well due to the large number of snapshots, while systematic experimental error sources significantly impact the pressure reconstructions. These errors cannot be modelled because of their unkown distribution and magnitude. Further, in this work the identification of flow structures with small spatial scales of $\mathcal{O}(1)$ mm is more relevant than the accuracy in pressure amplitude. It was therefore necessary to determine the optimal reconstruction parameters empirically. The

potential increase in the systematic processing error of the pressure amplitude associated with non-optimal parameters was addressed using the finite element correction procedure described in Kaufmann et al., 2019a.

5 Experimental Results

5.1 Pressure Reconstructions

Fig. 5a-5b and 6a-6b show averaged slope maps obtained from phase-locked measurements for one phase and for both investigated jet setups. These were used to calculate the corresponding curvature maps (fig. 5c - 5e and 6c - 6e). The noise patterns found in curvature maps indicate the presence of systematic experimental error sources. Without slope smoothing, they can overwhelm the signal from the impinging jet. Pressure reconstructions for 2 different phases for a nozzle exit velocity of 31 m s^{-1} and a distance of 10 mm between nozzle and sample, h_N, are shown in fig. 7. $\sigma_\alpha = 8$ and PRW = 12 were used as reconstruction parameters. Due to experimental noise, differential pressure amplitudes below approximately 1 Pa could not be resolved here and were set to 0 to mitigate noise patterns. Fig. 7a shows the phase with the highest observed peak pressure amplitude for this setup. The elongated shape of the vortex structure, which originates from the rectangular nozzle, is clearly visible. The orientation of the long and short axis is switched compared to the nozzle orientation (see section 4.1). Since the dynamic pressure decreases with the downstream distance due to entrainment and turbulent decay, the reconstructed peak amplitude of 450 Pa is consistent with the approximately 1200 Pa dynamic pressure that corresponds to the peak velocity at the nozzle exit. Pressure reconstructions for the second jet setup with nozzle exit velocity of 19 m s^{-1} and $h_N = 25$ mm are shown in fig. 8. Due to the low signal-to-noise ratio, $\sigma_\alpha = 7$ and PRW = 42 were used as reconstruction parameters. The position of the jet impinging in the center of the specimen was identified for both presented phase points. Due to the large downstream distance, the pressure amplitude is significantly reduced compared to the 540 Pa peak dynamic pressure at nozzle exit, and the vortical structure with minor and major axes has decayed into a turbulent jet with approximately Gaussian profile. The negative differential pressure region identified around the center indicates the presence of a vortex ring entraining fluid while moving along the specimen surface, which is consistent with the findings of studies focusing on the flow field, *e.g.* Xu and Wang, 2016b. Fig. 7a shows the phase with the lowest reconstructed pressure amplitude for which the position of the impinging jet could be identified. Pressure maps for the remaining phase points yield similar results, depending on the pressure amplitudes during the respective phase. The position of the impinging jet could not be identified for a number of phase points, indicating that the amplitudes encountered in these cases are too low to be detected with the present setup. The pressure reconstruction results for all phases and both setups can be found in appendix 1.

It should be noted that the observed spatial distributions and pressure amplitudes could not be validated with any established measurement techniques. Pressure transducers, which are

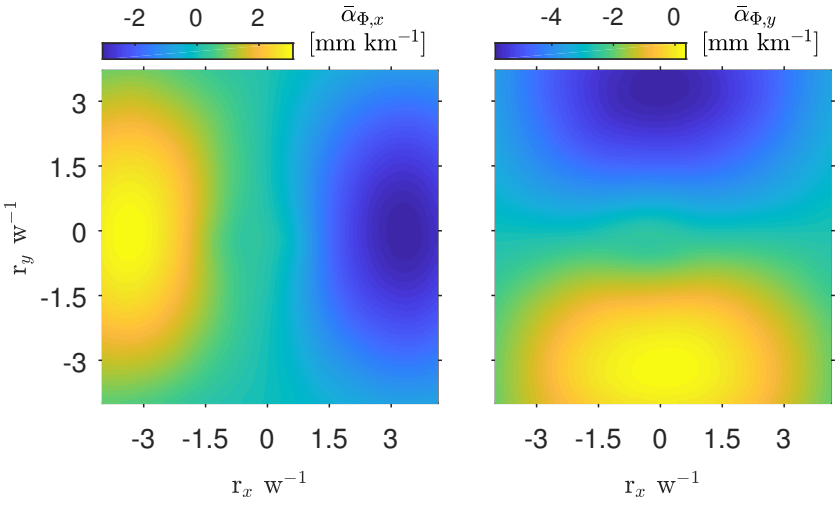

(a) Transversal slopes. (b) Longitudinal slopes.

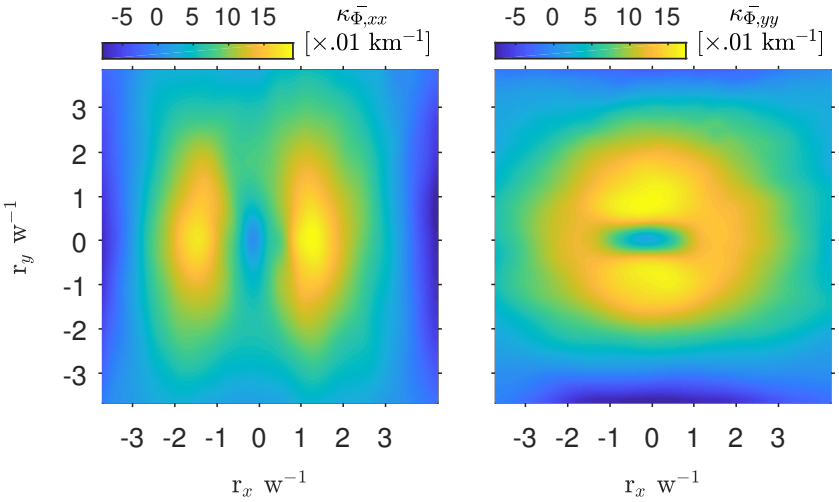

(c) Transversal curvatures ($\sigma_\alpha = 8$). (d) Longitudinal curvatures ($\sigma_\alpha = 8$).

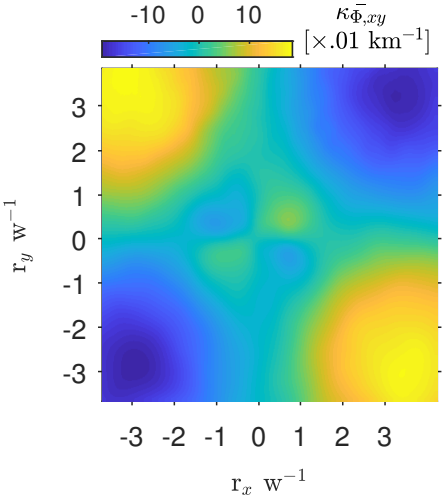

(e) Twist curvatures ($\sigma_\alpha = 8$).

Figure 5: Phase averaged slope maps and curvature maps for $\Phi = 1\ \frac{2\pi}{20}$. $U_{\text{pp}} = 46$ V, $h_{\text{N}} = 10$ mm.

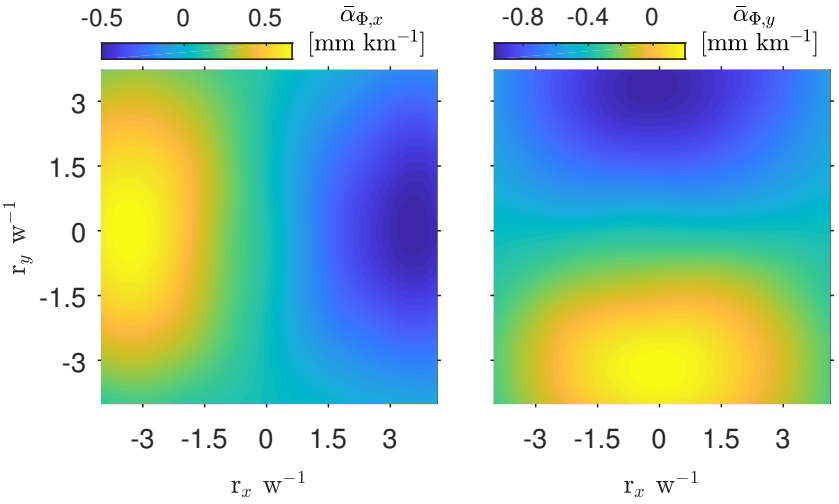

(a) Transversal slopes.

(b) Longitudinal slopes.

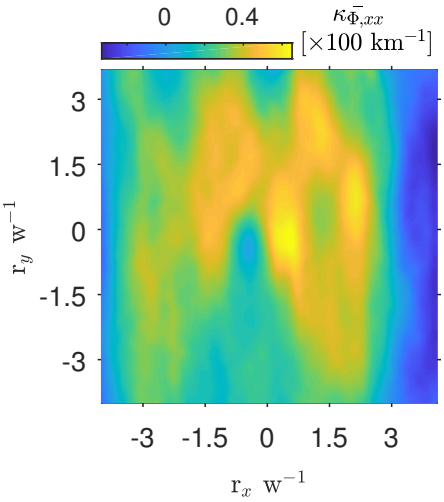

(c) Transversal curvatures ($\sigma_\alpha = 7$).

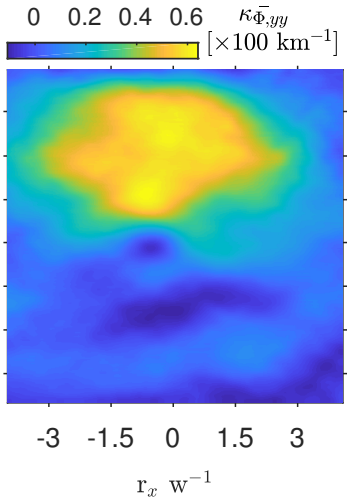

(d) Longitudinal curvatures ($\sigma_\alpha = 7$).

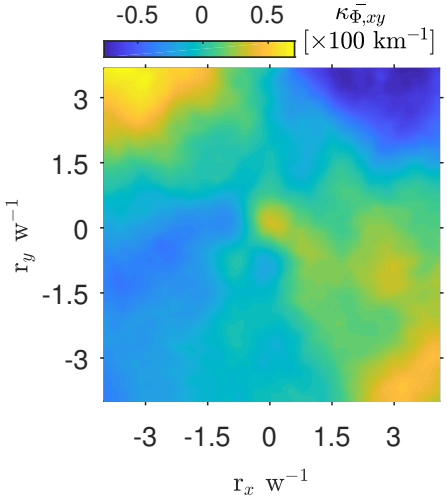

(e) Twist curvatures ($\sigma_\alpha = 7$).

Figure 6: Phase averaged slope maps and curvature maps for $\Phi = 1\ \frac{2\pi}{20}$. $U_{\text{pp}} = 20$ V, $h_{\text{N}} = 25$ mm.

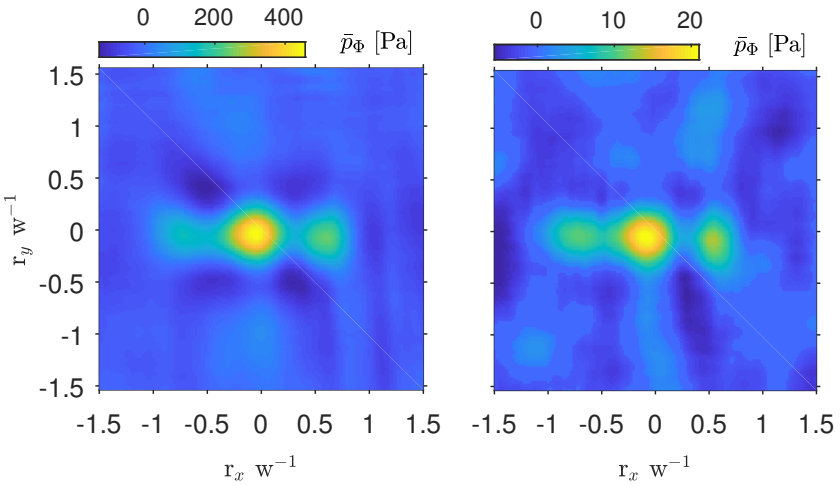

(a) Pressure for $\Phi = 1\ \frac{2\pi}{20}$. (b) Pressure for $\Phi = 16\ \frac{2\pi}{20}$.

Figure 7: VFM pressure reconstructions from phase averaged slope maps. $U_{\text{pp}} = 46$ V, $h_{\text{N}} = 10$ mm, $\sigma_\alpha = 8$, PRW = 12.

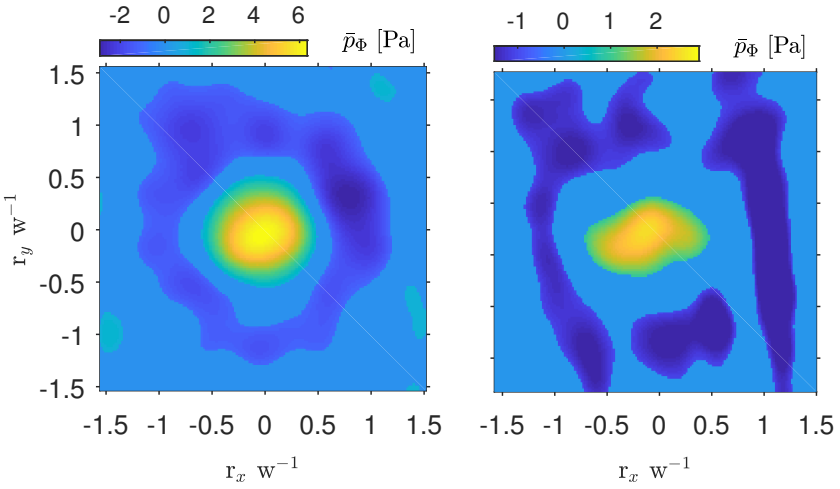

(a) Pressure for $\Phi = 1\ \frac{2\pi}{20}$. (b) Pressure for $\Phi = 13\ \frac{2\pi}{20}$.

Figure 8: VFM pressure reconstructions from phase averaged slope maps. $U_{\text{pp}} = 20$ V, $h_{\text{N}} = 25$ mm, $\sigma_\alpha = 7$, PRW = 42.

often used to measure low differential pressure amplitudes, do not only provide an insufficient amount of data points, but also average over too large of an area due to their surface diameter of typically $2 - 3$ mm. Other full-field techniques cannot resolves the low differential pressure amplitudes or are not applicable to surfaces.

5.2 Finite Element Correction

Due to systematic errors in data processing, VFM pressure reconstruction can lead to underestimations of the local pressure amplitudes. In Kaufmann et al., 2019a it was shown that the resulting error can be mitigated using a finite element correction procedure, which is employed

in the following. In a first step, slope maps are calculated from a VFM pressure reconstruction, p_{rec}, using a finite element simulation. Processing the thus obtained slope maps yield a new pressure distribution, p_{it}. The difference between p_{rec} and p_{it} reflects the systematic processing error for this particular distribution. It can be interpreted as a first estimate for the systematic error between the real distribution and p_{rec}. Adding this difference to p_{rec} yields a corrected pressure distribution, p_{cor}:

$$p_{\mathrm{cor,\,n}} = p_{\mathrm{rec}} + (p_{\mathrm{rec}} - p_{\mathrm{it,\,n}}) \quad , \tag{5}$$

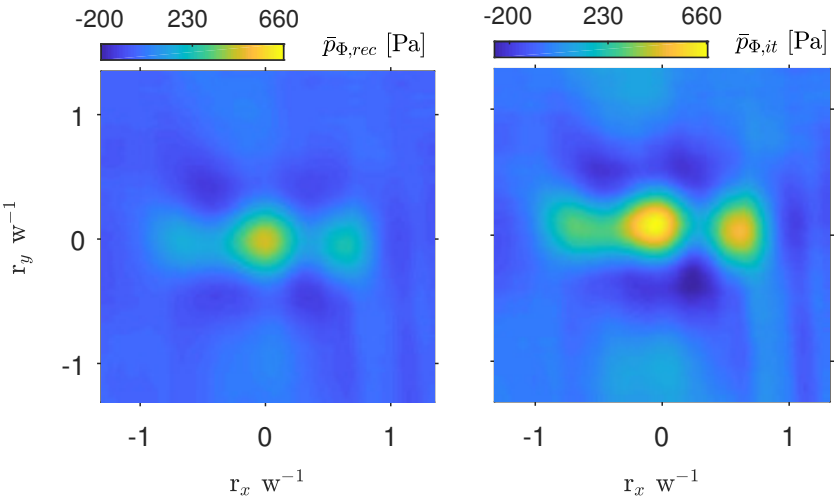

(a) Input pressure reconstruction.

(b) Corrected pressure distribution after 1 iteration.

Figure 9: Input distribution and iterated result for finite element correction for $\mathrm{U_{pp}} = 46$ V, $\mathrm{h_N} = 10$ mm and $\Phi = 1\ \frac{2\pi}{20}$.

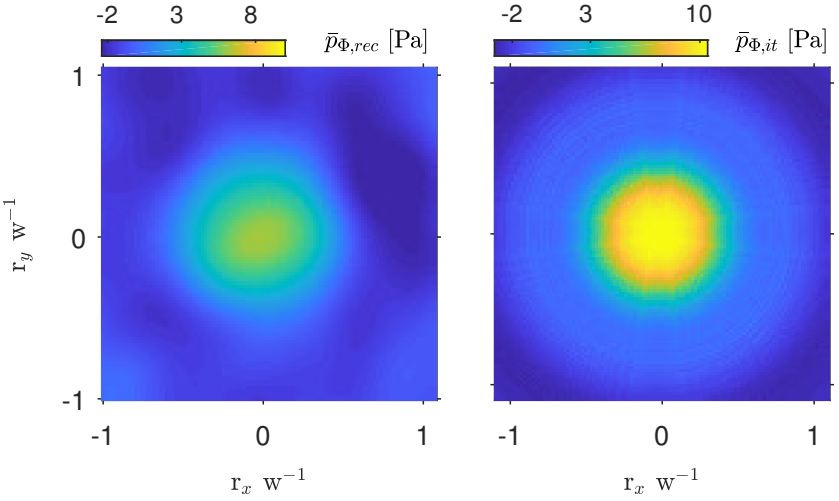

(a) Input pressure reconstruction.

(b) Corrected pressure distribution after 3 iterations.

Figure 10: Input distribution and iterated result for finite element correction for $\mathrm{U_{pp}} = 20$ V, $\mathrm{h_N} = 25$ mm and $\Phi = 1\ \frac{2\pi}{20}$.

where n is the number of iterations. It was found that this method yields well converged results after 1-3 iterations for the investigated cases. In Kaufmann et al., 2019a numerical data was used to show that the original load distribution can be approximated very closely for noise-free data with this procedure.
Here, only one iteration was performed because the correction procedure was found to amplify noise patterns which affect the lower amplitude region of the vortex shape. The peak pressure amplitudes of the shown corrected distribution is approximately 25% higher than that of the original reconstruction. Note that the field of view is reduced around the borders with each iteration, depending on the size of the spatial slope filter kernel and the PRW. For cases with low signal-to-noise ratio, it was necessary to address the noise patterns found in pressure maps, since they are typically amplified by the procedure. Since the pressure distributions found for large distances between nozzle and sample are approximately symmetric, this was achieved by averaging the pressure values for each radial distance from the stagnation point. Fig. 10a shows the original pressure reconstruction from experimental data, and fig. 10b the averaged and corrected distribution. The peak pressure amplitudes of the corrected distribution are $10\% - 35\%$ higher than that of the original reconstructions, depending on the investigated phase point.

6 Error Sources

This section discusses experimental and data processing errors affecting the obtained pressure amplitudes and distributions, as well as the origin of the observed noise patterns. First, systematic errors resulting from phase detection and VFM should be considered. They depend on the chosen reconstruction parameters, particularly the size of the slope filter kernel σ_α and PRW, the investigated load distribution as well as the signal-to-noise-ratio. In Kaufmann et al., 2019a the systematic error was investigated in detail for Gaussian pressure distributions and for different signal-to-noise ratios. In the present study it is difficult to quantify the amount of random noise because slopes were calculated from sets of reference and deformed grid images and averaged, and because the noise patterns stemming from systematic error sources cannot be reliably distinguished from random noise patterns. However, the results of the finite element correction (see section 5.2) can be interpreted as an estimate for the systematic processing error (see also Kaufmann et al., 2019a, chapters 5-6). It can be estimated to be up to 35% of the local amplitude for uncorrected pressure reconstructions.
In order to estimate the error associated with neglecting inertia (quasi-static plate behaviour), acceleration measurements were conducted using a LDV. The accelerations on the specimen surface were however found to be below the noise level of 0.3 ms^{-2}. As a worst case estimate, a value of 0.3 ms^{-2} can be assumed for the accelerations at every data point. The corresponding dynamic pressure value depends on the PRW window size and is $5 - 35$ Pa in the present case. Note that since the accelerations could not be resolved for any setup with the LDV, this is an estimate of the error for the high-amplitude jet setup using $U_{\mathrm{pp}} = 23$ V and $h_{\mathrm{N}} = 10$ mm. The worst-case error estimate is therefore below 8% of the observed peak amplitude. However, if

these acceleration were to occur at phases with low pressure amplitude, the associated error in pressure would be of the order of the identified pressure amplitudes. For the lower amplitude jet setup, accelerations can be assumed to be far lower and thus negligible.
Finally, experimental error sources need to be considered. The deflectometry setup is susceptible to misalignments between printed grid and camera sensor, miscalibration, as well as grid defects and damages on the reflective surface. All of these can lead to errors in phase detection. Misalignment is the likely cause for the vertical stripes observed in several pressure maps. Note that the acquisition time for each phase point was more than 30 min, such that factors like temperature fluctuations and strained cables may have caused small displacements during measurements. As the investigated printed grid pitch was very small with 0.3 mm and 9 pixels were used to record one reflected grid pitch, these would be sufficient to cause the observed misalignment, despite careful initial arrangement. It should also be noted that the Young's modulus of the specimen, which is s a linear factor in pressure calculation, was only measured to within 10% (Kaufmann et al., 2019a).
Even though the accumulated potential uncertainty in the identified pressure amplitudes is relatively high, the overall results agree with the magnitudes expected from the applied nozzle exit velocities and downstream distances. The identified spatial distributions correspond to the expected shapes of the vortical structures for the investigated downstream distances.

7 Limitations and Future Work

The presented VFM pressure reconstructions show that it is possible to obtain high resolution pressure measurements of low-range differential amplitudes with phase-locked deflectometry measurements. Even lower pressure amplitudes can potentially be resolved in future studies by addressing experimental error sources, thus mitigating noise patterns. This could be achieved by using translation stages for the positioning of grid, specimen and camera to address the issue of misalignment. Smaller grid pitches would further increase slope resolution and spatial resolution. Since not all available camera pixels were used in the present study, this would be relatively easy to achieve by changing the printed grid and the camera lens. Slope resolution can also be improved by choosing a larger distance between grid and specimen. However, the availability of suitable camera lenses is a restricting factor.
Improving the performance of the VFM by optimising the virtual fields or the pressure determination with higher order approaches could reduce the systematic processing error. These could also allow using smaller PRW sizes, effectively increasing the spatial resolution.

8 Conclusion

This study presents an approach for full-field pressure reconstructions from phase-locked optical surface slope measurements. A highly sensitive deflectometry setup was used to obtain slopes on a specular reflective specimen. The VFM was used to reconstruct pressure from the

experimental data and the material mechanical constitutive parameters of the flat plate specimen. It was shown that it is possible to obtain physically meaningful pressure distributions with amplitudes of $\mathcal{O}(1)$ Pa – $\mathcal{O}(100)$ Pa and spatial extent of $\mathcal{O}(1)$ mm – $\mathcal{O}(10)$ mm with this approach. The identification of lower pressure amplitudes was limited by noise patterns originating from experimental error sources. Possible improvements for addressing this issue in future studies were discussed. The results are outstanding in terms of the small spatial scales and pressure amplitudes which were identified in full-field.

9 Data Provision

All relevant data produced in this study will be made available upon publication of this manuscript.

Acknowledgements This work was funded by the Engineering and Physical Sciences Research Council (EPSRC).

Part III

Summary

Chapter 5

Recommendations and Future Work

A number of limitations and requirements was identified that allow general recommendations for the future use of deflectometry and the VFM for surface pressure reconstructions.
Finite element simulations and simulated experiments are a substantial support in designing the experimental setups. They help to predict suitable sample stiffness parameters and the printed grid pitches which are required to resolve the investigated load amplitudes and distributions. Camera fill factor, the number of pixels per recorded grid pitch and signal-to-noise ratio can also be simulated to determine whether the image sensor and illumination are suitable for a given setup. Simulated experiments further allow choosing appropriate reconstruction parameters for processing. This is particularly important for applications where a wide range of pressure events can occur simultaneously, *e.g.* in investigations of turbulent flows or other random excitation sources. Particularly small-scale flow events may be filtered out or confused with noise patterns when using ill-suited reconstruction parameters. Comparing simulated and real experiments also helps to identify patterns stemming from systematic experimental error sources like fringes or specimen surface deformations, which can be difficult to distinguish from the investigated signal.
A general issue was the precise alignment between grid, camera and sample. If available, micro stages and stepper motors should be used to facilitate the arrangement of these setup components. As applying the investigated load can induce surface deformations of several μm, test images in unloaded as well as loaded configurations should be taken before each experiment to make sure that no fringes occur in curvature maps. Other factors that may introduce errors in phase detection are harmonics in the printed grid, grid defects, deformations and damages of the sample surface, aberration and other camera lens imperfections, and the fill factor of the image sensor.
For tests with high shutter speed, the choice of the light source is crucial. Many common light sources produce substantial amounts of heat. This can cause density gradients in the air between grid, sample and camera, which can distort the light beams. If placed too closely to grid or sample heat can cause deformations and damages. Cooling fans on the light source (or camera) cause vibrations that are likely detectable in the signal.
A shortcoming of the present study was that accelerations could not be measured accurately.

The main challenge in obtaining these was the determination of the integration constant that is required to calculate instantaneous deflections. It was initially assumed that the deflections in the corners of the relatively large region of interest would not change over time, which was not confirmed. It may be possible to address this issue by physically fixing the specimen in a small area in the field of view in order to prevent variations of deflections over time, or by simultaneously measuring deflections at a known point in the field of view using an LDV.

A main challenge in the application of the presented experimental approach is that the investigated surfaces have to be mirror-like and plane, which are major restrictions for practical engineering applications. Recently, deflectometry measurements were extended to moderately curved surfaces in Surrel and Pierron, 2019. Though promising results were obtained, time-resolved measurements are currently not possible with this approach. Further, it requires a calibration and the required depth of field is a restricting factor for the use in combination with small grid pitches. A successful combination of deflectometry measurements on curved surfaces with the VFM would be of great value, as it would allow pressure reconstructions directly on practically relevant surfaces like *e.g.* aerofoils, fuselages and ship hulls. A combination with the VFM is however challenging because in-plane displacements are generally not negligible on curved surfaces.

The requirement of mirror-like surfaces could be addressed by using infrared instead of visible light sources for deflectometry. This was achieved with heated grids as spatial carrier in Toniuc and Pierron, 2018. Since infrared light has a longer wavelength than visible light, specular reflection can be achieved on specimens that do not have mirror-like but reasonably smooth surfaces with up to about 1.5 μm of RMS roughness, like perspex and metal plates. Current restrictions are the lack of an aperture ring and that available infrared cameras are limited in terms of spatial and temporal resolutions. Further, the lenses required to achieve comparable magnification are more expensive. A combination of infrared deflectometry measurements with the VFM may allow measurements directly on *e.g.* walls of water tanks or flumes.

Finally, the pressure reconstruction approach and the selection of virtual fields is an important factor in addressing the systematic error of the technique. Varying the virtual fields would also allow investigating the issue of lower accuracy for decreasing reconstruction window sizes. Further, the assumption of constant pressure over a reconstruction window is clearly inaccurate, such that linear or higher order approaches are likely to yield improved results.

Chapter 6

Conclusion

This thesis investigated the capabilities and limitations of full-field surface pressure reconstructions from deflectometry measurements with the Virtual Fields Method. Surface slopes of $\mathcal{O}(0.1)$ mm km^{-1} – $\mathcal{O}(10)$ mm km^{-1} were measured with the highly sensitive deflectometry setup. The VFM was used to reconstruct surface pressure information using the full-field deformation measurements and the material constitutive mechanical parameters. The data obtained with this technique allowed extracting mean and dynamic pressure distributions with low-range differential amplitudes of $\mathcal{O}(1)$ Pa – $\mathcal{O}(100)$ Pa and spatial extent of $\mathcal{O}(1)$ mm – $\mathcal{O}(10)$ mm. The results are presented in three papers which form the core of this thesis. The key findings of the study are summarized in the following.

- Static pressure distributions were reconstructed from time-averaged slope measurements.
- The influence of the processing parameters was investigated using experimental and model data.
- Simulated experiments employing a finite element model and artificial grid deformation were used to assess the uncertainty of the method.
- The numerical results were used to select optimal reconstruction parameters, taking into account experimentally observed noise.
- VFM pressure reconstructions were compared quantitatively to pressure transducer measurements.
- A finite element correction procedure was proposed to mitigate the systematic error of VFM pressure reconstructions.
- Temporal filters were used to extract dynamic information which was compared to transducer measurements.
- Dynamic Mode Decomposition (DMD) was used to identify relevant spatial information that correspond to specific frequencies.

- Phase-locked measurements were employed to directly measure dynamic flow events.
- Error sources were discussed based on the findings of both the experimental and the simulated results.
- The limitations of the approach as well as possible improvements for future studies and applications were discussed.

The results are outstanding in terms of the small spatial scales and the low differential amplitudes of the identified surface pressure distributions, as well as the high data point density that was achieved. These key features make the investigated technique highly relevant for a large range of applications in engineering and science.

Appendix A

Experimental Data

1 Pressure reconstructions from phase-locked slope measurements (Paper 3)

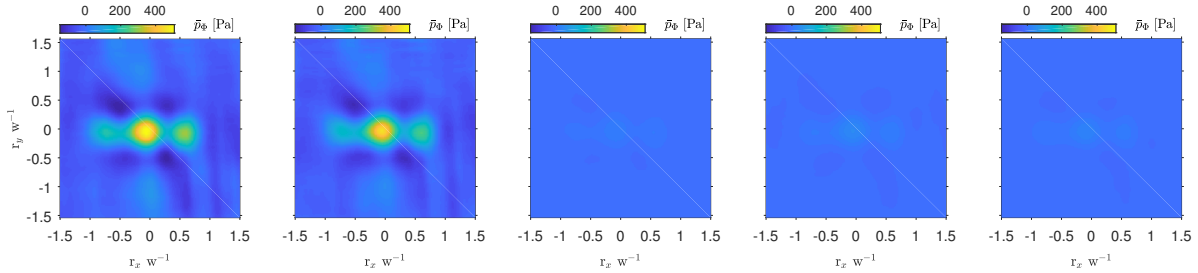

(a) $\Phi = 1\ \frac{2\pi}{20}$. (b) $\Phi = 2\ \frac{2\pi}{20}$. (c) $\Phi = 3\ \frac{2\pi}{20}$. (d) $\Phi = 4\ \frac{2\pi}{20}$. (e) $\Phi = 5\ \frac{2\pi}{20}$.

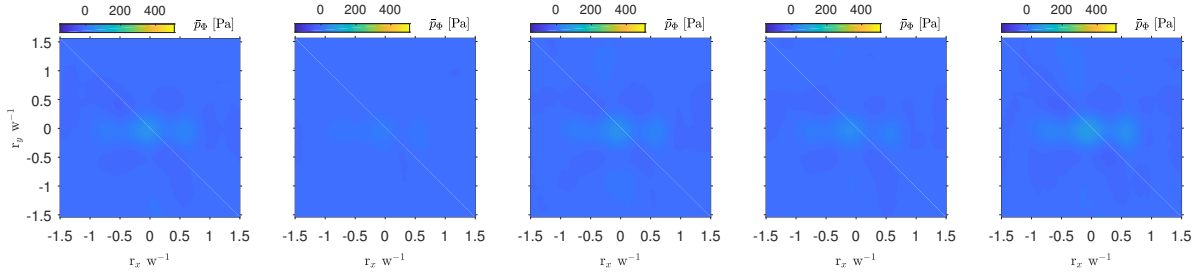

(f) $\Phi = 6\ \frac{2\pi}{20}$. (g) $\Phi = 7\ \frac{2\pi}{20}$. (h) $\Phi = 8\ \frac{2\pi}{20}$. (i) $\Phi = 9\ \frac{2\pi}{20}$. (j) $\Phi = 10\ \frac{2\pi}{20}$.

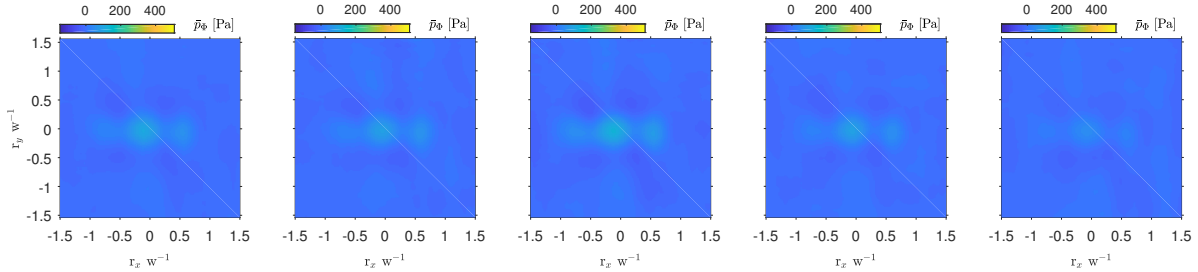

(k) $\Phi = 11\ \frac{2\pi}{20}$. (l) $\Phi = 12\ \frac{2\pi}{20}$. (m) $\Phi = 13\ \frac{2\pi}{20}$. (n) $\Phi = 14\ \frac{2\pi}{20}$. (o) $\Phi = 15\ \frac{2\pi}{20}$.

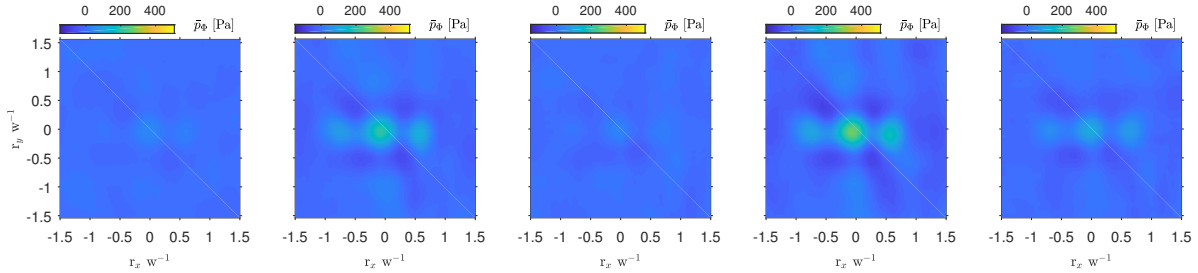

(p) $\Phi = 16\ \frac{2\pi}{20}$. (q) $\Phi = 17\ \frac{2\pi}{20}$. (r) $\Phi = 18\ \frac{2\pi}{20}$. (s) $\Phi = 19\ \frac{2\pi}{20}$. (t) $\Phi = 20\ \frac{2\pi}{20}$.

Figure 1: Pressure reconstructions from phase averaged slope maps (PRW = 12, $\sigma_\alpha = 8$). $h_N = 10$ mm, $U_{pp} = 46$ V.

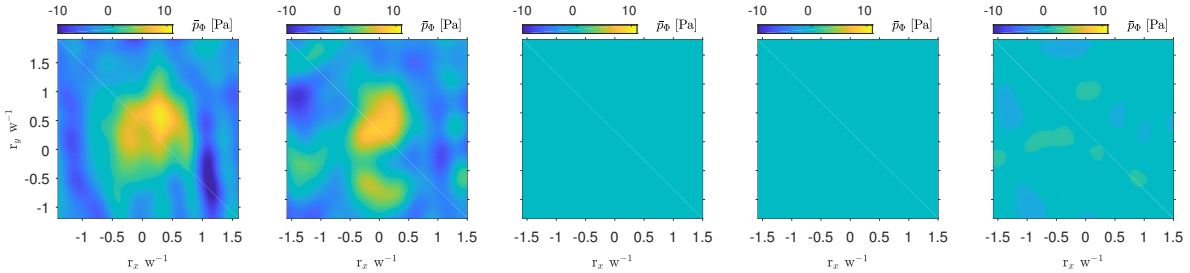

(a) $\Phi = 1\ \frac{2\pi}{20}$.

(b) $\Phi = 2\ \frac{2\pi}{20}$.

(c) $\Phi = 3\ \frac{2\pi}{20}$.

(d) $\Phi = 4\ \frac{2\pi}{20}$.

(e) $\Phi = 5\ \frac{2\pi}{20}$.

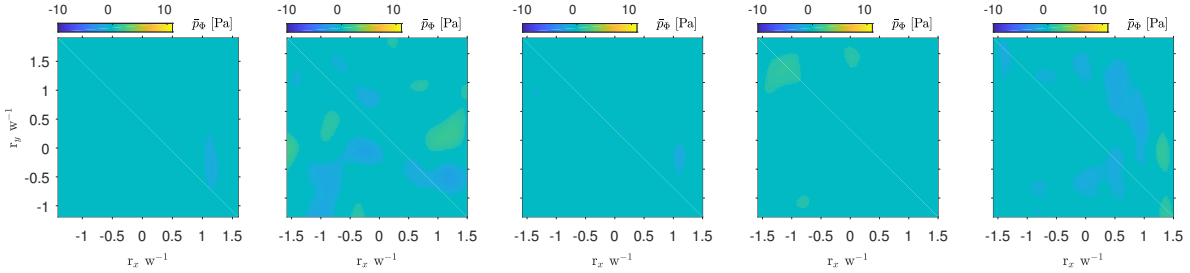

(f) $\Phi = 6\ \frac{2\pi}{20}$.

(g) $\Phi = 7\ \frac{2\pi}{20}$.

(h) $\Phi = 8\ \frac{2\pi}{20}$.

(i) $\Phi = 9\ \frac{2\pi}{20}$.

(j) $\Phi = 10\ \frac{2\pi}{20}$.

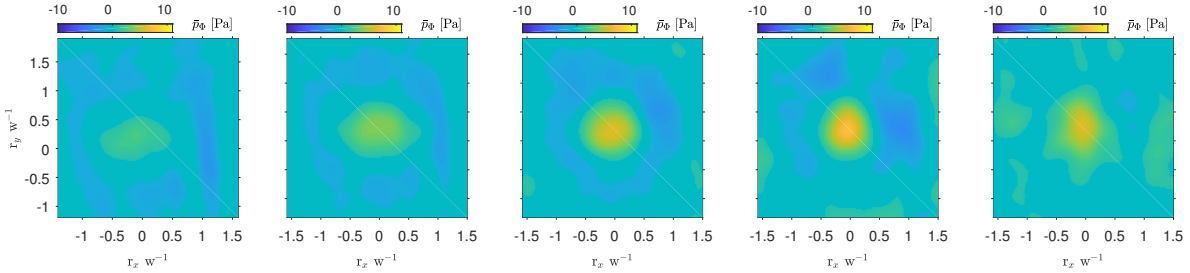

(k) $\Phi = 11\ \frac{2\pi}{20}$.

(l) $\Phi = 12\ \frac{2\pi}{20}$.

(m) $\Phi = 13\ \frac{2\pi}{20}$.

(n) $\Phi = 14\ \frac{2\pi}{20}$.

(o) $\Phi = 15\ \frac{2\pi}{20}$.

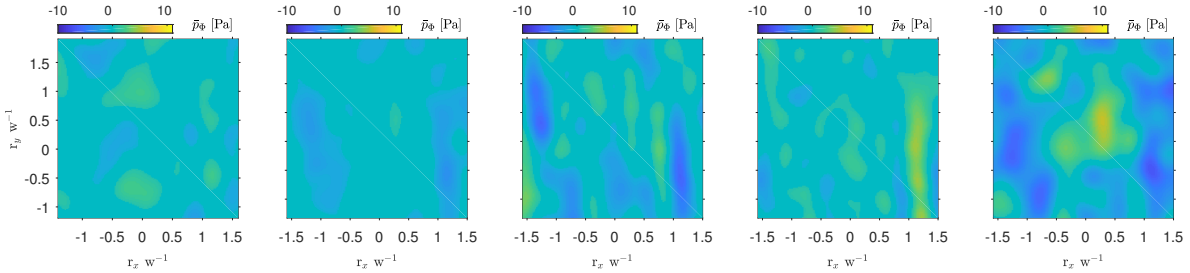

(p) $\Phi = 16\ \frac{2\pi}{20}$.

(q) $\Phi = 17\ \frac{2\pi}{20}$.

(r) $\Phi = 18\ \frac{2\pi}{20}$.

(s) $\Phi = 19\ \frac{2\pi}{20}$.

(t) $\Phi = 20\ \frac{2\pi}{20}$.

Figure 2: Pressure reconstructions from phase averaged slope maps (PRW = 42, $\sigma_\alpha = 7$). $h_N = 25$ mm, $U_{pp} = 20$ V.

Appendix B

Additional Background

1 DMD

The main aspects of DMD as introduced in Schmidt, 2010 are recalled here. For a snapshot sequence $\mathbf{V_1^N} = \mathbf{v_1}...\mathbf{v_N}$, where the $\mathbf{v_i}$ represent individual snapshots, the technique assumes that a linear mapping $\boldsymbol{A}$ exists which remains approximately constant over the entire data set, such that $\boldsymbol{A}\boldsymbol{V}_1^{N-1} = \boldsymbol{V}_2^N$. By calculating the Singular Value Decomposition (SVD) for the snapshot sequence,

$$\boldsymbol{V}_1^{N-1} = \boldsymbol{U}\boldsymbol{\Sigma}\boldsymbol{W}^H \quad , \tag{1}$$

where the superscript H denotes the conjugate transpose, one obtains:

$$\boldsymbol{U}^H\boldsymbol{A}\boldsymbol{U} = \boldsymbol{U}^H\boldsymbol{V}_2^N\boldsymbol{W}\boldsymbol{\Sigma}^{-1} = \tilde{\boldsymbol{S}} \quad . \tag{2}$$

Note that the right hand side of equation 1 contains the Proper Orthogonal Decomposition (POD), Pearson, 1901, of the snapshot sequence, with the spatial structures contained in $\boldsymbol{U}$, the temporal structures in $\boldsymbol{W}$ and the energy coefficients in $\boldsymbol{\Sigma}$. $\tilde{\boldsymbol{S}}$ is thus a projection of $\boldsymbol{A}$ onto the spatial POD modes. For large data sets, this step is computationally expensive and requires large amounts of RAM. Truncating the POD modes can mitigate this problem. Especially modes $\boldsymbol{\Phi}$ containing small amounts of energy often correspond to random noise events. The dynamic modes can then be obtained using the *eigenvectors* $\boldsymbol{y}_j$ for $\tilde{\boldsymbol{S}}\boldsymbol{y}_j = \mu_j\boldsymbol{y}_j$:

$$\boldsymbol{\Phi}_j = \boldsymbol{U}\boldsymbol{y}_j \quad . \tag{3}$$

Further, the complex *eigenvalues* contain information on damping and frequency coefficients of the modes:

$$\mu_j = e^{\delta_j + i\cdot f_j} \quad . \tag{4}$$

δ_j is the damping coefficient and f_j the frequency of the j-th mode. Finally, the amplitudes of each mode need to be determined. Introducing the matrix:

$$\boldsymbol{L} = \begin{bmatrix} \boldsymbol{Y} \\ \boldsymbol{Y}\boldsymbol{M} \\ ... \\ \boldsymbol{Y}\boldsymbol{M}^{N-1} \end{bmatrix} \quad , \tag{5}$$

with the matrix $\boldsymbol{Y}$ containing the *eigenvectors* of $\tilde{\boldsymbol{S}}$ as columns and the diagonal matrix $\boldsymbol{M}$ containing the corresponding *eigenvalues* as diagonal elements, one obtains:

$$\boldsymbol{V}_1^N = \boldsymbol{L}\boldsymbol{C} \quad . \tag{6}$$

Now $\boldsymbol{L}$ contains the information on shapes and temporal evolution of the modes, and the diagonal matrix $\boldsymbol{C}$ the amplitude coefficients c_j as diagonal elements. Using the SVD $\boldsymbol{L} = \boldsymbol{U}_L\boldsymbol{\Sigma}_L\boldsymbol{W}_L^H$ one can obtain the pseudo inverse of $\boldsymbol{L}$ such that:

$$\boldsymbol{C} = \boldsymbol{W}_L\boldsymbol{\Sigma}_L^{-1}\boldsymbol{U}_L^H\boldsymbol{V}_1^N \quad . \tag{7}$$

Now the snapshot reconstructions can be expressed as:

$$\boldsymbol{v}_k = \sum_{j=1}^{N_{modes}} \boldsymbol{\Phi}_j \exp\left(i f_j + \delta_j\right) \cdot f_{aq}^{-1} \cdot (k-1) c_j \quad . \tag{8}$$

In order to manage the large data sets encountered in this study, the streaming DMD approach introduced in Hemati et al., 2014 was employed here. It is based on incrementally updating an orthonormal basis calculated from all available snapshots with the Gram-Schmidt process. This basis is used to obtain a POD, which is also truncated to reduce computational cost. The snapshot projections onto this basis are used to calculate a DMD operator $\tilde{\boldsymbol{K}}$, which takes the place of $\tilde{\boldsymbol{S}}$ above.

References

Amitay, M. and Cannelle, F. (2006). Evolution of finite span synthetic jets. *Physics of Fluids*, 18(5):054101.

Ashby, M. (2011). *Materials selection in mechanical design*. Butterworth-Heinemann, Oxford, fourth edition edition.

Badulescu, C., Grédiac, M., and Mathias, J. D. (2009). Investigation of the grid method for accurate in-plane strain measurement. *Measurement Science and Technology*, 20(9):095102.

Balzer, J. and Werling, S. (2010). Principles of shape from specular reflection. *Measurement*, 43(10):1305 – 1317.

Barbero, E. (2013). *Finite element analysis of composite materials using ANSYS®, Second Edition*. Composite Materials. CRC Press.

Beltaos, S. (1976). Oblique impingement of circular turbulent jets. *Journal of Hydraulic Research*, 14(1):17–36.

Berry, A. and Robin, O. (2016). Identification of spatially correlated excitations on a bending plate using the virtual fields method. *Journal of Sound and Vibration*, 375:76 – 91.

Berry, A., Robin, O., and Pierron, F. (2014). Identification of dynamic loading on a bending plate using the virtual fields method. *Journal of Sound and Vibration*, 333(26):7151 – 7164.

Bioucas-Dias, J. and Valadão, G. (2007). Phase unwrapping via graph cuts. *IEEE Transactions on Image Processing*, 16(3):698–709.

Brown, K., Brown, J., Patil, M., and Devenport, W. (2018). Inverse measurement of wall pressure field in flexible-wall wind tunnels using global wall deformation data. *Experiments in Fluids*, 59(2):25.

Browne, L. and Dinkelacker, A. (1995). Turbulent pipe flow: pressures and velocities. *Fluid Dynamics Research*, 15(3):177 – 204.

Bull, M. (1996). Wall-pressure fluctuations beneath turbulent boundary layers: Some reflections on forty years of research. *Journal of Sound and Vibration*, 190(3):299 – 315.

Chen, N. and Yu, H. (2014). Mechanism of axis switching in low aspect-ratio rectangular jets. *Computers and Mathematics with Applications*, 67(2):437 – 444. Mesoscopic Methods for Engineering and Science (Proceedings of ICMMES-2012, Taipei, Taiwan, 23-27 July 2012).

Corcos, G. M. (1963). Resolution of pressure in turbulence. *The Journal of the Acoustical Society of America*, 35(2):192–199.

Corcos, G. M. (1964). The structure of the turbulent pressure field in boundary-layer flows. *Journal of Fluid Mechanics*, 18(3):353–378.

Dai, X., Xie, H., and Wang, Q. (2014). Geometric phase analysis based on the windowed Fourier transform for the deformation field measurement. *Optics and Laser Technology*, 58:119 – 127.

Davila, A., Ruiz, P., Kaufmann, G., and Huntley, J. (2003). Measurement of sub-surface delaminations in carbon fibre composites using high-speed phase-shifted speckle interferometry and temporal phase unwrapping. *Optics and Lasers in Engineering*, 40(5-6):447–458.

de Kat, R. and van Oudheusden, B. W. (2012). Instantaneous planar pressure determination from piv in turbulent flow. *Experiments in Fluids*, 52(5):1089–1106.

D'Errico, J. (2009). Inverse (integrated) gradient. https://de.mathworks.com/matlabcentral/fileexchange/ 9734-inverse-integrated-gradient (accessed on 12.06.2019).

Devivier, C. (2012). *Damage identification in layered composite plates using kinematic full-field measurements*. PhD thesis, Université de Technologie de Troyes.

Devivier, C., Pierron, F., Glynne-Jones, P., and Hill, M. (2016). Time-resolved full-field imaging of ultrasonic Lamb waves using deflectometry. *Experimental Mechanics*, pages 1–13.

Devivier, C., Pierron, F., and Wisnom, M. (2012). Damage detection in composite materials using deflectometry, a full-field slope measurement technique. *Composites Part A: Applied Science and Manufacturing*, 43(10):1650 – 1666.

Dinkelacker, A., Hessel, M., Meier, G. E. A., and Schewe, G. (1977). Investigation of pressure fluctuations beneath a turbulent boundary layer by means of an optical method. *Physics of Fluids*, 20:S216–S224.

Dym, C. and Shames, I. (1973). *Solid mechanics: a variational approach*. Advanced engineering series. McGraw-Hill.

Emmerling, R., Meier, G. E. A., and Dinkelacker, A. (1975). Wall pressure fields under turbulent boundary layers. Technical report, Max-Planck-Institut fuer Stroemungsforschung Goettingen.

Engler, R. H., Klein, C., and Trinks, O. (2000). Pressure sensitive paint systems for pressure distribution measurements in wind tunnels and turbomachines. *Measurement Science and Technology*, 11(7):1077–1085.

Gardon, R. and Akfirat, J. (1965). The role of turbulence in determining the heat-transfer characteristics of impinging jets. *International Journal of Heat and Mass Transfer*, 8(10):1261 – 1272.

Ghaemi, S., Ragni, D., and Scarano, F. (2012). Piv-based pressure fluctuations in the turbulent boundary layer. *Experiments in Fluids*, 53.

Giraudeau, A., Pierron, F., and Guo, B. (2010). An alternative to modal analysis for material stiffness and damping identification from vibrating plates. *Journal of Sound and Vibration*, 329(10):1653–1672.

Glezer, A. and Amitay, M. (2002). Synthetic jets. *Annual Review of Fluid Mechanics*, 34(1):503–529.

Grédiac, M., Sur, F., and Blaysat, B. (2016). The grid method for in-plane displacement and strain measurement: A review and analysis. *Strain*, 52(3):205–243.

Gregory, J. W., Asai, K., Kameda, M., Liu, T., and Sullivan, J. P. (2008). A review of pressure-sensitive paint for high-speed and unsteady aerodynamics. *Proceedings of the Institution of Mechanical Engineers, Part G: Journal of Aerospace Engineering*, 222(2):249–290.

Hemati, M., Williams, M., and Rowley, C. (2014). Dynamic mode decomposition for large and streaming datasets. *Physics of Fluids*, 26(11):111701.

Hibino, K., Larkin, K., Oreb, B., and Farrant, D. (1995). Phase shifting for nonsinusoidal waveforms with phase-shift errors. *Journal of the Optical Society of America A*, 12(4):761–768.

Holman, R., Utturkar, Y., Mittal, R., Smith, B., and Cattafesta, L. (2005). Formation criterion for synthetic jets. *AIAA JOURNAL*, 43:2110–2116.

Jambunathan, K., Lai, E., Moss, M., and Button, B. (1992). A review of heat transfer data for single circular jet impingement. *International Journal of Heat and Fluid Flow*, 13(2):106 – 115.

Jaw, Y., Chen, J.-H., and Wu, P.-C. (2009). Measurement of pressure distribution from PIV experiments. *Journal of Visualization*, 12:27–35.

Kalifa, R. B., Habli, S., Saïd, N. M., Bournot, H., and Palec, G. L. (2016). The effect of coflows on a turbulent jet impacting on a plate. *Applied Mathematical Modelling*, 40(11):5942 – 5963.

Kaufmann, R., Pierron, F., and Ganapathisubramani, B. (submitted 2019a). Full-field surface pressure reconstruction using the Virtual Fields Method. *Experimental Mechanics*.

Kaufmann, R., Pierron, F., and Ganapathisubramani, B. (submitted 2019b). Reconstruction of surface pressure fluctuations using deflectometry and the Virtual Fields Method. *Experiments in Fluids*.

Kim, J.-H., Pierron, F., Wisnom, M., and Avril, S. (2009). Local stiffness reduction in impacted composite plates from full-field measurements. *Composites Part A: Applied Science and Manufacturing*, 40(12):1961 – 1974.

Kim, M., Li, Y., Peng, D., Yeom, E., and Kim, K. C. (2019). Flow and surface pressure field measurements on a circular cylinder with impingement of turbulent round jet. *Experimental Thermal and Fluid Science*, 105:67 – 76.

Leclére, Q. and Pézerat, C. (2012). Vibration source identification using corrected finite difference schemes. *Journal of Sound and Vibration*, 331(6):1366 – 1377.

Lecoq, D., Pézerat, C., Thomas, J.-H., and Bi, W. (2014). Extraction of the acoustic component of a turbulent flow exciting a plate by inverting the vibration problem. *Journal of Sound and Vibration*, 333(12):2505 – 2519.

Liu, Q., Sleiti, A., and Kapat, J. (2008). Application of pressure and temperature sensitive paints for study of heat transfer to a circular impinging air jet. *International Journal of Thermal Sciences*, 47(6):749 – 757.

Martins, J., Andrade-Campos, A., and Thuillier, S. (2018). Comparison of inverse identification strategies for constitutive mechanical models using full-field measurements. *International Journal of Mechanical Sciences*, 145:330 – 345.

Moulart, R., Pierron, F., Hallett, S. R., and Wisnom, M. R. (2011). Full-field strain measurement and identification of composites moduli at high strain rate with the virtual fields method. *Experimental Mechanics*, 51(4):509–536.

N. B. Livingood, J. and Hrycak, P. (1973). Impingement heat transfer from turbulent air jets to flat plates: A literature survey. Technical Report NASA-TM-X-2778, E-7298, NASA Lewis Research Center; Cleveland, OH, United States.

O'Donoughue, P., Robin, O., and Berry, A. (2017). Time-resolved identification of mechanical loadings on plates using the virtual fields method and deflectometry measurements. *Strain*, 54(3):e12258.

O'Donoughue, P., Robin, O., and Berry, A. (2019). Inference of random excitations from contactless vibration measurements on a panel or membrane using the virtual fields method. In Ciappi, E., De Rosa, S., Franco, F., Guyader, J.-L., Hambric, S. A., Leung, R. C. K., and Hanford, A. D., editors, *Flinovia—Flow Induced Noise and Vibration Issues and Aspects-II*, pages 357–372, Cham. Springer International Publishing.

Pearson, K. (1901). Liii. on lines and planes of closest fit to systems of points in space. *The London, Edinburgh, and Dublin Philosophical Magazine and Journal of Science*, 2(11):559–572.

Pezerat, C. and Guyader, J.-L. (2000). Force Analysis Technique: Reconstruction of force distribution on plates. *Acta Acustica united with Acustica*, 86(2):322–332.

Pierron, F. and Grédiac, M. (2012). *The virtual fields method. Extracting constitutive mechanical parameters from full-field deformation measurements.* Springer New-York.

Pierron, F., Sutton, M. A., and Tiwari, V. (2011). Ultra High Speed DIC and Virtual Fields Method Analysis of a Three Point Bending Impact Test on an Aluminium Bar. *Experimental Mechanics*, 51(4):537–563.

Poon, C. Y., Kujawinska, M., and Ruiz, C. (1993). Spatial-carrier phase shifting method of fringe analysis for moiré interferometry. *The Journal of Strain Analysis for Engineering Design*, 28(2):79–88.

Ragni, D., Ashok, A., van Oudheusden, B. W., and Scarano, F. (2009). Surface pressure and aerodynamic loads determination of a transonic airfoil based on particle image velocimetry. *Measurement Science and Technology*, 20(7):074005.

Ritter, R. (1982). Reflection moire methods for plate bending studies. *Optical Engineering*, 21:21 – 9.

Robin, O. and Berry, A. (2018). Estimating the sound transmission loss of a single partition using vibration measurements. *Applied Acoustics*, 141:301 – 306.

Rossi, M. and Pierron, F. (2012). On the use of simulated experiments in designing tests for material characterization from full-field measurements. *International Journal of Solids and Structures*, 49(3):420 – 435.

Schmidt, P. J. (2010). Dynamic mode decomposition of numerical and experimental data. *Journal of Fluid Mechanics*, 656:5–28.

Surrel, Y. (1996). Design of algorithms for phase measurements by the use of phase stepping. *Applied Optics*, 35(1):51–60.

Surrel, Y. (2000). *Photomechanics*, chapter Fringe Analysis, pages 55–102. Springer Berlin Heidelberg, Berlin, Heidelberg.

Surrel, Y., Fournier, N., Grédiac, M., and Paris, P.-A. (1999). Phase-stepped deflectometry applied to shape measurement of bent plates. *Experimental Mechanics*, 39(1):66–70.

Surrel, Y. and Pierron, F. (2019). Deflectometry on curved surfaces. In Lamberti, L., Lin, M.-T., Furlong, C., Sciammarella, C., Reu, P. L., and Sutton, M. A., editors, *Advancement of Optical Methods & Digital Image Correlation in Experimental Mechanics, Volume 3*, pages 217–221, Cham. Springer International Publishing.

Timoshenko, S. and Goodier, J. (1951). *Theory of Elasticity*. McGraw-Hill.

Timoshenko, S. and Woinowsky-Krieger, S. (1959). *Theory of plates and shells*. Engineering societies monographs. McGraw-Hill.

Toniuc, H. and Pierron, F. (submitted 2018). Infrared deflectometry for surface slope deformation measurements. *Experimental Mechanics*.

Toussaint, E., Grédiac, M., and Pierron, F. (2006). The virtual fields method with piecewise virtual fields. *International Journal of Mechanical Sciences*, 48(3):256 – 264.

Tropea, C., Yarin, A., and Foss, J. (2007). *Springer handbook of experimental fluid mechanics*. Springer-Verlag Berlin Heidelberg.

Usherwood, J. R. (2009). The aerodynamic forces and pressure distribution of a revolving pigeon wing. *Experiments in Fluids*, 46(5):991–1003.

Van Buren, T., Whalen, E., and Amitay, M. (2014). Vortex formation of a finite-span synthetic jet: effect of rectangular orifice geometry. *Journal of Fluid Mechanics*, 745:180 – 207.

van Oudheusden, B. W. (2013). PIV-based pressure measurement. *Measurement Science and Technology*, 24(3):032001.

Willmarth, W. W. (1975). Pressure fluctuations beneath turbulent boundary layers. *Annual Review of Fluid Mechanics*, 7(1):13–36.

Xu, Y. and Wang, J. J. (2016a). Flow structure evolution for laminar vortex rings impinging onto a fixed solid wall. *Experimental Thermal and Fluid Science*, 75:211 – 219.

Xu, Y. and Wang, J. J. (2016b). Flow structure evolution for laminar vortex rings impinging onto a fixed solid wall. *Experimental Thermal and Fluid Science*, 75:211 – 219.

Yang, L., Zare-Behtash, H., Erdem, E., and Kontis, K. (2012). Application of AA-PSP to hypersonic flows: The double ramp model. *Sensors and Actuators B: Chemical*, 161(1):100 – 107.

Young, F. L. (1965). Experimental investigation of the effects of surface roughness on compressible turbulent boundary layer skin friction and heat transfer. Technical Report AD0621085, Texas University at Austin Defense Research Laboratories.

Zienkiewicz, O. (1977). *The finite element method*. McGraw-Hill.

Zuckerman, N. and Lior, N. (2006). Jet impingement heat transfer: Physics, correlations, and numerical modeling. *Advances in Heat Transfer*, 39(C):565 – 631.